Optimization of Energy Management in Heavy-Duty Fuel Cell Hybrid Electric Vehicle Conversion: Enhancing Lifetime and Efficiency with Fuzzy Logic-Based Strategies

by

Elnaz TAYEBAN

THESIS PRESENTED TO ÉCOLE DE TECHNOLOGIE SUPÉRIEURE
IN PARTIAL FULFILLMENT OF A MASTER'S DEGREE
WITH THESIS IN ELECTRICAL ENGINEERING
M.A.Sc.

MONTREAL, SEPTEMBER 23, 2024

ÉCOLE DE TECHNOLOGIE SUPÉRIEURE
UNIVERSITÉ DU QUÉBEC

BOARD OF EXAMINERS

THIS THESIS HAS BEEN EVALUATED

BY THE FOLLOWING BOARD OF EXAMINERS

M. Ricardo Izquierdo, Thesis supervisor
Department of Electrical Engineering, École de technologie supérieure

M. Qingsong Wang, Chair, Board of Examiners
Department of Electrical Engineering, École de technologie supérieure

Mrs. Gaixia Zhang, Member of the Jury
Department of Electrical Engineering, École de technologie supérieure

THIS THESIS WAS PRESENTED AND DEFENDED

IN THE PRESENCE OF A BOARD OF EXAMINERS AND THE PUBLIC

ON SEPTEMBER 13, 2024

AT ÉCOLE DE TECHNOLOGIE SUPÉRIEURE

ACKNOWLEDGEMENTS

First and foremost, I extend my deepest gratitude to Professor Ricardo Izquierdo, my supervisor, for his invaluable expertise, guidance, and patience. His dedication and commitment have been instrumental in overcoming the numerous challenges encountered during my research. His willingness to share his profound knowledge and insights has significantly contributed to the completion of my thesis. I am truly appreciative of the opportunity to work under his supervision at the École de Technologie Supérieure, Montréal, Canada.

I offer my sincere thanks to the LaCIME laboratory, particularly to Professor Izquierdo and Normand Gravel, the laboratory manager, for providing me the honor of accessing their esteemed facilities and research tools. Equally, my deepest appreciation goes to Mathieu Gratuze, whose fellowship and counsel were essential in extending my research interests at ÉTS. He played a critical role in advancing my academic and linguistic challenges, and his efforts are genuinely indelible.

My acknowledgment would be incomplete without mentioning Mitacs Canada and ALTABEC Inc. for their Acceleration program, which not only provided me with an invaluable internship opportunity but also offered financial support. This experience has been fundamental in gaining hands-on experience and has immensely contributed to my personal and professional growth.

I am thankful to my colleagues, lab mates, and friends for their irreplaceable help and companionship during my time at ÉTS, making it both fruitful and enjoyable.

My deepest gratitude goes to my family, especially my parents, for their countless sacrifices and constant encouragement, and to my brother Omid for being an exceptional role model and source of motivation throughout my life. I am also profoundly grateful to Pouria, my partner, for his unwavering faith and undying love, which have been my strength foundation. Similarly, my heartfelt thanks to Asoo, whose loyal friendship and support have remained strong despite the distance, delivering deep reassurance and powerful inspiration.

This achievement mirrors our shared support and belief, crucial to my growth academically and personally. Your inspiration and faith fueled my journey—this success is ours together.

Optimisation de la Gestion de l'Énergie dans la Conversion de Véhicules Hybrides Électriques à Pile à Combustible de Fort Tonnage : Amélioration de la Durée de Vie et de l'Efficacité avec des Stratégies Basées sur la Logique Fuzzy

Elnaz TAYEBAN

RÉSUMÉ

Le transport est un contributeur majeur aux émissions mondiales de CO_2, responsable d'environ 20% du total, avec une consommation d'énergie dans ce secteur comptant pour près d'un quart de toutes les émissions. L'Agence Internationale de l'Énergie (AIE) souligne que le transport routier est le plus grand émetteur au sein du secteur, représentant 75% des émissions de transport en 2018, divisé entre les véhicules de passagers (45,1%) et les camions de fret (29,4%). Cela signifie que le voyage sur route seul est responsable d'environ 15% des émissions mondiales de CO_2. Les effets néfastes des gaz à effet de serre incluent le changement climatique, qui conduit à des conditions météorologiques extrêmes, des perturbations dans l'approvisionnement alimentaire et une augmentation des incendies de forêt, ainsi que des problèmes de santé tels que les maladies respiratoires dues à la pollution de l'air. Étant donné ces défis environnementaux et sanitaires significatifs posés par les véhicules conventionnels, le passage vers des options de transport durables est critique. Les véhicules électriques à pile à combustible (FCEV) se démarquent comme une solution viable, offrant une alternative propre en émettant uniquement de la vapeur d'eau. Souligné par le Massachusetts Institute of Technology, les FCEV ont le potentiel de réduire considérablement les émissions de gaz à effet de serre et de réduire la dépendance au pétrole sans changer les habitudes de conduite actuelles. Ils offrent également des avantages par rapport aux véhicules électriques à batterie (BEV), y compris des gammes plus longues et des temps de ravitaillement plus rapides, les rendant une option attrayante pour un large éventail d'utilisations, des camions lourds aux voyages de longue distance (*Nunez* (2019)*InternationalRenewableEnergy Laboratory* (2011)Camacho (2022)).

Cette thèse vise à transformer un camion lourd conventionnel de classe 8 C10 Caterpillar Kenworth 2002 avec un moteur à combustion interne en un véhicule électrifié en remplaçant le moteur à essence par un moteur électrique (EM), éliminant ainsi les émissions. La conversion utilise un mélange d'hydrogène et de batteries pour alimenter un processus électrochimique dans une pile à combustible, générant de l'électricité pour alimenter l'EM sans émissions nocives, ne produisant que de l'eau et de la chaleur comme sous-produits. La conception du système est bifurquée en sous-système de traction (TS) et sous-système de stockage d'énergie (ESS), chacun étant validé séparément. L'architecture de contrôle comprend des contrôleurs locaux (Contrôleur PI) pour le TS et l'ESS, se concentrant respectivement sur la vitesse du véhicule et le courant de la pile à combustible, ainsi qu'une stratégie globale de gestion de l'énergie (EMS). Conçu et simulé dans MATLAB-Simulink avec une représentation macroscopique énergétique (EMR), cette approche illustre les interactions complexes du système et les complexités de contrôle. L'EMS pour l'ESS est exploré à travers trois scénarios : fonctionnement continu de la pile à combustible, une stratégie basée sur des règles simples, et une méthode basée sur la Fuzzy Logic, évaluant leur performance par rapport aux objectifs et contraintes du système.

La dernière partie de cette thèse se concentre sur la réalisation d'objectifs systémiques spécifiques : réduire le poids global du véhicule, minimiser la consommation d'hydrogène et prolonger la durée de vie du pack de batteries. Le système ESS est conçu de manière à ce que le pack de batteries fournisse le courant maximal demandé par le moteur électrique (EM) à tout moment, indépendamment de la capacité de la batterie. Cette conception, optimisée par l'opération de la pile à combustible pendant le cycle de conduite européen (NEDC), permet une réduction significative du nombre de modules de batterie, réduisant le poids de moitié, soit environ 414 kg.

L'efficacité de la conception de l'ESS a été évaluée à travers trois scénarios. Dans le premier scénario, avec la pile à combustible (FC) fonctionnant en continu, l'état de charge (SOC) de la batterie a dépassé 0,7, ne répondant pas à l'objectif de maximiser la durée de vie de la batterie, qui nécessite de maintenir un SOC entre 0,4 et 0,7. Ce scénario a également conduit à une consommation inutile d'hydrogène. Le deuxième scénario a mis en œuvre une stratégie simple basée sur des règles pour le contrôle du courant de la FC, activant la FC à un SOC de 0,4 et la désactivant à 0,7. Cependant, pendant le NEDC, le SOC est tombé à 0,27 par moments, indiquant un risque pour la longévité de la batterie, malgré une consommation d'hydrogène réduite.

Le troisième scénario, employant une stratégie de Fuzzy Logic pour l'EMS, a réussi à maintenir le SOC dans la plage optimale de 0,4 à 0,7, s'alignant ainsi sur tous les objectifs du système, y compris une consommation d'hydrogène réduite. Ce scénario a démontré la supériorité de l'approche de la Fuzzy Logic dans l'optimisation de la performance du système et la réalisation des avantages environnementaux et opérationnels prévus.

Mots-clés: véhicules électriques à pile à combustible (FCEV), camion lourd, stratégie de gestion de l'énergie (EMS), Fuzzy Logic, Contrôleur PI, la pile à combustible (FC), représentation macroscopique énergétique (EMR)

Optimization of Energy Management in Heavy-Duty Fuel Cell Hybrid Electric Vehicle Conversion: Enhancing Lifetime and Efficiency with Fuzzy Logic-Based Strategies

Elnaz TAYEBAN

ABSTRACT

Transportation is a major contributor to global CO_2 emissions, responsible for about 20% of the total, with energy consumption in this sector accounting for nearly a quarter of all emissions. The International Energy Agency (IEA) highlights that road transport is the largest emitter within the sector, accounting for 75% of transportation emissions in 2018, divided between passenger vehicles (45.1%) and freight trucks (29.4%). This signifies that road travel alone is responsible for roughly 15% of global CO_2 emissions. The adverse effects of greenhouse gases include climate change, which leads to extreme weather, disruptions in food supply, and increased wildfires, alongside health issues such as respiratory illnesses due to air pollution. Given these significant environmental and health challenges posed by conventional vehicles, the shift towards sustainable transport options is critical. Fuel Cell Electric Vehicles (FCEVs) stand out as a viable solution, offering a clean alternative by emitting only water vapor. Highlighted by the Massachusetts Institute of Technology, FCEVs have the potential to drastically cut greenhouse gas emissions and reduce petroleum dependence without changing current driving habits. They also offer advantages over Battery Electric Vehicles (BEVs), including longer ranges and faster refueling times, making them an appealing option for a broad spectrum of uses, from heavy-duty trucks to long-distance travel (*Nunez* (2019)*InternationalRenewableEnergy Laboratory* (2011)Camacho (2022)).

This thesis aims to transform a conventional Class 8 C10 Caterpillar Kenworth 2002 truck with an internal combustion engine into an electrified vehicle by replacing the gasoline engine with an Electric Motor (EM), thereby eliminating emissions. The conversion utilizes a mix of hydrogen and batteries to fuel an electrochemical process in a fuel cell, generating electricity to power the EM without harmful emissions, only producing water and heat as by-products. The system design is bifurcated into the Traction Subsystem (TS) and the Energy Storage Subsystem (ESS), with each being validated separately. The control architecture comprises local controllers for the TS and ESS, focusing on vehicle speed and fuel cell current, respectively, and a global Energy Management Strategy (EMS). Designed and simulated in MATLAB-Simulink with an Energetic Macroscopic Representation (EMR), this approach illustrates the intricate system interactions and control complexities. The EMS for the ESS is explored through three scenarios: continuous fuel cell operation, a rule-based strategy, and a fuzzy logic-based method, assessing their performance against the system's objectives and constraints.

The final part of this thesis focuses on achieving specific system objectives: reducing the vehicle's overall weight, minimizing hydrogen consumption, and extending the battery pack's lifetime. The Energy Storage System (ESS) is designed so that the battery pack delivers the maximum current demanded by the Electric Motor (EM) at any moment, independent of battery capacity. This design, optimized through fuel cell operation during the New European Driving

Cycle (NEDC), allows for a significant reduction in the number of battery modules, halving the weight by approximately 414kg.

The effectiveness of the ESS design was evaluated across three scenarios. In the first scenario, with the fuel cell (FC) continuously operating, the battery's State of Charge (SOC) exceeded 0.7, failing to meet the objective of maximizing battery life, which requires maintaining an SOC between 0.4 and 0.7. This scenario also led to unnecessary hydrogen consumption. The second scenario implemented a simple rule-based strategy for FC current control, turning the FC on at an SOC of 0.4 and off at 0.7. However, during the NEDC, the SOC dropped to 0.27 at times, indicating a risk to battery longevity, despite reduced hydrogen use.

The third scenario, employing a fuzzy-logic strategy for the EMS, successfully maintained the SOC within the optimal range of 0.4 to 0.7, thereby aligning with all system objectives, including reduced hydrogen consumption. This scenario demonstrated the superiority of the fuzzy-logic approach in optimizing system performance and achieving the intended environmental and operational benefits.

Keywords: Fuel Cell Electric Vehicle (FCEV), Heavy-Duty, Energy Management Strategy (EMS), Fuzzy Logic, PI Controller, Fuel Cell (FC),Energetic Macroscopic Representation (EMR)

TABLE OF CONTENTS

Page

LIST OF TABLES

LIST OF FIGURES

LIST OF ABBREVIATIONS

AFC	Alkaline Fuel Cell
BEV	Battery Electric Vehicle
CCS	Carbon Capture and Storage
CHP	Combined Heat and Power
CO_2	Carbon Dioxide
EM	Electric Motor
EMR	Energetic Macroscopic Representation
EMS	Energy Management Strategy
ESS	Energy Storage Subsystem
FC	Fuel Cell
FCEV	Fuel Cell Hybrid Electric Vehicle
FIS	Fuzzy Inference System
FLC	The Fuzzy Logic Controller
GHG	Green-House Gas
GVM	Gross Vehicle Mass
HEV	Hybrid Electric Vehicle
IBC	Inversion Based Control
LTI	Linear Time-Invariant
LSM	Lanthanum Strontium Manganite

MCFC	Molten Carbonate Fuel Cell
MHEV	Mild Hybrid Electric Vehicle
NEDC	New European Driving Cycle
PAFC	Phosphoric Acid Fuel Cell
PEHV	Plug-in Hybrid Electric Vehicle
PEM	Polymer Electrolyte Membrane
PEMFC	Proton Exchange Membrane Fuel Cell
PI	Proportional-Integral
Pt	Platinum
REEV	Range-Extender Electric Vehicle
Ru	Ruthenium
SOC	State of Charge
SOFC	Solid Oxide Fuel Cell
SOH	State of Health
TS	Traction Subsystem
TTW	Tank-To-Wheel
YSZ	Yttrium Stabilized Zirconia

INTRODUCTION

The introduction provides an entry into the concept of Fuel Cell Hybrid Electric Vehicles (FCEVs) and the complexity of their Energy Management Strategy (EMS). This discourse explains the combination of eco-friendly propulsion and sophisticated control methodologies. Emphasis is placed on the conversion of heavy-duty trucks, clarifying the challenges encountered and the methodologies adopted. A preview of forthcoming chapters is also offered, providing a general view of the thematic landscape.

0.1 The Evolution of Hybrid Electric Vehicles: Hydrogen's Role in Electrification

Hybrid Electric Vehicles (HEVs) are a noteworthy advancement in the automotive industry, providing a promising solution to address the adverse environmental effects of Green-House Gas (GHG) emissions.Granovskii, Dincer & Rosen (2006) This study delves into the history and potential of HEVs, with a specific emphasis on FCEVs. FCEVs find application in both city cars and heavy-duty trucks, and their effectiveness in reducing and, in certain cases, eliminating GHG emissions has garnered significant attention in recent years Ajanovic & Haas (2019).

The history of HEVs dates back to the late 19th century when the convergence of electric and gasoline-powered technologies began. Throughout the years, various types of HEVs have been developed, including Battery Electric Vehicles (BEV), Fuel Cell Electric Vehicles (FCEV), Plug-in Hybrid Electric Vehicles (PHEV), Range-Extended Electric Vehicles (REEV) and Mild Hybrid Electric Vehicles (MHEV) Ajanovic (2015). Among these, FCEVs have gained attention for their remarkable advantages. FCEVs operate by utilizing hydrogen fuel along with a fuel cell stack to generate electricity for propulsion. In FCEVs, hydrogen is stored in high-pressure tanks within the vehicle. The fuel cell stack, which consists of individual fuel cells, plays a crucial role in the process U.S. Department of Energy (2023). Hydrogen from the storage tanks is supplied to the anode side of the fuel cell stack. At the anode, hydrogen molecules are split into protons ($H+$) and electrons ($e-$) through an electrochemical reaction. The proton exchange membrane within the fuel cell stack allows only protons to pass through, while electrons take an external path, creating an electrical current. This current flows through an external circuit, generating usable electrical power that drives the Electric Motor (EM) of the FCEV. At the cathode side of the fuel cell stack, oxygen from the atmosphere combines with protons and electrons to produce water vapour (H_2O) as the only byproduct. This water vapour is released from the FCEV, resulting in a clean and environmentally friendly operation Blal *et al.* (2019). FCEVs exhibit numerous advantages that make them a compelling technology. Firstly, FCEVs boast zero emissions, emitting only water vapour, thereby contributing to enhanced air quality and addressing climate change concerns. Secondly, FCEVs demonstrate high energy efficiency by directly converting hydrogen fuel into electricity through the fuel cell, eliminating the need for intermediate energy conversions. This efficiency translates into greater mileage and reduced energy consumption. Thirdly, refuelling an FCEV is swift, comparable to conventional vehicles, taking only a few minutes to fill up the hydrogen tank. This convenience eliminates range anxiety commonly associated with battery electric vehicles. Furthermore, FCEVs typically offer an extended driving range, surpassing that of battery-electric vehicles, allowing for longer trips without frequent recharging. Lastly, FCEVs exhibit versatility, finding applications in various sectors, including passenger vehicles as well as heavy-duty applications like trucks and buses. This versatility presents a wide range of possibilities for reducing emissions in different transportation domains Manoharan *et al.* (2019).

FCEVs are utilized in both city cars and large commercial trucks, providing unique benefits in each area. In urban areas, FCEVs can address challenges such as air and noise pollution. For instance, the Toyota Mirai, an FCEV, has been introduced as a city car with zero emissions and a longer driving range compared to BEVs. On the other hand, FCEVs also present opportunities for reducing GHG emissions in the heavy-duty truck sector. The Nikola Tre, an FCEV truck, showcases the potential for long-haul freight transport with lower emissions compared to conventional diesel trucks Cullen *et al.* (2021),Nikola Corporation (2023).

Statistical data from credible sources supports the environmental benefits of FCEVs. Statistics show that FCEVs can achieve an efficiency of up to 60%, surpassing the 25-30% efficiency range of conventional vehicles Plug Power Inc.. Furthermore, the European Commission notes that FCEVs emit only water vapour and warm air as byproducts, contributing to improved air quality European Commission Green propulsion in transport. Figure 0.1 from the International Energy Agency reveals that over 20 countries have established electrification targets or internal combustion engine bans for cars, and 8 countries, along with the European Union, have announced net-zero emission pledges. These initiatives are expected to significantly reduce GHG emissions in the transportation industry.

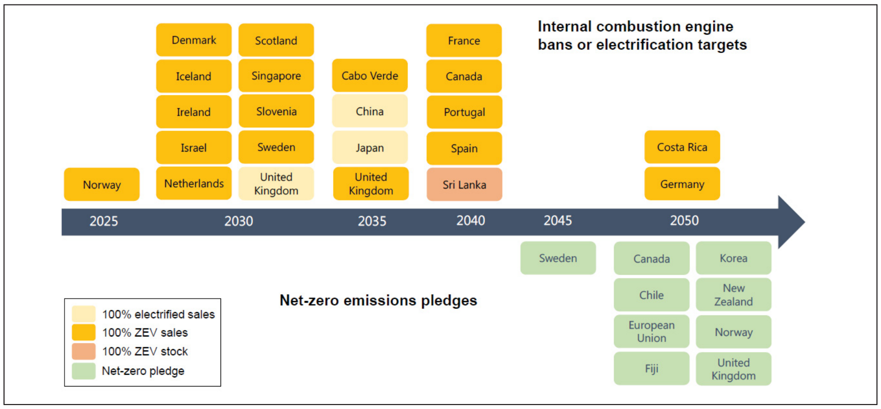

Figure 0.1 More than 20 countries have electrification targets or ICE bans for cars, and 8 countries plus the European Union have announced net-zero pledges

Taken from The Global EV Outlook (2021)

The heavy dependence on fossil fuels, accounting for 80% of the world's energy consumption, poses two significant challenges. Firstly, fossil fuel reserves are depleting, projected by 2023. Secondly, fossil fuels contribute to environmental concerns, incurring an annual cost of around $5 trillion. The *Hydrogen Energy System* was introduced in 1970 as a solution, utilizing hydrogen's distinct properties as a clean and efficient energy source. The electrochemical conversion of hydrogen in fuel cells surpasses the performance of traditional fuels. This has driven the adoption of hydrogen fuel cells, especially for road and rail transport, as a fossil-fuel-free alternative. FCEVs integrate Fuel Cells (FC) with batteries and/or Ultracapacitors to enhance power density and meet load requirements. To achieve this, an EMS is employed, utilizing various control techniques for optimal performance Sorlei *et al.* (2021). This study provides an overview of FCEV technology and EMS, discussing propulsion systems and strategies.

0.2 Transitioning Conventional Heavy-Duty Trucks to FCEVs: Identifying the Challenge

The central challenge addressed by this thesis is the conversion of a conventional heavy-duty truck powered by an internal combustion engine into an FCEV. This research focuses on the optimization of energy management in these converted heavy-duty FCEVs, aiming to enhance their lifetime and efficiency. Employing fuzzy logic-based strategies, the thesis explores advanced methods for EMS optimization to achieve superior performance and sustainability in heavy-duty fuel cell hybrid electric vehicle conversions. This process involves complex technological, operational, and logistical considerations, including the integration of fuel cell systems, energy management strategies, and the reconfiguration of conventional vehicle components. As the transportation sector seeks sustainable alternatives, this transition aims to mitigate the environmental effects of heavy-duty vehicles while advancing the practicality of FCEVs in real-world scenarios.

Transportation represents a significant portion of global carbon dioxide (CO_2) emissions, accounting for about one-fifth of total emissions. This includes emissions from energy consumption, which makes up around 24% of total emissions. The breakdown of these emissions by mode of transport is of interest – cars, trucks, planes, and trains.

Figure 0.2 presents the distribution of global transport emissions in 2018, sourcing its data from the International Energy Agency (IEA). Within this, road travel accounts for the largest share, contributing 75% of total transport emissions. Passenger vehicles, including cars and buses, make up 45.1% of this share, while the remaining 29.4% is attributed to freight-carrying trucks. Considering the transportation sector's overall contribution of 21% to total emissions, and given that road transport constitutes three-quarters of these transportation emissions, road travel alone is responsible for approximately 15% of the total CO_2 emissions Hannah Ritchie (2020).

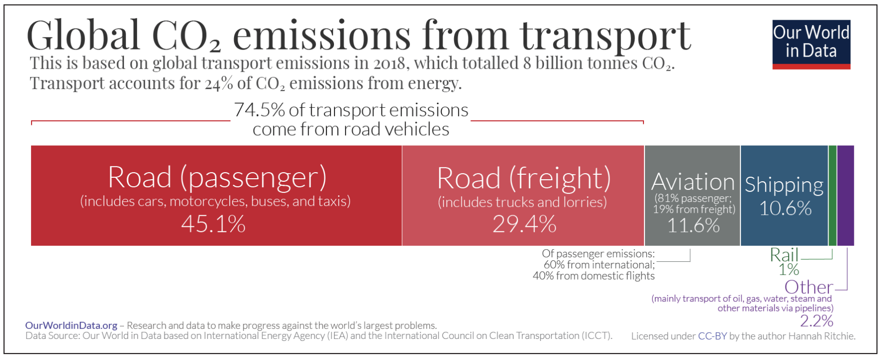

Figure 0.2 Global CO_2 emissions in 2018 totaled 8 billion tonnes. The transportation sector accounted for 24% of these emissions from energy, with nearly 75% of transportation emissions originating from road vehicles

Taken from Hannah Ritchie (2020)

Furthermore, greenhouse gases have significant impacts on the environment and public health. They contribute to climate change by trapping heat and cause respiratory issues through smog and air pollution. The climate change driven by these gases leads to extreme weather events, disruptions in food supply, and increased wildfire occurrences. Predicted weather patterns will change, altering ecosystems. Some species may go extinct, while others will migrate or expand their habitats Nunez (2019). Figure 0.3 shows these emissions result in extreme weather events, disruptions in food supplies, and increased wildfires, impacting both the environment and human health.

Figure 0.3 Climate risks and their impacts on sustainable Earth

Taken from WMO (2019)

Hence, the necessity for transitioning to more sustainable alternatives in the transportation sector is clear, given the substantial environmental and health challenges associated with conventional fossil fuel-powered vehicles. As discussed, the road transportation sector contributes a significant share, as high as 29.4% of global CO_2 emissions Hannah Ritchie (2020).

Within this context, FCEVs emerge as a suitable alternative. FCEVs provide a clean and efficient mode of transportation, emitting zero harmful pollutants at the tailpipe and producing only water vapor as a byproduct. They are particularly attractive because they address the issues of GHG emissions, air pollution, and dependence on finite fossil fuel resources. Research conducted at the Massachusetts Institute of Technology indicates that FCEVs have the inherent capacity to significantly reduce greenhouse gas emissions and the reliance on petroleum, all without requiring changes in driving behavior International Renewable Energy Laboratory (2011). Additionally, FCEVs offer a longer driving range and quicker refueling times compared to BEVs, making them suitable for a wider range of applications, including heavy-duty trucks and long-distance travel Camacho (2022).

This explains the purpose of this thesis: to explore and optimize the transition from conventional fossil fuel-powered vehicles to FCEVs, particularly in the heavy-duty truck sector. By focusing on FCEVs, this research aims to address the pressing environmental and health challenges posed by current transportation practices. The thesis seeks to demonstrate how FCEVs can significantly reduce GHG emissions, while also providing practical benefits such as longer driving ranges and quicker refueling times. Ultimately, the goal is to contribute to the development of sustainable transportation solutions that mitigate the environmental impact of heavy-duty vehicles and promote the broader adoption of FCEVs.

0.3 Methodology for Converting Heavy-Duty Trucks into FCEVs: A Transition Framework

The objective of this thesis is to study the conversion of a conventional internal combustion engine Class 8 heavy-duty truck into an electrified variant. Within our conversion process, we undertake the transformation of a Class 8 C10 Caterpillar Kenworth 2002 truck by substituting its internal combustion engine with an EM. This crucial conversion transforms environmentally harmful gasoline-powered vehicles into zero-emission alternatives. Traditionally, gasoline engine vehicles depend on fossil fuels to power the engine, which significantly contributes to adverse environmental impacts. According to the proposed method, we substitute this conventional fuel source with a combination of hydrogen and batteries, resulting in an electrochemical process within a fuel cell that generates electricity. This electricity effectively powers the EM and propels the vehicle. Crucially, this process is characterized by zero emissions, with the sole by-products being benign water and heat.

While this approach presents a promising solution, it is crucial to consider the limitations of battery-only systems for long-haul applications. The shift to battery-electric propulsion for these applications encounters significant obstacles due to various technical and practical constraints. These challenges include limited vehicle range, extended charging times that affect delivery schedules and vehicle uptime, high economic and environmental costs associated with battery production, and increased vehicle size, which reduces payload capacity due to the additional battery weight. Collectively, these issues impede the economic viability of BEVs in the commercial market.

In contrast, FCEVs offer a compelling solution, especially for long-distance transportation. FCEVs excel with rapid refueling times, reduced infrastructure requirements, and lighter powertrain weight, which enhances payload capacity and provides economic benefits. These practical advantages, combined with their capability to achieve zero tailpipe emissions, position FCEVs as a promising pathway for decarbonizing and electrifying the heavy-duty transport sector. This is true even when accounting for potentially lower overall tank-to-wheel (TTW) conversion efficiencies compared to BEVs Pardhi, Chakraborty & Tran (2022).

Furthermore, the hybrid powertrain in FCEVs addresses the limitations of fuel cells, particularly their low power variation rates. This hybrid setup can potentially extend the lifespan of fuel cells and improve operational efficiency compared to pure fuel cell vehicles. Essentially, the integration of fuel cells and batteries compensates for each other's drawbacks, offering a well-rounded and practical solution for long-haul heavy-duty transportation Liu, Liu & Qin (2020).

In our ongoing development, we have adopted an innovative powertrain design that incorporates two critical subsystems: the Traction Subsystem (TS) and the Energy Storage Subsystem (ESS). Aligning with the primary objectives of this thesis—to enhance battery lifetime, reduce vehicle weight, and minimize hydrogen consumption—we have developed a comprehensive strategy.

This approach focuses on prolonging the lifespan of energy sources, particularly the battery pack, and reducing overall weight and hydrogen consumption through a rule-based Energy Management Strategy (EMS) utilizing Fuzzy Logic. This novel approach signifies a major advancement in our conversion process, ultimately improving the eco-friendliness of heavy-duty trucks by optimizing the use of hydrogen resources and highly efficient energy storage systems.

To fulfill these objectives, several technical steps have been undertaken. First, a carefully selected prototype was used to define the specifications for the ESS section, EM, and auxiliary components. With the powertrain developed, we began designing the model and its control strategy. The challenge of efficiently distributing energy between the fuel cell and batteries in an FCEV required a robust EMS design to improve operational efficiency and prolong battery life. Furthermore, an Energetic Microscopic Representation (EMR) was employed as a visualization tool, providing a detailed understanding of the system design and its functionality.

The unique EMS, utilizing a rule-based methodology grounded in fuzzy logic, ensures that converting a long-haul heavy-duty vehicle is a compelling alternative for reducing greenhouse gas emissions while simultaneously optimizing system efficiency.

0.4 Thesis Outline and Organization

The introduction has presented the problem statement, thesis objective, and proposed solution. The problem revolves around the need to convert internal combustion engine heavy-duty trucks into FCEVs for more sustainable transportation. The objective is to enhance the lifespan of energy sources, particularly the battery pack, while minimizing hydrogen consumption and reducing vehicle weight through a rule-based EMS based on Fuzzy Logic. To accomplish this, a comprehensive approach has been employed, involving the selection of a well-studied prototype, dimensioning of relevant components, powertrain development, and EMS design. The structure of the thesis is as follows:

Chapter 1, This chapter provides a comprehensive review of the theory behind FCEVs. It begins with an introductory overview and a comparative analysis of different types HEVs and their applications. The chapter then delves into a detailed description of various FCEV components, and the essential EMS. Following this, it introduces our control system, detailing its different methods and the basics of its implementation. Finally, the chapter presents the Energetic Macroscopic Representation (EMR) as a visualization tool, used to explain the system as a whole. Importantly, this chapter explains why FCEVs are superior options for heavy-duty applications.

Chapter 2, presents the methodology used in designing the system. It begins by introducing the innovative EMR as a visualization tool, which helps to illustrate the system's complexity and provides a comprehensive understanding of its operation. The chapter then details the system methodology at two distinct levels: the Traction Subsystem (TS) and the Energy Storage Subsystem (ESS). It thoroughly examines the interaction between these two subsystems, highlighting their integrated functioning within the overall system.

In Chapter 3, the focus shifts to the Energy Management System (EMS). This chapter explores various EMS approaches and their applications in meeting the thesis objectives. It examines the complexities of different EMS techniques and their effectiveness in optimizing energy utilization. Additionally, this chapter illustrates how EMS is specifically employed to achieve the thesis goals, emphasizing its crucial role in efficiently managing power flows and enhancing the overall system performance.

Finally, Chapter 4 focuses on data acquisition and simulation. This chapter is dedicated to system validation and the detailed analysis of simulation results. It involves an in-depth evaluation of the system's performance under various scenarios, comparing its operation across multiple conditions. The simulation results provide crucial evidence of the system's robustness and effectiveness, offering valuable insights into its reliability and efficiency. These findings support the thesis objectives and demonstrate the overall efficacy of the system.

CHAPTER 1

BACKGROUND AND LITERATURE REVIEW

In the forthcoming section, we will systematically explore FCEVs, beginning with an introductory overview and a comparative analysis of different types of HEVs and the justification for FCEVs . Following this, we will discuss the components of FCEVs, with special emphasis on the battery, fuel cell, and essential EMS. We will then introduce our control system, outlining its various methods and the basics of its implementation. Finally, we will present the visualization tool EMR, used to explain the system as a whole. This section aims to provide readers with a comprehensive understanding of the fundamental architecture and operational dynamics of FCEVs.

1.1 FCEVs: Origins and Evolution

FCEVs have their roots in the early development of the hydrogen fuel cell. Sir William Robert Grove, a Welsh scientist, is credited with inventing the fuel cell in 1839. However, the concept largely remained unexplored until the 20th century Grove (1839). The space age, driven by NASA's requirements for a sustainable power source for space missions, rejuvenated interest in fuel cells in the 1960s nas (1965). The energy crisis in the 1970s further increased the need for alternative energy vehicles, including those powered by hydrogen. This backdrop led to the first prototype FCEVs being introduced in the 1990s by major automobile manufacturers. The 21st century has seen an accelerated interest in FCEVs due to growing environmental concerns, the urgency of reducing greenhouse gas emissions, and advancements in fuel cell technologies Fuel Cell & Hydrogen Energy Association (2021), James & Kalinoski (2002).

1.1.1 Introduction to FCEVs

FCEVs are an advanced class of vehicles that utilize hydrogen gas as a primary fuel. These vehicles contain an onboard FC that effectively transforms hydrogen into electricity. This generated electricity subsequently powers an electric motor to drive the vehicle. The sole emission from this conversion process is water vapor, positioning FCEVs as a viable solution in the domain of zero-emission transport Kromer & Heywood (2007).

The importance of FCEVs in the modern transportation landscape cannot be overstated. With rising global concerns about environmental degradation and the need to reduce greenhouse gas emissions, FCEVs present a compelling and eco-friendly alternative. They offer extended driving ranges comparable to gasoline vehicles and relatively quick refueling times, giving them a significant advantage over conventional battery electric vehicles. As technological advancements and infrastructure developments continue to enhance the feasibility of hydrogen as a clean fuel, FCEVs are set to play a crucial role in the future of sustainable transportation Saur & Ramsden (2014).

1.1.2 Constituent Elements

In the following discussion, we will focus on the primary components of FCEVs, particularly the battery, fuel cell, and EMS System. FCEVs utilize a combination of fuel cells and batteries. The EMS plays a crucial role by intelligently managing and directing the flow of energy between these two sources during vehicle operation. This dynamic allocation ensures that the energy requirements of the electric propulsion system are met effectively and efficiently Noura (2022a).

Subsequent sections will systematically explore the core components that constitute FCEVs. Initially, attention will be given to the battery, exploring its integral function and operational characteristics. This will be followed by an in-depth examination of the FC, discussing its mechanism and significance in the system. Concluding this sequential exploration, the EMS will be presented, emphasizing its pivotal role in harmonizing the synergy between the battery and fuel cell. A comprehensive understanding of these elements is indispensable to appreciate the complexity of our system design. It should be noted that in this section, we only provide an introductory overview of these components, with detailed information and thorough discussions reserved for subsequent chapters.

1.1.2.1 Battery Functionality Introduction

Batteries serve as compact energy storage systems, utilizing multiple electrochemical cells to transform stored chemical energy into electricity. This conversion is both efficient and emission-free during use. These batteries rely on specific materials, designed for consistent chemical reactions across multiple charging cycles Whittingham (2012). Each battery possesses two main electrodes: an anode and a cathode as shown in Figure 1.1.

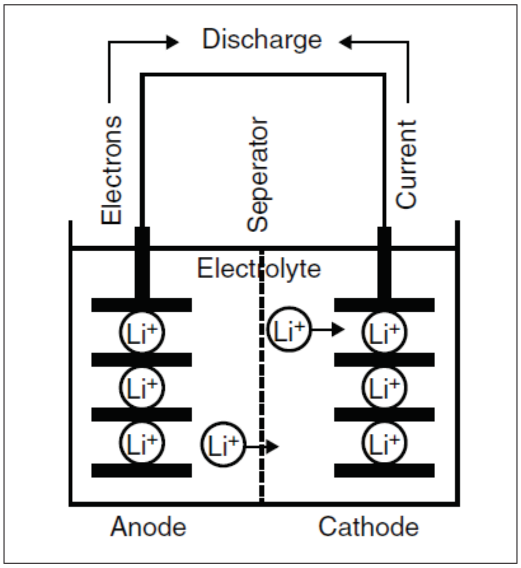

Figure 1.1 Schematics of a common battery

Taken from Dincer, Hamut & Javani (2016)

Over the years, numerous battery chemistries have emerged. Among these, Li-ion batteries stand out, dominating many applications. They come in four distinct designs: small cylindrical, large cylindrical, prismatic, and pouch. Cylindrical variants, produced in vast quantities, are renowned for their shape retention and resilience against external forces. However, their thermal management capabilities diminish with size, and replacing them can be a challenge. Prismatic cells, encased in a semi-rigid plastic casing, boast efficient volume usage and are equipped with threaded holes for bolts, facilitating replacement. The pouch design offers high energy and power densities due to minimal packaging but needs additional safeguards to ensure longevity

Pesaran, Kim & Keyser (2009). Despite these specifics, batteries have become the preferred choice for HEVs and EVs, primarily due to their efficiency.

Key battery parameters include its capacity, expressed in Ah, indicating the maximum discharge current; energy content, derived by multiplying capacity with average discharge voltage, represented in KWh; and power, calculated as the product of voltage and current, displayed in KW. The state of charge (SOC) is another essential metric, signifying the available charge percentage in the battery Tie & Tan (2013).

Presently, batteries are the primary choice for EVs and HEVs because of their efficiency in delivering both peak and average power. However, when compared to traditional fuels, they have limitations like reduced specific energy, energy density, and slower refueling/charging rates. These factors contribute to limitations in vehicle range, bulkier sizes, higher costs, and subsequently, a limited adoption rate.

A typical electric vehicle powered by batteries covers approximately 3-6 miles per KWh, contingent on factors like the vehicle's design and driving patterns. For instance, current technologies necessitate roughly 150 kg of Li-ion cells (or over 500 kg of lead-acid cells) to achieve a 200 km range under average driving conditions. Doubling this range would proportionally increase the required power, weight, and corresponding costs. Modern battery requirements, especially for electric vehicles, prioritize high discharge and recharge rates, large capacity, and robust cycling capabilities.

1.1.2.2 Fuel Cell Functionality Introduction

Interest in fuel cells as a sustainable power source has surged due to the adverse effects of relying on fossil fuels, such as pollution, resource depletion, and geopolitical tensions. Fuel cells, particularly Polymer Electrolyte Membrane (PEM) types, offer a versatile and cleaner energy alternative that aligns with both efficiency and environmental criteria. These cells can operate on various fuels, including hydrogen, ethanol, and biomass-derived materials, either directly or through a reforming process. Given the pressing need for energy transition, a phased approach guided by government and industry initiatives can leverage existing fossil fuels for hydrogen production before fully transitioning to cleaner sources Spiegel (2011).

A fuel cell functions like a facility that converts fuel into electricity continuously, as long as fuel is available. This distinguishes it from a battery, which gets depleted. Essentially, the fuel cell serves as a medium for the transformation of chemical energy in the fuel into electrical power. This is similar to combustion engines, which also convert chemical energy into usable mechanical or electrical forms. At the molecular level, the oxidation of hydrogen molecules in the presence of oxygen results in water and heat production, as illustrated in Figure 1.2.

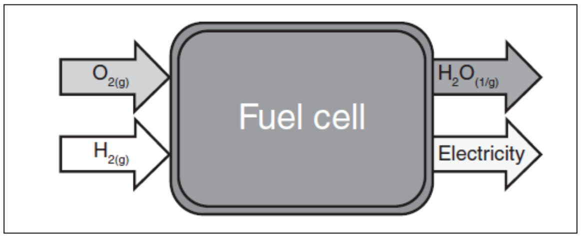

Figure 1.2 Fuel Cell and its general concept

Taken from O'hayre, Cha, Colella & Prinz (2016)

In a fuel cell, hydrogen undergoes a split into two separate electrochemical reactions, one taking place at the anode and the other at the cathode. To grasp the fundamentals of electrochemistry, it is crucial to understand four key terms: oxidation, reduction, anode, and cathode. Oxidation involves the removal of electrons from a molecule, while reduction involves the addition of electrons. In the context of a hydrogen-oxygen fuel cell, hydrogen is oxidized at the anode, releasing electrons. Oxygen undergoes reduction at the cathode, consuming electrons. The anode is generally the electrode where electrons are released, and the cathode is where electrons are received. This sets the stage for understanding the hydrogen oxidation reaction and the oxygen reduction reaction as integral components in fuel cell operation O'hayre *et al.* (2016). Figure 1.3 illustrates the fundamental operation of a fuel cell as an electrochemical energy conversion device. It depicts how hydrogen and oxygen are utilized to produce electricity, heat, and water. Specifically, the figure highlights the roles of the anode and the cathode in facilitating the key electrochemical processes of oxidation and reduction Dincer *et al.* (2016).

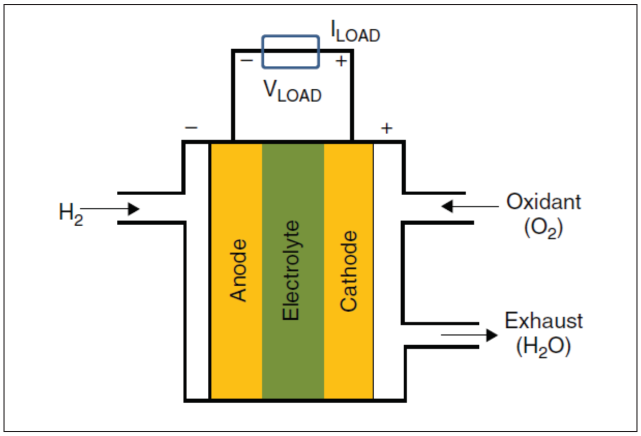

Figure 1.3 This illustration outlines the four fundamental stages in the operation of a fuel cell: 1) Initial entry of hydrogen atoms into the anode; 2) Electron removal from these atoms at the anode; 3) Proton migration through the membrane to the cathode, while electrons traverse the external circuit, contributing to electrical output; 4) Subsequent recombination of electrons, protons, and ambient oxygen to yield the end products of heat and water

Taken from Dincer *et al.* (2016)

1.1.2.3 Energy Management Strategy Introduction

HEVs offer significant advantages in fuel efficiency and emissions reduction compared to traditional vehicles, thanks to their integrated energy storage and electric drive systems. These systems enable features such as engine-off idling, regenerative braking, power augmentation, and the use of a smaller engine. The bidirectional operation of these electric components allows energy to be stored during engine operation or braking and then used when needed. This multifaceted energy sourcing adds complexity to managing power distribution between the engine and the energy storage system. The primary goal of the energy management strategy is to optimize fuel usage and, if possible, reduce emissions, all while maintaining vehicle performance Serrao, Onori & Rizzoni (2011). This research aims to decrease hydrogen fuel usage in an FCEV and extend battery longevity while maintaining a low overall battery pack weight. Given that the vehicle's power sources consist only of an FC and a battery, it inherently operates with zero emissions. Therefore, the objective of minimizing emissions is inherently satisfied in this configuration. In the energy management framework of a HEV, the speed controller, usually represented by the driver or a basic feedback mechanism in simulations, determines the total power requirement to maintain a given speed. The energy management strategy then allocates this power demand between the onboard energy sources, usually a battery and a fuel tank, specifying the engine and battery power outputs Serrao *et al.* (2011). For this research, the focus of EMS is on efficiently dividing the power demand between the battery and the FC and this is executed by monitoring the vehicle dynamics. The vehicle is modeled as a dynamic system with two independent states: speed of the vehicle and the SOC of the energy storage. Faster dynamics like speed changes in powertrain components are omitted as they do not substantially impact fuel consumption. This simplified, steady-state model provides an adequate representation of overall efficiency and is computationally efficient for simulating an entire driving cycle as illustrated in Figure 1.4.

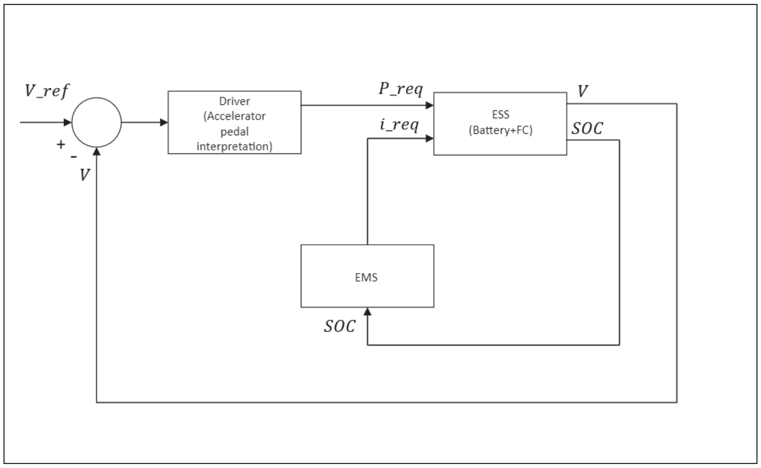

Figure 1.4 The function of EMS within a HEV

In this research, the challenge of EMS is framed as an optimal control problem. The main objective is to carefully distribute power between the fuel cell and battery to maximize the battery's lifespan and reduce the amount of hydrogen used. The EMS serves as the uppermost layer in the powertrain control hierarchy and plays a pivotal role in determining the most efficient power distribution between the available energy sources. Various approaches to solving this intricate optimization problem have been explored in existing literature. In the field of EMS, two main types of methodologies stand out: rule-based and optimization-based approaches, as outlined in Figure 1.5. These categories serve as the foundational paradigms for developing various EMS techniques, highlighting the range of available solutions Ouddah & Adouane (2019).

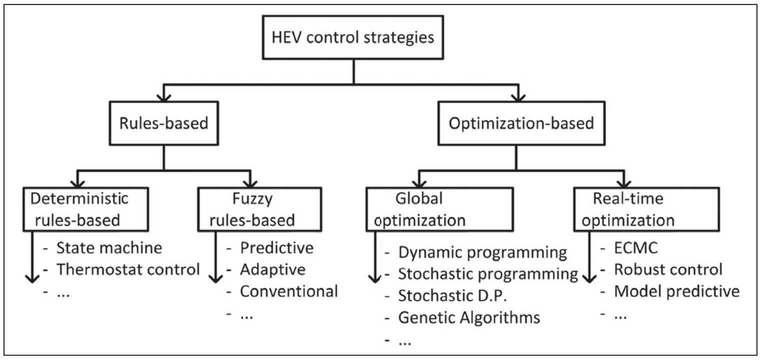

Figure 1.5 Categorization of control approaches for hybrid vehicles

Taken from Ouddah & Adouane (2019)

In the automotive sector, rules-based EMSs have historically been favored for their ease of implementation and real-time effectiveness. These can be subdivided into deterministic and fuzzy rules-based systems. These strategies rely on an intuitive control framework that transforms engineering insights into practical outcomes, although they necessitate meticulous parameter tuning. It's noteworthy that the academic sphere is increasingly concentrating on the utilization of fuzzy logic Ouddah & Adouane (2019). On the subject of fuzzy logic, its applications in energy management have been proposed and discussed extensively in the literature. The Fuzzy Logic Controller (FLC) is adept at simulating human cognitive processes and expertise, especially when dealing with ambiguous or imprecise information. Although FLC has successfully addressed numerous complex issues that are not easily described by complete mathematical models, the subjectivity in designing its rule base and membership functions poses limitations to their adjustability Kamal & Adouane (2018).

In this research, a rule-based methodology featuring an FLC will be utilized for the design of the EMS. The primary objectives to be addressed are the optimization of battery longevity and the minimization of hydrogen fuel consumption. Through the capabilities of FLC, which have been demonstrated to effectively manage imprecise data and complex scenarios, an EMS will be developed that adeptly balances these objectives. A data-driven decision-making process, rooted in engineering principles, will be employed to achieve sustainable and efficient vehicle operation.

1.1.3 FCEVs Powertrain

In an FCEV, the *powertrain* designates the assembly of elements responsible for creating and transferring energy to propel the vehicle. Within a front-wheel-drive FCEV framework, the powertrain encompasses elements such as the Fuel Cell Stack, Battery Pack, DC/DC converter, traction motor along with its control unit, and the vehicle's wheels and body Yao *et al.* (2019). These components, along with the EMS, constitute the focus of this research.

As depicted in Figure 1.6, the architecture of the powertrain in the FCEV under investigation closely resembles that of traditional HEVs, wherein the energy sources interface with the wheels via an EM. This FCEV powertrain is principally made up of an FC, an energy-storage battery, a DC/DC converter, a DC/AC inverter, and a motor. The simulation model, constructed in SIMULINK, incorporates the FC's polarization curve, an energy management system, a lithium-ion battery module, an EM, and a vehicle dynamics model. In this research, the Proton Exchange Membrane Fuel Cell (PEMFC) serves as the primary energy source, delivering consistent driving power and linking electrically to the DC power bus via a unidirectional DC/DC converter. As the key energy storage component, the lithium-ion battery pack is directly connected to the DC bus to stabilize the voltage. It also provides additional, instantaneous energy during vehicle acceleration and captures regenerative energy during braking Liu *et al.* (2020).

In an FCEV, the powertrain is divided into two primary subsystems: the Energy Storage Subsystem (ESS) and the Traction Subsystem (TS). The ensuing section delves into the critical role and intricacies of the ESS and TS in the overall functionality of the FCEV.

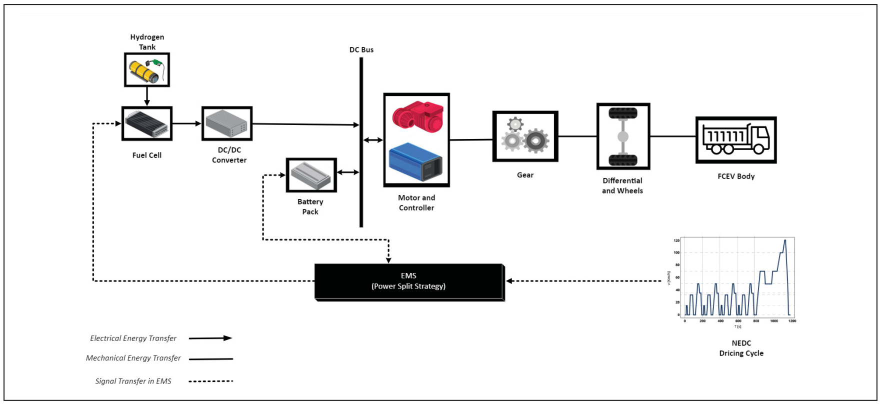

Figure 1.6 The diagram outlining the powertrain components of a FCEV

1.1.3.1 Energy Storage Subsystem & Traction Subsystem

ESSs serve as integral energy reservoirs that complement the fuel cell system in an FCEV. These systems, which can include batteries and FCs, are pivotal in fulfilling the vehicle's varying power requirements. Not only do they charge and discharge through multiple cycles, but they also influence the overall performance of the FCEV. The characteristics of these storage systems, such as energy capacity and power density, can differ significantly between BEVs, HEVs, and FCEVs. For FCEVs, an effective ESS should possess both high energy and high power density to tackle issues like cold starts and transient power spikes. The ESS technology currently faces challenges, such as high initial and replacement costs, large size, and reliability concerns. Future research directions include exploring alternative storage mechanisms like flywheels and assessing the longevity of ESS in real-world applications Waseem, Amir, Lakshmi, Harivardhagini & Ahmad (2023) Sorlei *et al.* (2021). In the realm of FCEVs that are tailored for medium to heavy-duty long-distance applications, the term TS is employed to designate the section of the vehicle's powertrain that is primarily responsible for generating mechanical motion. The TS predominantly draws its energy from the FC and is engineered to meet or slightly exceed the median power requirements for the vehicle, thereby ensuring optimal fuel cell efficiency. To accommodate high power demand scenarios, such as rapid acceleration or hill climbing, the accompanying component in ESS, in this research battery pack, is configured with elevated current and energy capacities Pardhi *et al.* (2022).

As illustrated in Figure 1.7, the ESS and TS components of the powertrain are distinctly highlighted.

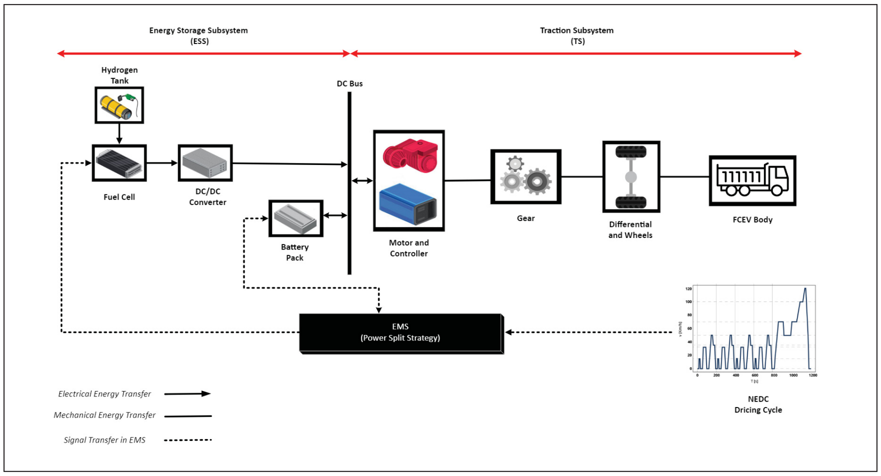

Figure 1.7 Powertrain schematic of an FCEV highlighting the Energy Storage System (ESS) and the Traction Subsystem (TS)

1.2 Fundamentals and Characterization of Fuel Cell Technology

This section introduces the fundamentals of fuel cells and their types, focusing on PEMFCs. It also explains the importance of the polarization curve in fuel cell modeling. The content lays the groundwork for later discussions on FCEVs.

1.2.1 Introduction to Fuel Cell Technology

Fuel cells are electrochemical devices that facilitate the direct conversion of chemical energy into electrical energy. Unlike traditional combustion engines, which rely on thermal processes, fuel cells achieve energy conversion without combustion, thus emitting fewer pollutants and greenhouse gases. This makes them a pivotal technology in the transition toward sustainable and green energy solutions Wang *et al.* (2020).

1.2.2 Types of Fuel Cells

Fuel cells are categorized based on factors like the electrolyte employed, operational conditions, load needs, fuel availability, start-up time, and their specific applications. Various fuel cell electrolytes exist, available in both solid and liquid forms. They can operate at high or low temperatures. Specifically, low-temperature fuel cells necessitate catalysts to accelerate their chemical processes Abdelkareem *et al.* (2021). The prominent types include:

1. Proton Exchange Membrane Fuel Cells (PEMFCs): A PEMFC consists of an electrolyte facilitating proton movement, specifically $H+$, from its anode to its cathode. This membrane is a solid polymer and functions within a temperature range of 70 to $90°C$ at pressures of 1–2 bar. A singular cell within this fuel cell type typically has a voltage of $1.1v$, and this value amplifies based on the total number of cells in the stack. The fundamental electrochemical processes in a hydrogen fuel cell, exemplified by the PEMFC, are outlined in Equation 1.1 Ijaodola *et al.* (2018).

$$\begin{aligned}\text{Anode: } & \mathrm{H_2(g)} \rightarrow \mathrm{2H^+(aq)} + \mathrm{2e^-} \\ \text{Cathode: } & \frac{1}{2}\mathrm{O_2(g)} + \mathrm{2H^+(aq)} + \mathrm{2e^-} \rightarrow \mathrm{H_2O(l)} \\ \text{Overall: } & \mathrm{H_2(g)} + \frac{1}{2}\mathrm{O_2(g)} \rightarrow \mathrm{H_2O(l)} + \text{electric energy} + \text{waste heat}\end{aligned} \tag{1.1}$$

Bipolar plates, typically made from graphite, are integral components of FCs. These plates contain channels facilitating the entry of required reactants. Their design is pivotal not only for FC performance but also for managing heat and moisture within the cell. To regulate the heat produced, certain FCs are equipped with cooling mechanisms. Enhancing FC efficiency is imperative, given the associated fuel costs. Optimization relies on enhancing its multiple components. The design strategy should prioritize cost-effectiveness, manufacturability, and competitiveness within the energy storage market. A significant cost component of the FC is the electrocatalyst layer. Platinum (Pt) is commonly employed in this layer to expedite specific chemical reactions, supported by a minimal presence of a material named Nafion. Within this FC setup, electrons traverse from one end to the other, while protons journey through a specialized medium. The culmination of these movements results in a chemical transformation. The attributes of such FCs encompass rapid activation, robust construction, adaptability in power output, and scalability. However, these FCs present challenges: they exhibit delayed oxygen interactions, difficulties in thermal and moisture regulation, and necessitate ultra-pure hydrogen. Yet, their potential to serve as alternatives in automotive and aerospace propulsion systems remains undeniable Abdelkareem *et al.* (2021).

The subsequent Figure 1.8 provides an in-depth representation of this specific fuel cell.

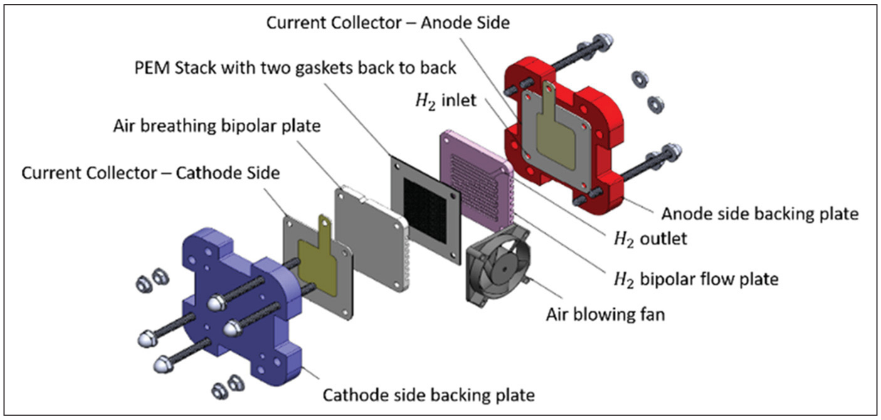

Figure 1.8 An illustrative breakdown of the components in a proton exchange membrane fuel cell (PEMFC)

Taken from Wilberforce *et al.* (2019)

2. Alkaline Fuel Cells (AFCs): The AFC utilizes solutions like $NaOH$ or KOH as its electrolyte and functions within a temperature range of 23–70°C. Different from PEMFCs, the AFC is an anion exchange membrane fuel cell and stands as one of the earliest fuel cell technologies. Its merits include high efficiency, efficient heat regulation, prompt start-up, and cost-effectiveness. Although AFCs can potentially replace platinum with nickel-based alloys at the anode, they face challenges with CO_2 sensitivity, leading to electrolyte consumption and diminished performance Abdelkareem *et al.* (2021).

3. Direct alcohol fuel cell (DAFC): Operating primarily under 100°C, DAFCs are favored for portable power needs up to $250W$. These cells mainly utilize alcohols like methanol and

ethanol, evident in DMFC and DEFC types. The catalyst layer in DAFCs often combines Pt and Ruthenium (Ru), with the latter shielding Pt from CO poisoning. Key advantages of DAFCs include rapid start-up, the capability to source fuels from waste (e.g., derived methanol or ethanol), impressive energy density, straightforward fuel handling, and cost-efficiency. Yet, they face the issue of fuel crossover, which results from concentration gradients causing fuel to move from the anode to the cathode, impacting performance negatively Abdelkareem *et al.* (2021).

4. Phosphoric acid fuel cells (PAFC): The PAFC operates within a temperature range of 150 to 220°C, ideally around 180°C. Utilizing phosphoric acid (H_3PO_4) as its electrolyte, the PAFC stands out for its widespread commercial application and notable maturity level among fuel cells Eapen, Suseendiran & Rengaswamy (2016). PAFCs present key benefits like greater CO poisoning resistance and cost-efficiency due to lesser Pt catalyst needs than PEMFCs. Their operation at higher temperatures also makes them apt for Combined Heat and Power (CHP) systems by leveraging waste heat Ito (2017). However, they also come with challenges such as higher initial costs, longer start-up durations, and specific material requirements to ensure the stability of the membrane electrode assembly Hart & Hörmandinger (1998).

5. Molten carbonate fuel cell (MCFC): The MCFC is a high-temperature fuel cell with operational temperatures between 550 to 700°C. It utilizes molten carbonate salts, especially lithium and potassium carbonates, as its electrolyte. Both its anode and cathode are made using nickel-based powders Wu, Zhang & Ni (2016). MCFCs are lauded for their efficiency and their ability to employ CO_2 for carbon capture and storage purposes. They operate at such high temperatures that costly noble metals aren't needed, enhancing cost-efficiency. Despite these advantages, MCFCs grapple with issues like corrosion, extended start-up durations, restricted material selection, and handling the molten carbonate Abdelkareem *et al.* (2021).

6. Solid oxide fuel cell (SOFC): Solid oxide fuel cells (SOFCs) are recognized for their efficient performance and adaptability to multiple fuels, including methanol and biogas. Not requiring noble metals, they are cost-effective with an impressive lifespan reaching 80,000 hours. Yet, their high operational temperatures restrict material choices that can maintain stability. Operating

between 600 and 1100°C, their electrolytes often consist of Yttrium stabilized zirconia (YSZ). Materials for the cathode, like Lanthanum Strontium Manganite (LSM), are chosen for their stability and conductivity, while nickel-based YSZ anodes enhance hydrogen oxidation rates Abdelkareem *et al.* (2021).

1.2.2.1 Selection of PEMFC for the Design

Among the diverse array of fuel cell technologies available, the PEMFC emerges as the most suitable choice for our design framework. The decision to deploy PEMFC is anchored on several pivotal attributes:

1. Operational Advantages: The PEMFC is lauded for its rapid start-up capabilities, notable power density, and optimal operational temperatures.

2. Fuel Efficiency and Environmental Considerations: Leveraging hydrogen as its primary fuel, a resource which is both abundant and clean, PEMFC operation does not result in the release of harmful pollutants Instead, the primary byproducts are gentle: heat and water.

3. Performance Metrics: The PEMFC can generate power up to a commendable 132KW at a temperature of 80°C. Moreover, its continuous power provision coupled with a substantial operational lifespan of 20,000 hours reinforces its reliability.

4. Cell Configuration and Voltage: A singular PEMFC cell, when operating under open-circuit conditions, exhibits a voltage range of 0.8 to 1.2 volts. For enhanced voltage and power outputs, these cells wisely combined to form a stack, connected in configurations of series and parallel. Commercially available PEMFC stacks typically proffer operational voltages spanning 26 to 50 volts.

5. Sustainability and Recyclability: A noteworthy feature is the capacity for reverse osmosis to repurpose the hydrogen residing in the byproduct water, underscoring the system's commitment to sustainability Mitra, Arya & Gupta (2023a) Mitra *et al.* (2023b).

Considering these advantageous features, the adoption of PEMFC technology not only aligns with the technical requisites of our design but also resonates with our sustainability ethos.

1.2.3 Fuel Cell Polarization Curve

The polarization curve serves as a foundational method in fuel cell assessment, defining the relationship between cell voltage and current density. A representative polarization curve for a PEMFC is illustrated in Figure 1.9.

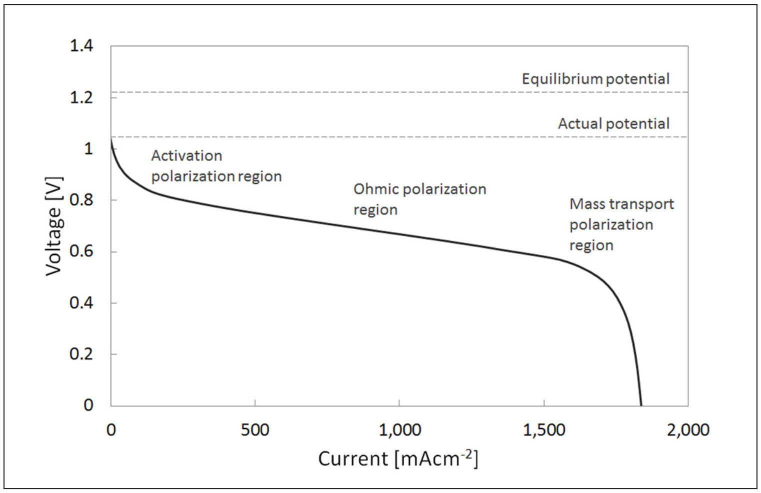

Figure 1.9 Polarization curve of a PEMFC highlighting the activation, ohmic, and mass transport regions

Taken from Valle (2014)

This curve is typically constructed in a quasi-steady-state condition, wherein the current remains consistent until voltage stabilization. However, linear alterations in the current can also generate these curves. In addition to increasing or decreasing the current, random values can also be used to create polarization curves. The common practice is to record with increasing and then decreasing values, averaging the results for each data point. Polarization curves serve as a varied diagnostic tool for assessing fuel cell efficiency and the impact of alterations in specific operational parameters. Such a curve permits the identification of kinetic, ohmic, and mass transport losses. The initial segment of the curve, characterized by minimal current densities, is termed the activation polarization zone. Here, there is a notable decrease in cell potential, attributed to the slow kinetics of the oxygen reduction reaction. As current densities escalate, the curve exhibits a linear descent for most parts of the plot. This phase referred to as the ohmic polarization stage, shows voltage drops dominantly due to ohmic resistance, with the voltage decrease correlated to current density. The resistances in this phase pertain to electronic movement via the electrodes and protonic transmission through the electrolyte. The curve's final segment, observed at elevated current densities, is governed by mass transport and is labeled the concentration polarization zone. Here, The gas diffusion layer and catalyst layer produce pore structures that limit the transport of reactant gases through this region, resulting in dramatic decreases in cell performance. Fuel and oxygen are mixed in the electrolyte, and a short circuit within the cell causes the difference between the actual potential and its theoretical maximum potential. By multiplying potential with current density at various points, one can deduce the power density versus current density graph from the polarization curve. While the polarization curve offers information about the overall fuel cell operation, it fails to elucidate the performance of individual components or specific processes. As polarization curves cannot be generated during regular fuel cell function, and considerable time is required for the measurement, it may prevent the characterization of certain time-sensitive processes in the fuel cell. These curves are widely used to examine how different catalysts and their degradation affect fuel cell performance. While they may not provide detailed information about the catalyst itself, they are crucial for assessing the general health of the fuel cell Valle (2014).

1.3 Battery Dynamics and Performance Metrics

In this section, the focus is on the fundamental aspects of battery technology and its critical role in energy storage systems, particularly within FCEVs. This section also explores the various parameters that determine battery performance, highlighting the importance of efficient energy management. Furthermore, it delves into the essential concepts of State of Charge (SOC) and State of Health (SOH), detailing their definitions, importance, and the methodologies employed for their assessment. Through this section, a comprehensive understanding of the factors that influence battery efficacy and longevity in FCEVs will be discussed.

1.3.1 Introduction to Batteries: The Case for Lithium Iron Phosphate $LiFePO_4$

This section discusses battery types and energy storage essentials for FCEVs. Different types of batteries suit different applications, thus requiring recognition of their distinct characteristics. In this study, we focus primarily on Lithium Phosphate Iron ($LiFePO_4$) batteries in the context of the model we used. Comparative studies have demonstrated that $LiFePO_4$ batteries outperform lithium cadmium, lead-acid, lithium cobalt, and nickel-metal hydride batteries. Several key performance metrics were considered for this evaluation, including energy conversion efficiency, capacitance, lifespan, ecological impact, temperature tolerance, and operational performance under heavy-duty charging and discharging cycles. The low toxicity and pollution-free of $LiFePO_4$ batteries make them highly sustainable as well as highly reliable. They are capable of handling intense charge and discharge cycles, making them an ideal power supply for common electric vehicles. The availability of their raw materials also enhances their appeal from the standpoint of the supply chain. $LiFePO_4$ batteries show inconsistent changes in their internal resistance while being charged and discharged, affecting their technical performance. Research has shown a close relationship between the current, battery voltage, and resistance within the battery during these processes. When the battery is discharging, it can be modeled with a third-order polynomial equation that accurately represents its internal resistance and potential. This modeling produces results with minimal relative error, regardless of the voltage level at which the battery is discharging Parikh, Shah & Prajapati (2023). By considering the mentioned characteristics of $LiFePO_4$, it is selected for this study as the most suitable option. In the following section, detailed specifications of $LiFePO_4$ and all modeling data which has been used are demonstrated.

1.3.2 $LiFePO_4$ Batteries Performance: Comparative Advantages and Detailed Specifications

Compared with other lithium battery types, $LiFePO_4$ battery packs offer high energy conversion efficiency, reaching up to 95%, and a considerably longer life cycle, offering up to 2000 charge cycles compared with 400 to 500 cycles in other lithium battery types. These batteries can also be utilized to power electric motors and to manage power in a variety of applications, such as electric scooters, purely electric vehicles, and hybrid vehicles. It is expected that $LiFePO_4$ batteries will become the leading choice for applications in electric vehicles in the future as a result of these advantages Tseng, Huang, Chen & Tsai (2018).

1.3.2.1 Analyzing Charging and Discharging: Internal Resistance and Equivalent Circuit in $LiFePO_4$ Batteries

As illustrated in Figure 1.10, V_b is the battery pack's internal voltage, and R_{in} is the battery's internal resistance. In most cases, R_{cov} and C are not included in an equivalent circuit for a battery. It is however more accurate to simulate over-voltage conditions by adding the resistor R_{cov} in parallel with the capacitor C, and then in series with the rest of the circuit. Through this addition, the charging process depicted in this circuit diagram is more reflective of real-world conditions, overcoming the limitations of a basic linear model and improving its precision. R_{eq} is the total resistance observed by the voltage source. When the capacitor C does not conduct, R_{eq} influences the over-voltage effect, and it can be calculated using Equation 1.2 shown Tseng *et al.* (2018).

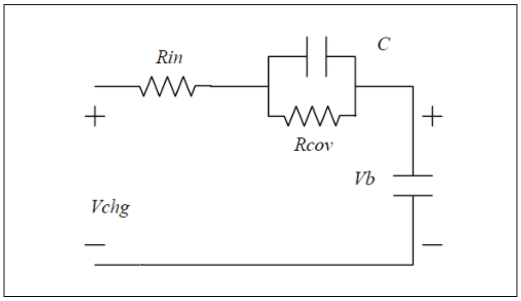

Figure 1.10 Equivalent circuit diagram of a $LiFePO_4$ battery pack illustrating internal resistance and over-voltage simulation

Taken from Tseng *et al.* (2018)

$$R_{\text{eq}} = R_{\text{in}} + R_{\text{cov}} \tag{1.2}$$

1.4 PI Controllers

In this section, we focus on Proportional-Integral (PI) controllers, a critical element in our FCEV system. PI controllers are known for their effectiveness in maintaining stable and accurate control by adjusting to the difference between a desired setpoint and the actual system state. They do this through their two parts: the proportional part tackles the current error, while the integral part manages past errors. This dual-action is particularly beneficial for our FCEV's systems, such as the speed loop and the fuel cell current control loop, ensuring precise speed regulation and optimal fuel cell efficiency John D (2022).

These controllers play a vital role in balancing performance and energy efficiency, enhancing both the reliability and effectiveness of our energy management strategy. Furthermore, PI controllers' ability to adjust outputs considering both steady-state and accumulated errors makes them indispensable in complex systems, including advanced applications like our heavy-duty FCEV conversion Electronics Coach (2023), Sandeep (2021).

This section delves deeper into PI controllers' functioning and their significance in our FCEV model's enhanced energy management.

1.4.1 Control System Analysis

In the field of control engineering, the decision to use time domain or frequency domain analysis for a system raises many questions about its application and purpose. System analysis is the understanding of the system and its operations or functions. This analysis can be done qualitatively or quantitatively. Qualitative analysis is a descriptive analysis of the system and its performance, but the nature of the project makes it difficult to accurately compare systems based on this type of analysis. The quantitative analysis, on the other hand, focuses on the measurable and specific parameters of the system. Determining these parameters is difficult, but once determined, it becomes increasingly easy to compare different systems. For example, consider evaluating two cars for sale. A quality assessment may involve test driving the vehicle and recording observations such as smoothness, speed and acceleration. However, these descriptions are subjective and may not reflect actual experience. On the other hand, quantitative measurements, such as the acceleration time from 0 km/h to 100 km/h or the maximum speed of the vehicle, provide meaningful data, to facilitate comparisons. The quantitative analysis of the system is divided into two parts according to the response time: time domain analysis and frequency domain analysis. Each has its own unique and effective approach to system evaluation. Time domain analysis involves observing and measuring a system's behavior over a period, making it ideal for systems that exhibit changes gradually. This method captures the dynamics of a system as they occur over time, providing a clear understanding of its evolution and response patterns.

Frequency domain analysis, on the other hand, focuses on how a system responds to varying frequencies. It's used for systems that change rapidly, analyzing their behavior under different frequency conditions. This method is particularly useful for understanding the fast dynamics of a system that might not be as apparent in the time domain Sandeep (2021).

For the purposes of this thesis, we concentrate on time domain analysis. Our system's characteristics and the nature of the changes it undergoes are more suited to this method. The time domain analysis allows us to observe and measure the system's response over time, providing a comprehensive understanding of its behavior, which is crucial for our study.

1.4.1.1 LTI Second-Order System

Linear Time-Invariant (LTI) systems are foundational in control theory, characterized by their linearity and time invariance. Linearity implies that the system's output for a linear combination of inputs equals the same combination of individual outputs, adhering to the principle of superposition. Time invariance suggests that the system's behavior remains constant over time, meaning a time-shifted input results in an equivalent time-shifted output. LTI systems are crucial in the field of control systems due to their predictable behavior and ease of analysis. They find extensive application in designing and understanding control systems, particularly in signal processing, communications, and automated control mechanisms. Their predictable responses to inputs and stability over time make them ideal for analyzing and designing a wide range of control systems Lathi (2006).

In the context of LTI systems, we will now derive the response of a standard second-order control system to a step input. Figure 1.11 illustrates the step response characteristic of such a second-order system and Equation 1.3 gives the closed-loop transfer function.

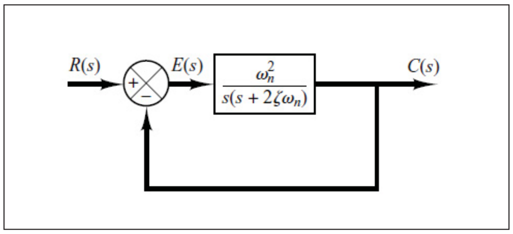

Figure 1.11 Simplified block diagram illustrating the step response for a second-order system, including its closed-loop transfer function

Taken from Ogata (1999)

$$\frac{C(s)}{R(s)} = \frac{\omega_n^2}{s^2 + 2\zeta\omega_n s + \omega_n^2} \tag{1.3}$$

As the damping factor ζ of the system varies from ∞ to 0, the pole positions are depicted in Fig 1.12. With a reduction in ζ, the poles converge along the real axis. When ζ decreases further, a pair of conjugate poles travels in a quarter-circle path towards the imaginary axis. Depending on where the poles are situated, the system can exhibit one of three behaviors:

- For $\zeta > 1$: The system has distinct real poles and shows an overdamped transient response characterized by no overshoot and a slower rise time.
- For $\zeta = 1$: The system possesses coinciding real poles and displays a critically damped transient response, marked by no overshoot and a moderate rise time.
- For $\zeta < 1$: The system features complex poles, leading to an underdamped transient response with overshoot and a quicker rise time.

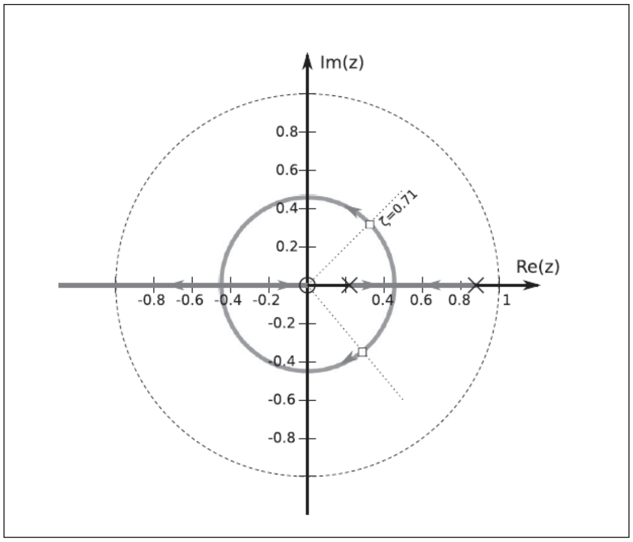

Figure 1.12 The positioning of poles in a second-order system shifts with a decrease in the damping factor ζ from ∞ to 0. When ζ equals 1, the system's real poles converge ($r_{1,2} = \omega_n$). Subsequently, the conjugate pole pair progresses towards the imaginary axis

Taken from Haidekker (2013)

Fig. 1.13 displays the step responses for a range of damping factor (ζ) values. A higher damping factor, such as $\zeta = 2$, results in a notably slow transient response. Reducing ζ to 1, where the poles coincide on the real axis, leads to the quickest response without any overshoots. Diminishing the damping further results in quicker rise times accompanied by overshoots. Extremely low ζ values cause the system to exhibit multiple oscillations. For optimal performance in a LTI second-order system, a damping factor of $\zeta = 1/\sqrt{2}$ is ideal, offering both rapid response and minimal overshoot Ogata (1999).

1.4.1.2 Time domain Analysis of a System

In control systems, ensuring stability is essential. These systems need to meet specific standards, typically described in terms of how they behave over time or in response to different frequencies. The most important aspect is making sure the system is stable, as only a stable system can work

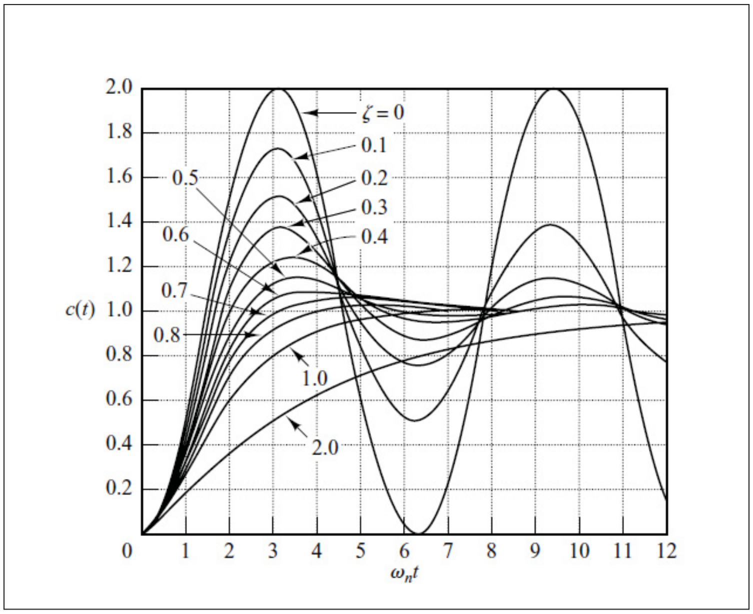

Figure 1.13 Normalized step responses of a second-order system for some values of the damping factor. From $\zeta = 10$ to $\zeta = 0.5$, a lower damping factor gives rise to faster response and more overshoot

Taken from Ogata (1999)

correctly. When designing controllers, the main goal is to keep the system stable, which involves managing factors like steady-state error and how the system reacts to changes in gain or phase.

To evaluate how well a system performs, we often look at how it responds to various inputs, like constant or gradually increasing signals. The system's reaction to these inputs, particularly its steady-state error, tells us a lot about its performance. We also consider how sensitive the system is to internal changes or outside disruptions.

A key function in many control systems is to have the output closely match the input, especially in terms of how quickly it can respond. This is assessed by examining the system's immediate reaction to sudden changes. The step response is a common way to measure this, providing insights into the system's speed and stability Bunzemeier & Litz. The following Figure 1.14 illustrates the step response of a system, showcasing how it reacts to a sudden change.

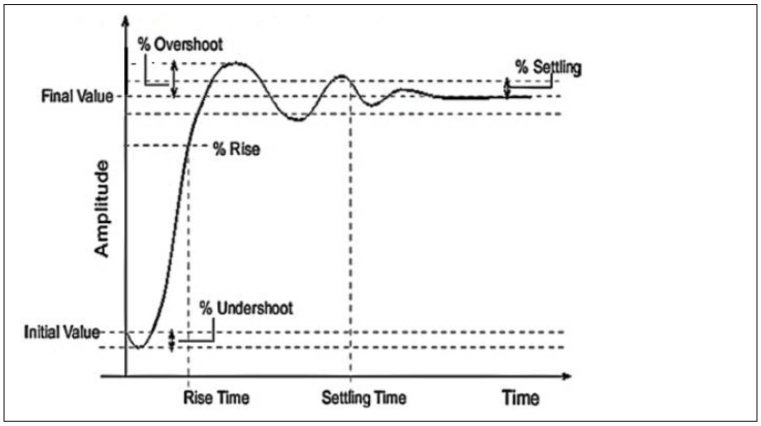

Figure 1.14 Illustration of system step response

Taken from Bawa, Omeiza & Amlabu (2019)

Rise time (t_r) reflects how quickly the system responds, measured as the duration for the response to go from 10% to 90% of its final value.

Delay time (t_d) represents the time taken for the system's response to reach a noticeable level, typically 50% of the final value, after it's initially excited.

Settling time (t_s) is the period after which the response remains within a certain range of tolerance.

Overshoot (M_p) is the peak amount by which the system's response exceeds its final value, usually shown as a percentage of that final value.

1.4.1.3 Analysis of System Control in the Time Domain with PI Controllers

In time domain control, when a step input is applied to a system, the ideal response would be an immediate step output with no overshoot, rise time, or settling time. However, achieving this perfect response is not possible with any damping value in the system. The goal is to design an optimal system that has the smallest possible rise and settling times with zero overshoot. This is often achieved using an underdamped system in a closed loop with an appropriate controller.

Although an underdamped system has low rise and settling times, it tends to have overshoot, which needs to be minimized using the controller Electronics Coach (2023).

The PI controller is a popular choice due to its simplicity and effectiveness. One key advantage of the PI controller is its conceptual simplicity, particularly the integration aspect, which most engineers can grasp and implement without needing an in-depth understanding of control theory. Despite its simplicity, the PI controller is sophisticated in capturing the system's history through integration. In this subsection, we will explore how each parameter of the PI controller affects the dynamics of a closed-loop system. Figure 1.15 demonstrates a unity feedback system, providing a visual representation of this concept.

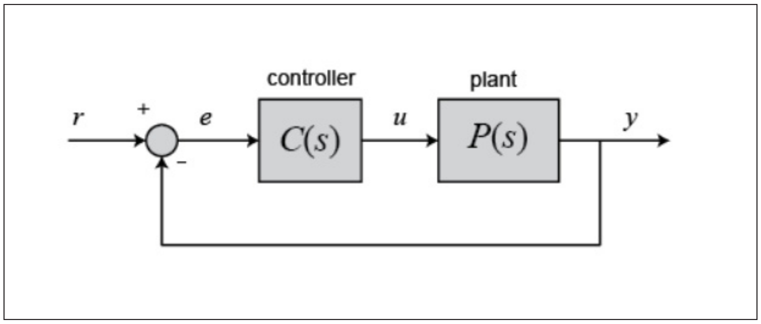

Figure 1.15 PI Controller

Taken from CTMS (2023)

When a plant's output doesn't meet system requirements, using a closed-loop control system can be an effective solution. In such systems, the controller is driven by the error between the actual output and the desired output. The controller then generates corrective actions to align the plant's actual output with the desired one.

A simple method involves creating an actuating signal that is proportional to the error. The greater the error, the stronger the actuating signal. This is the basis of the Proportional controller, which is effective as long as the error remains within certain limits. However, for errors that exceed a threshold, a Proportional controller alone may not suffice.

Two main types of errors are considered:

1. Transient Error: This error occurs due to the delay in the plant's response to input changes. If the gain of the Proportional controller is increased to reduce this delay, it can lead to overshoots and oscillations, creating transient errors. Hence, it's crucial to monitor the rate of change of the error.

2. Steady-State Error: This error arises when the plant is unable to reach the set point due to inherent limitations. In such cases, considering the integral of the error over time provides a clearer picture of the steady-state error. An Integral controller, which focuses on the accumulated error over time, can effectively minimize this steady-state error, especially in noisy conditions.

The PI Controller combines these two approaches. It uses proportional control to expedite settling and integral control to address errors that persist over time. This dual approach enhances the plant's performance, ensuring both quick response and reduced steady-state errors Sandeep (2021).

The output generated by a PI controller, corresponding to the control input for the plant, is computed in the time domain based on the feedback error in the following Equation 1.4 CTMS (2023):

$$u(t) = K_p e(t) + K_i \int e(t)\, dt \tag{1.4}$$

In the presented equation, $u(t)$ signifies the control action output of the PI controller at any given time t. This output is a combination of two terms. The first term, $K_p e(t)$, represents the proportional component where K_p is the proportional gain coefficient and $e(t)$ is the instantaneous error between the desired setpoint and the actual system output at time t. This term ensures the control action is proportionate to the current error. The second term, $K_i \int e(t)\, dt$, embodies the integral component, with K_i as the integral gain coefficient. The integral of the error over time, $\int e(t)\, dt$, accumulates past errors, providing a corrective signal based on the historical sum of errors.

1.5 Energetic Microscopic Representation in Fuel Cell Hybrid Electric Vehicles

In the domain of complex system representation, particularly for HEVs, various modeling topologies and formalisms are employed. Among these, the Energetic Macroscopic Representation (EMR) stands out as a significant approach for the causal functional modeling of such vehicles. EMR is particularly noted for providing a macroscopic energetic view, offering detailed insights into the energetic functions of the system. This formalism is distinguished by its unique inversion rules, which systematically aid in constructing the local control structure of complex systems. These aspects of EMR, along with its inversion-based control, are integral to the control design and energy management in HEVs Syed (2012). In this thesis, we aim to utilize the EMR methodology, which has been extensively applied in various fields, including HEVs Lhomme, Bouscayrol & Barrade (2004), wind energy conversion systems Koita, Payman, Dakyo & Hissel (2018), and fuel cell systems Chrenko (2008). The objective is to define and develop the control system of a FCEV using the principles of EMR. This approach will provide a structured and systematic framework to analyze and design the FCEV's control system, ensuring optimal performance and efficient energy management. EMR's proven effectiveness in diverse applications suggests its potential for significant contributions to the advancement of FCEV technology Syed (2012).

1.5.1 Fundamentals and Pictorial Representation in EMR

A paraphrased version of the sentence with an explanation of the four steps involved in EMR and its inversion-based control could be:

Implementing EMR with its inversion-based control approach involves a four-step process for effective control design. These steps include:

- System Model Organization: Initially, the system model is structured in accordance with EMR principles.
- Analysis and Inversion of the System's EMR: The next step involves analyzing the system's EMR and performing its inversion.

- Simplification and Estimation: This stage focuses on simplifying the model and estimating relevant parameters.
- Development of Strategy: Finally, a strategy is formulated based on the simplified and estimated model Keyu (2010).

1.5.1.1 Organizing the System Model According to EMR

EMR is a visual method for structuring models of actual processes for control applications. It relies on the action-reaction principle to arrange sub-systems connections based on physical causality, specifically integral causality. This approach emphasizes the system's energetic characteristics, focusing on how energy is stored, converted, and distributed Keyu (2010).

- Principle of action and reaction:

  The flow of power through interconnected components or energy sources involves a dynamic interplay of *action* and *reaction* forces. Consider a scenario where a battery, designated as a voltage source s_1, interfaces with an inductor, a representative of a current source s_2, as depicted in Fig. 1.16. The voltage across the battery v_{bat} represents the action force, while the inductor's current i_L serves as the reaction force in this interaction, as illustrated in Figure 1.16. The instantaneous power transmission within the system is the product of the action force v_{bat} and the reaction force i_L. It's important to note that the directionality assigned in an EMR model is fundamentally a matter of established convention Keyu (2010).

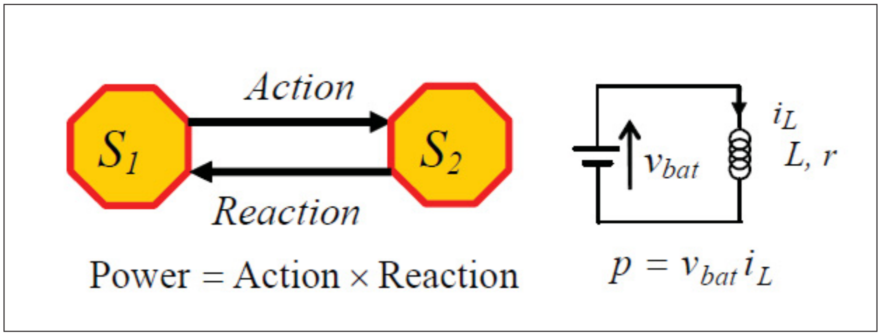

Figure 1.16 Illustration of the Principle of Energetic Interactions

Taken from Keyu (2010)

- Concept of Integral Causality in EMR:

  EMR follows the concept of integral causality, considered the accepted reason-and-effect relationship in systems that change over time. Integral causality means that the previous data of a system (prior to a certain point in time) is computed through integration, and the predictive trends (post that point-future data) through differentiation. Simply put, integral causality in EMR defines inputs to the system as causes and the resulting integrations as effects (outputs). For instance, in an inductor-based system, voltage is treated as the initiating cause (input), and the generated current as the resultant effect (output), which opposes the behavior in systems with capacitive characteristics. Unlike capacitors or inductors, a resistor's role as input or output is not time-dependent but varies according to the system it's integrated with, reflecting its adaptable nature in electrical circuit components. Figure 1.17 illustrates this fundamental principle of EMR.

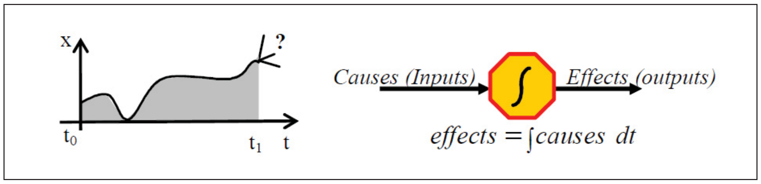

Figure 1.17 Graphical Representation of Integral Causality

Taken from Keyu (2010)

- EMR Core Components and pictograms:

  The EMR categorizes system elements into four primary types: elements that generate or use power, known as source elements; elements that store power, known as storage elements; elements that change the form of energy, referred to as conversion elements; and elements that connect different parts of the system, termed as coupling elements. Figure 1.18 shows the EMR basic elements in pictograms Chen, Bouscayrol & Lhomme (2008).

  - *Source Elements* are the system's terminal nodes that either supply or utilize energy, exemplified by a battery.
  - *Storage Elements* are depicted by rectangular symbols with a diagonal line and are responsible for holding energy, providing the state variables of the system, such as the energy in a capacitor.

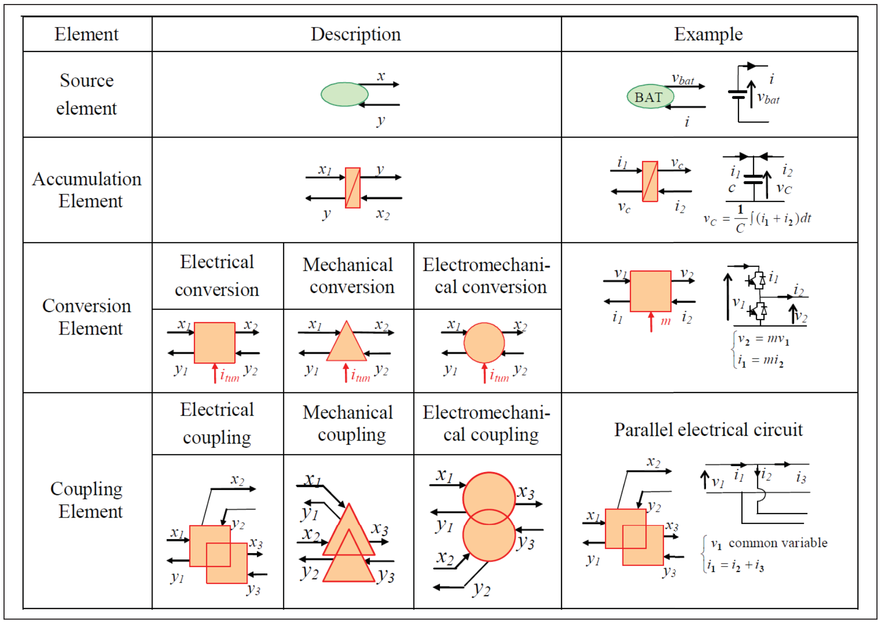

Element	Description			Example
Source element				
Accumulation Element				$v_C = \frac{1}{C}\int(i_1+i_2)dt$
Conversion Element	Electrical conversion	Mechanical conversion	Electromechanical conversion	$v_2 = mv_1$ $i_1 = mi_2$
Coupling Element	Electrical coupling	Mechanical coupling	Electromechanical coupling	Parallel electrical circuit v_1 common variable $i_1 = i_2 + i_3$

Figure 1.18 Graphical Representation of Integral Causality

Taken from Keyu (2010)

- *Conversion Elements* are portrayed as shapes that indicate the type of energy conversion without storage, including squares for electrical, circles for electromechanical, and triangles for purely mechanical conversions.
- *Coupling Elements* are shown as overlapping shapes and are essential for the distribution of energy across the system Chen *et al.* (2008).

1.5.1.2 Analysis and Inversion of the System's EMR

Systematic extraction of control protocols from EMR is achievable via specialized inversion methodologies. The process initiates by designating tuning pathways that align with the system's objectives and restrictions, commencing from the tuning variables and progressing systematically toward the objectives. Following this, the paths for control are deduced by reversing these initial paths, resulting in the generation of control blocks. These blocks are symbolized by pale blue parallelograms, signifying their informational processing role Keyu (2010). For a comprehensive understanding, Figure 1.19 provides an illustrative overview of the EMR alongside its inversion-based control mechanism.

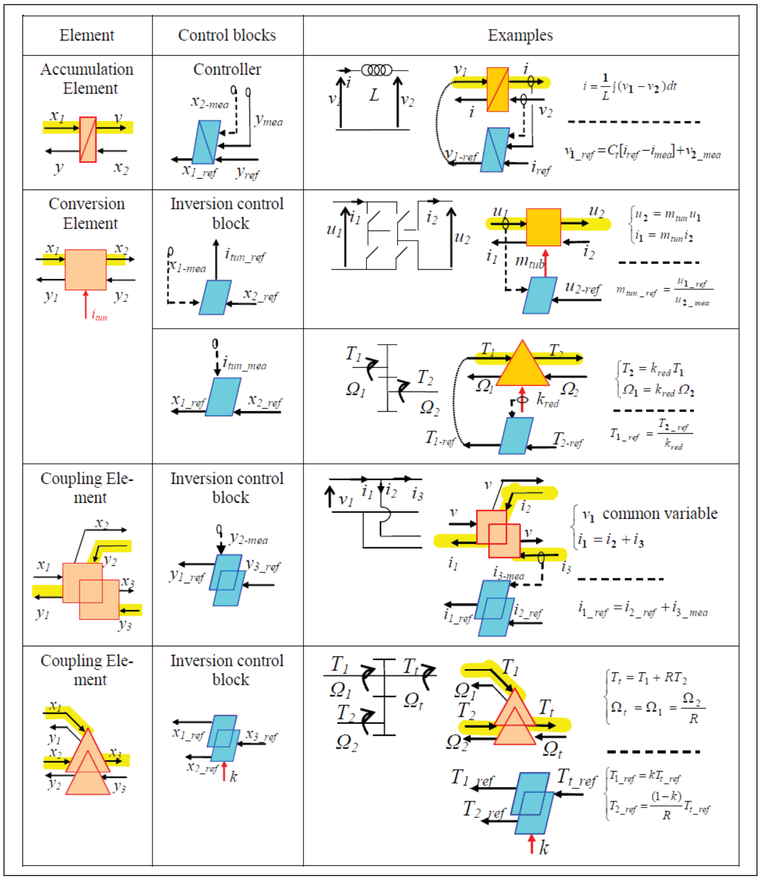

Figure 1.19 Illustrative overview of EMR and the corresponding inversion-based control mechanism

Taken from Keyu (2010)

Elements that accumulate energy, shown as rectangles intersected by a diagonal, are indicative of a dynamic relation and lack the capacity for direct inversion, thus necessitating a controller's presence for reversal operations. The route from the output back to its input reference is created, turning the output back to match the intended input. Sensors, denoted by small encircled measurement markers, are implied by measurement variables. Solid arrows bearing sensors dictate essential measurements. Where the measurement of x_2 can be adjusted or disregarded, a dashed line symbolizes its elective status Keyu (2010).

For elements converting energy, represented as squares, direct inversion is possible given stationary conditions. An example within the EMR diagram is an electric conversion element, where the tuning journey initiates at $u1$ and leads to $u2$. Here, the modulation variable m_{ub}, governing the converter's switching function, is directly linked to the relationship between $u1$ and $u2$. With mechanical conversion elements, the tuning commences from an output torque T, reversing directly from the standard torque $T_{2,\ ref}$ to $T_{1,\ ref}$, provided the gear ratio k_{red} is known Keyu (2010).

Coupling elements, portrayed as superimposed figures, might need extra inputs to reverse. An electrical coupling element's inversion, for instance, starts from $i1$ and is directed towards $i2$ and $i3$, with $i2_{ref}$ being deduced from an additional $i3_{mea}$ input. Similarly, the depiction of a mechanical coupling element's inversion shows torque $T1$ as the tuning origin, extending towards T_r. To determine the reference torques $T_{1,\ ref}$ and $T_{2,\ ref}$ from $T_{r,\ ref}$, an additional distribution ratio k is imperative Keyu (2010).

1.5.1.3 Simplification and Estimation

In the process of simplification and estimation control structures, certain reductions are made to align with system demands and trade-offs. Although it is generally presumed that all system variables can be quantified, in reality, some prove challenging to measure. Consequently, appropriate estimations are devised. When constructing necessary estimators, segments of the EMR can be utilized directly. These estimation segments mirror the configuration of standard EMR modules, with the distinction being their purple hue to denote their estimating function Keyu (2010).

1.5.1.4 Strategy

A strategic layer, depicted in dark blue in Figure 1.20, is established to oversee the energy management of the entire system. The control architecture derived from the EMR constitutes the *local control level*, while the overarching strategy functions as the *global management level* Keyu (2010).

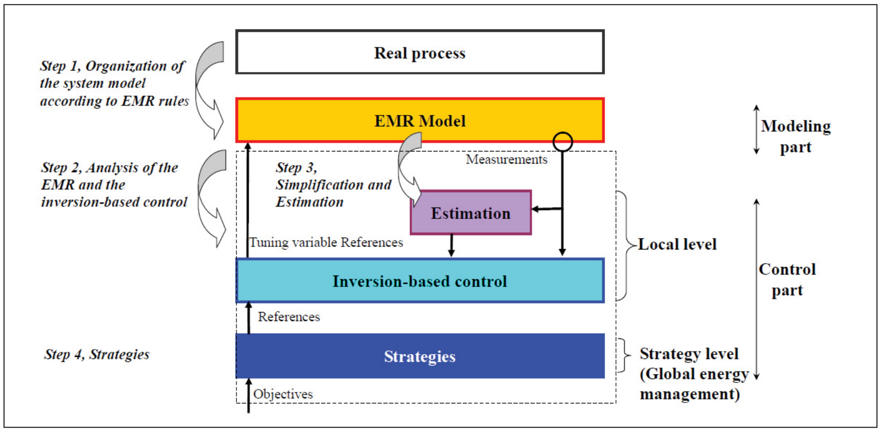

Figure 1.20 Illustrative overview of EMR and the corresponding inversion-based control mechanism

Taken from Keyu (2010)

As seen in Figure 1.20, by following a four-step process, we can create a control structure rooted in EMR principles, featuring two main parts: the local level for managing specific parts of the system and the strategic level for overseeing the entire system's energy use. The goal is to build a control setup that works for complex systems. For more on creating sturdy control systems and making control strategies Keyu (2010).

CHAPTER 2

METHODOLOGICAL FRAMEWORK FOR SYSTEM DESIGN USING EMR

This chapter outlines the approach taken to design the system, starting with an introduction to the advanced EMR, which serves as a tool to visually map out the system's intricate workings and provides an in-depth understanding of how it operates. It then progresses to analyze the system's methodical framework, focusing on two key areas: TS and the ESS. The chapter delves into how these subsystems interact with one another, highlighting how they function together to ensure the system operates effectively as a whole.

2.1 Introduction to the EMR Analysis of the FCEV Powertrain

Chapter 1 introduced the powertrain as the heart of the FCEV, consisting of two main subsystems: the ESS and the TS. This chapter aims to dissolve the complexities of these subsystems and their determining roles in the FCEV's operation. ESSs are crucial as they store energy and assist the fuel cell in meeting the vehicle's fluctuating power demands, directly impacting the FCEV's overall efficiency and capability. They must be adept at managing high-power needs, such as during cold starts or sudden power demands.

In the previous chapter, we examined the components of an FCEV, including the powertrain schematic highlighting the Energy Storage System and the Traction Subsystem. Moving forward, this chapter will guide us through the Energetic Macroscopic Representation of the powertrain, paving the way to a comprehensive study of the system. The modeling process for each subsystem will be explored using EMR, laying the foundation for understanding the inner workings of the FCEV.

2.2 Decoding EMR Representations in FCEV Powertrain

The powertrain of the FCEV is transformed into an EMR for the purposes of this study, as depicted in Figure 2.1 This conversion into EMR provides a comprehensive view of the system's configuration. To thoroughly understand the EMR, we begin by studying its pictograms for both the TS and the ESS. Each subsystem within the EMR is analyzed in three distinct sections: modeling, control, and strategy, as previously introduced in Chapter 1. This approach allows for a detailed examination of the EMR's application in understanding and optimizing the FCEV's powertrain.

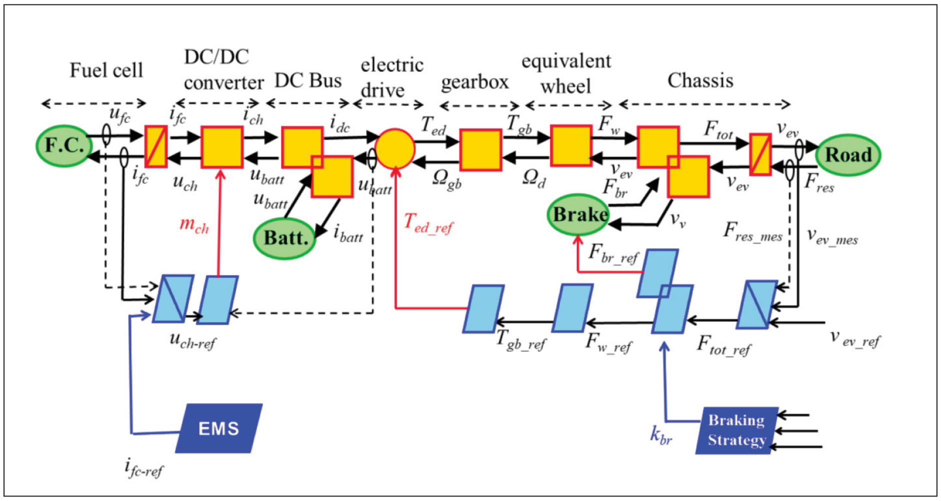

Figure 2.1 EMR Overview of the FCEV

Taken from Noura (2022b)

2.3 Introduction to Pictograms

EMR excels in modeling intricate systems, which can often be segmented into various smaller components. Take a car, for instance; it can essentially be viewed as a combination of a storage unit (fuel tank), an engine, a shaft, and wheels. Each of these components plays a vital role in managing the flow of power, which in this context flows from the storage unit to the road. The EMR formalism employs specific pictograms, depicted in Figure 2.2, to represent these systems. Within the EMR framework, four primary elements are used to accurately depict this type of system Lenoir, Trovao, Ta & Messier.

2.3.1 The Source element

In the EMR framework, the *Source element* serves as the starting point for analyzing the system. It denotes the system's boundaries, represented in an FCEV by critical components such as the

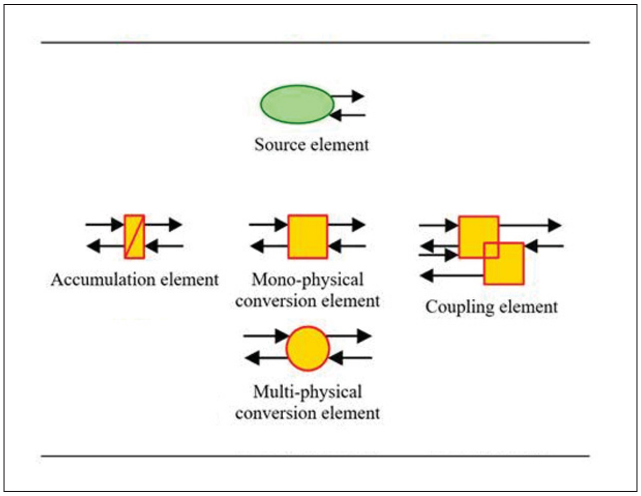

Figure 2.2 EMR Primary Pictograms Illustrating System Components

Taken from Lenoir *et al.*

battery, fuel cell, brakes, and traction force. This element reflects the underlying principle that energy transfers from one source to another, emphasizing how the system manages this energy flow.

In our FCEV system, we define the following components as source elements, each marking a boundary or a key functional limit within the EMR framework:

- **Environment:** Represents the traction force, involving external forces and conditions that the vehicle encounters.
- **Brakes:** Symbolize the vehicle's braking mechanism, a vital aspect of vehicle control and safety.
- **Battery Pack:** Acts as an energy storage unit, crucial for the vehicle's electrical needs.
- **Fuel Cell:** The primary source of energy, pivotal for the vehicle's propulsion and overall operation.

These elements collectively outline the framework of our system, highlighting the transition and management of energy within it.

2.3.2 The Conversion elements

Figure 2.2 illustrates the two converter categories in the EMR framework: *monophysical conversion* and *multiphysical conversion*. In monophysical conversion, the energy remains the same type at both the input and output of the converter. Conversely, multiphysical conversion involves a change in the type of energy within the converter. This is exemplified by an electric motor, which transforms electrical energy into mechanical energy. Unlike source elements, these converters have dual input and output channels, reflecting their role in both receiving and transmitting power. These channels represent the action and reaction paths that occur before and after conversion. Examples of converters include gearboxes and choppers (used in power electronics) for monophysical conversion, and electric motors or engines for multiphysical conversion Lenoir *et al.*.

2.3.3 The Accumulation element

The *Accumulation element* in the EMR framework captures the dynamic aspects of a system, signifying energy changes during state transitions. For instance, as a vehicle accelerates, it accumulates kinetic energy, primarily drawn from the fuel cell and battery. This process of energy accumulation is represented by yellow rectangles intersected by a red line as illustrated in Figure 2.2, with two input and two output paths, reflecting their role in the system's energy dynamics.

From a mathematical perspective, the presence of derivatives or integrals in our system modeling typically indicates an energy accumulation phase. Accumulation elements are where differential equations are applied, signifying temporary energy storage. This includes scenarios like inductors storing magnetic energy, inertia storing kinetic energy, or capacitors holding electrostatic energy Lenoir *et al.*.

2.3.4 The Coupling element

The *Coupling element* in the EMR framework plays a crucial role in either combining or splitting two power flows. This is a common occurrence in physical systems, exemplified in scenarios like Kirchhoff's current law or a car's differential. In the EMR pictograms, coupling for a single domain is indicated by overlapping yellow squares as it is depicted in Figure 2.2, while multi-domain coupling uses circles. These symbols represent the distribution of energy, suggesting that configurations like parallel or series connections, or transmissions, fall under coupling elements.

Mathematically, the presence of variable additions in a system model often points to a coupling element. These elements have an additional input and output compared to previously mentioned components. The extra ports are positioned either on the left or right side of the element, indicative of whether the power is being divided or merged. Coupling elements are particularly common in complex system models Lenoir *et al.*, such as our FCEV case study.

Incorporating coupling elements into a model often reveals missing equations necessary for a control loop. This necessitates the implementation of specific strategies, like EMS, which we will explore in more detail in Chapter 3.

2.3.5 The Tuning path

In the EMR framework, after finalizing the system representation, the next crucial step is defining the *Tuning path*. The tuning path is essentially a sequence of physical quantities that connect the controllable variables to the target variables we aim to influence Lenoir *et al.*. For our study, as illustrated in Figure 2.3, the goal is to apply control and establish tuning paths across all system blocks.

The tuning path is designed to relate the control variables directly to our primary objective variable, which for the TS case is the vehicle's speed, v_{ev}. The control variables we focus on are T_{ed_ref} (the reference electric drive torque) and F_{br_ref} (the reference brake force). We have structured the tuning path to correlate these control parameters with the vehicle's speed, traversing through all the system blocks.

This structured approach requires us to develop our control paths based on these tuning paths, involving the inversion of the elements we have defined in our EMR model. To clarify, this means we can regulate the entire TS primarily through T_{ed_ref} and F_{br_ref}. Our end goal is to align the actual measured speed of the vehicle with a desired *reference speed*, derived from our driving cycle. Achieving this alignment involves utilizing Inversion-Based Control (IBC) techniques, which we will delve into later in this chapter.

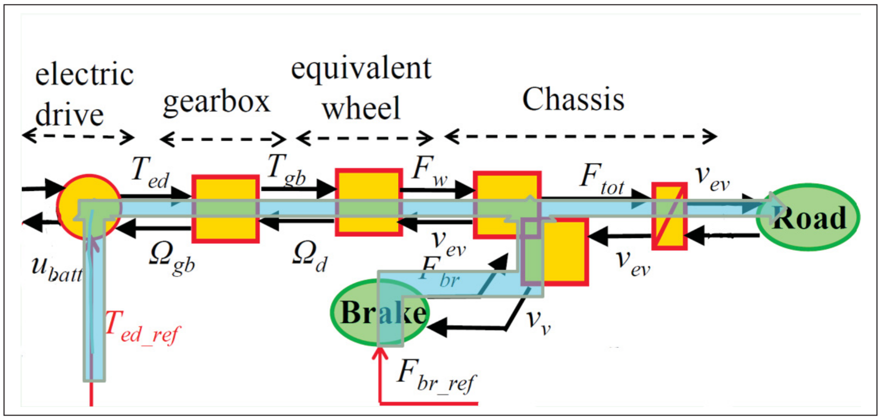

Figure 2.3 Illustration of the EMR tuning path, showcasing the interrelation between control variables T_{ed_ref} and F_{br_ref} and their impact on vehicle speed

Taken from Noura (2022b)

Similarly, the tuning path for the ESS is structured to link the control variable m_{hfc} directly to our primary objective variable, which is the fuel cell current, i_{fc}. The control variable, m_{hfc} modulates the proportion of fuel cell current that contributes to the electric drive's demand. In our energy management strategy, it is essential to regulate a single current source—either from the fuel cell or the battery—to meet the traction system's requirements, particularly the electric drive. Given that the fuel cell is the primary energy provider in our system, we choose to control the fuel cell current, thereby designating i_{fc} as the objective variable.

Following the development of the primary EMR layer, we establish the current control path within the IBC layer. Similar to the traction subsystem, a PI controller is employed to minimize the error between the actual fuel cell current i_{fc_mes} and the reference current i_{fc_ref}. This reference current will be optimized within the EMS block, which will be elaborately discussed in Chapter 3. Within the IBC layer, the control tuning variable, m_{hfc}, must be precisely tuned since the objective variable in our case is the fuel cell current i_{fc}. This detailed tuning ensures that the ESS effectively meets the system's energy demands, aligning with our overall energy management strategy.

2.3.6 The Inversion Based Control (IBC)

As discussed earlier, our objective for TS is to align the vehicle's actual speed v_{ev} with the reference speed v_{ev_ref}. This goal is pursued through the control variables T_{ed_ref} and F_{br_ref}. To achieve this, we establish a control loop within the EMR framework, which has been introduced as IBC. The tuning path is designed to relate these control variables directly to our primary objective variable, v_{ev}, passing through all the system blocks.

Similarly, the objective of the ESS is to align the actual fuel cell current i_{fc} with the reference fuel cell current i_{fc_ref}. This alignment is pursued through the control variable m_{hfc}. To achieve this, we also establish a control loop within the EMR framework, introduced as IBC. By precisely tuning m_{hfc}, we ensure that i_{fc} accurately meets the demands of the electric drive, thereby satisfying the energy requirements of the traction system. This process involves a PI controller to minimize the error between i_{fc_mes} and i_{fc_ref}, with the reference current optimized within the EMS block.

The principles and elements of the IBC are discussed in detail through the speed control loop within this section. The specific application of these principles for the ESS and fuel cell current control will be elaborated on later in Chapter 3.

The control loop is methodically structured by inversing each element in the modeling chain. The IBC principle is illustrated in Figure 2.4, but the IBC process starts with the later stages of the modeling chain and progresses backward towards the control variables. Each element in the main chain, such as traction or electric braking of an electric vehicle, has its unique inversion methodology. This systematic approach ensures the vehicle's speed matches the desired speed Lenoir *et al.*.

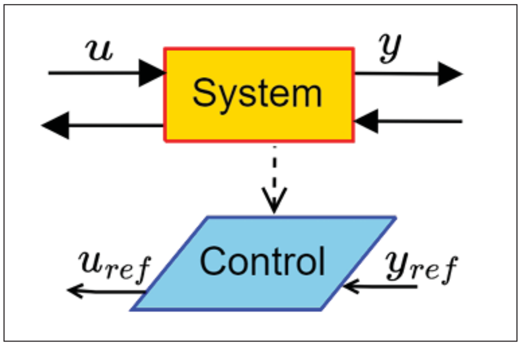

Figure 2.4 Illustration of IBC Principle

Taken from Lenoir *et al.*

Figure 2.5 highlights the initial point for integrating the IBC block in our study.

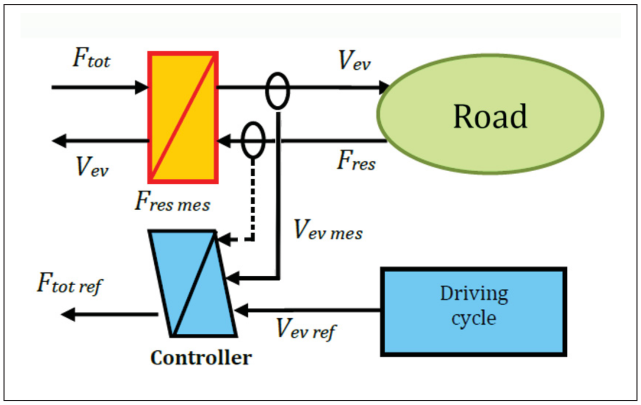

Figure 2.5 Identification of the Starting Point for IBC Integration: A schematic representation pinpointing the initial phase for IBC block implementation in the study

2.3.6.1 Inversion of conversion element

Conversion elements, due to their straightforward nature, are among the most fundamental components in the modeling sequence and are relatively simple to invert. As depicted in

Figure 2.4, the IBC block for a conversion element is illustrated. These elements are known for directly converting one form of energy to another without involving any complex mathematical equations like differential equations. Mathematically, this is expressed as shown in Equation 2.1. In the context of control blocks, these elements incorporate only a single input and output, focusing exclusively on the quantities associated with the action path Lenoir *et al.*.

$$\text{If } y(t) = kf(t) \text{ with } k \text{ constant, then } f(t)_{\text{ref}} = \frac{1}{k} y(t)_{\text{ref}} \tag{2.1}$$

2.3.6.2 Inversion of accumulation element

The accumulation element is the part that represents differential equations in their most basic form. Directly reversing these equations is not feasible as it produces erroneous results. Instead, the reverse process utilizes control systems, which are commonly referred to as controllers. We have a variety of controller models, but one particular kind is embedded in the reversing mechanism Lenoir *et al.*.

Currently, our design employs a PI controller for some key reasons. The first reason is to simplify the design process, allowing for an expedited initial simulation. The second is to lessen the system performance errors and disparity. This approach is also aligned with our well-structured design that monitors the operational aspects of our vehicle.

This is illustrated in Figure 2.6, while Equation 2.2 gives the functioning of the IBC within this context.

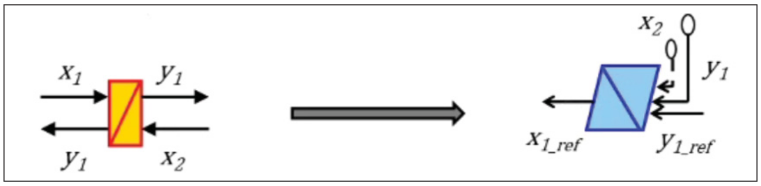

Figure 2.6 Schematic Representation of Accumulation Element Inversion via PI Controller Implementation

$$\begin{gathered}\text{If } y_1(t) = \int (x_1(t) - x_2(t))\, dt, \\ \text{Then } x_{1_{\text{ref}}} = C(t)[y_1(t)_{\text{ref}} - y_1(t)] + x_2(t), \\ \text{with } C(t) \text{ a controller}\end{gathered} \tag{2.2}$$

2.3.6.3 Inversion of coupling element

The inversion process for a coupling element is determined by the balance between the number of signals being controlled and the desired control signals. When these numbers match, the inversion process is straightforward, akin to a basic conversion element. However, if there are more variables to control than those being actively controlled, additional equations are necessary for the model, and a compromise must be identified. In such scenarios, the inversion of the coupling element introduces a new input variable, which should be managed through a strategy employing a strategy pictogram. This situation implies that not all variables can be perfectly managed. Conversely, if there is excess freedom in the coupling structure, it allows for the controlled variables to achieve their target values through various combinations of input signals Lenoir *et al.*.

Figure 2.7 presents a comprehensive table that encapsulates all the pictograms, providing an overview of the EMR basic elements along with the corresponding IBC blocks.

2.4 Traction Subsystem: Modeling Procedure and Analysis

In this section, our focus shifts to the traction subsystem. We will define and explain the modeling process for each component within this subsystem. This includes a detailed exploration of the mathematical equations that govern each block. Our approach is structured and sequential, beginning with the fundamental modeling layer. We then progress through the inversion-based control, enhancing our model's precision and functionality. Finally, we integrate the strategy

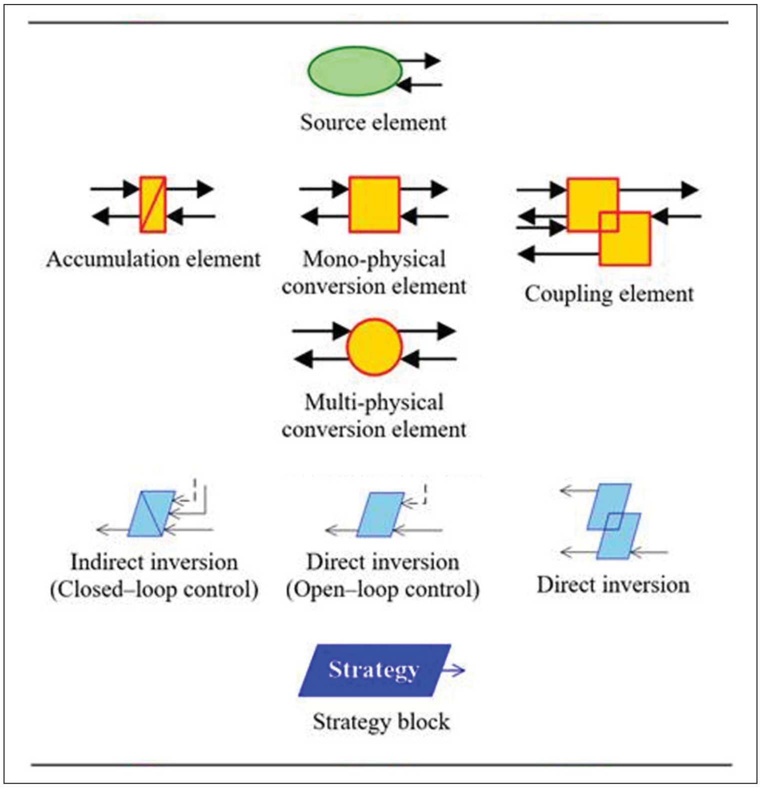

Figure 2.7 Overview of EMR Basic Elements and Their Corresponding IBC Blocks

Taken from Lenoir *et al.*

block, concluding in a comprehensive and robust model of the traction subsystem. This process is visually represented in Figure 1.20, guiding our discussion and analysis throughout this section.

2.4.1 The modeling layer

In this section, we delve into the complexities of the modeling layer for the traction subsystem, starting by establishing the system's boundaries.

Having established the system boundaries, we now turn our attention to additional elements in our modeling layer, including the electric drive, gearbox, wheels, and chassis, respectively.

First, the limits of our traction subsystem are primarily defined by three critical elements: the road, brakes, and the battery block. Each of these components plays a vital role in the overall functionality and performance of the subsystem. We begin our detailed exploration with the Road element.

2.4.1.1 Road Element

In this section, first we need to examine the operational dynamics of a PI controller within the traction subsystem of the vehicle to be able to elaborate on the *Road element* specifications and operational principles. This exploration will clarify how the PI controller contributes to the smooth and optimal functioning of the vehicle's propulsion mechanism.

To gain insight into the functional dynamics of the FCEV, it is crucial to first analyze the vehicle's mechanical behavior. The longitudinal forces influencing an FCEV are typically derived from a quintet of factors: rolling resistance, climbing force also known as uphill driving force, inertia force, aerodynamic drag force, and the resultant traction force. Essentially, the traction force is the sum of the first four forces and represents the force that propels the vehicle, channeling this energy through the wheels to facilitate motion. In an FCEV, the motion dynamics are governed by a set of established mathematical equations. The Equations 2.3 to 2.7 provide a framework for precisely calculating the mentioned quintet forces influencing the vehicle's movement Zhang & Yao (2015).

$$F_{trac} = F_f + F_c + F_a + F_d \tag{2.3}$$

$$\text{Rolling resistance:} \quad F_f = fmg\cos\alpha \tag{2.4}$$

$$\text{Uphill driving force:} \quad F_c = mg\sin\alpha \tag{2.5}$$

$$\text{Aerodynamic drag:} \quad F_d = 0.5C_D A\rho v^2 \tag{2.6}$$

$$\text{Inertial force:} \quad F_a = \dot{m}\frac{dv}{dt} \tag{2.7}$$

The longitudinal dynamics of the FCEV can be simplified by considering all the environmental forces as a single resultant force, F_{env}. This force represents the sum of all forces impacting the vehicle from environmental aspects, including rolling resistance F_f, uphill force F_c, and aerodynamic drag force F_d. The traction force F_{trac} is then described as the Equation 2.8. Through this simplification, the inertial force is obtained by subtracting the environmental force from the traction force. This simplification aids in the chassis model development.

$$\begin{cases} F_{env} & = F_f + F_c + F_d \\ F_{trac} & = F_a + F_{env} \end{cases} \Rightarrow m \cdot \frac{dv}{dt} = F_{trac} - F_{env} \tag{2.8}$$

Upon integrating both sides of Equation 1.15, we arrive at the subsequent Equation 2.9:

$$V_{ev}(t) = \frac{1}{M_{tot}} \int \left[F_{trac}(t) - F_{env}(t)\right] d_t \Rightarrow V_{ev}(t) = \frac{1}{M_{tot}} \int F_{tot}(t) d_t \tag{2.9}$$

In Equation 2.9, V_{ev} stands for the vehicle's speed, and M_{tot} is the vehicle's overall mass. F_{tot} represents all the forces that influence the vehicle's movement.

The *Road element* block is a pivotal component in our traction subsystem, serving as one of its foundational elements. This block has been adapted from the model used in the IEEE VTS Motor Vehicles Challenge 2017 Depature *et al.* (2016). However, to ensure compatibility with our system, we have adjusted specific parameters. These modifications are aimed at accurately reflecting the unique dynamics encountered by our FCEV which as mentioned earlier is a Class 8 C10 Caterpillar Kenworth 2002 truck. The adjusted road parameters, along with their implications for our model, are elaborated upon in the following. As we reviewed earlier, Equation 2.8 indicates:

$$F_{\text{env}} = F_f + F_c + F_d \tag{2.10}$$

Assuming the vehicle is traversing a flat surface, then:

$$F_c = 0 \tag{2.11}$$

$$F_{\text{env}} = F_f + F_d \tag{2.12}$$

The rolling resistance force F_f and the aerodynamic drag force F_d are given by Equation 2.13 and Equation 2.14:

$$F_f = f \cdot m \cdot g \cdot \cos(\alpha) = \mathrm{RDp}_f \times \mathrm{CHAp}_{m-eq} \times \mathrm{RDp}_g \tag{2.13}$$

$$F_d = 0.5 \cdot C_D \cdot A \cdot \rho \cdot V^2 = 0.5 \cdot (\mathrm{RDp}_{Cx} \times \mathrm{RDp}_A \times \mathrm{RDp}_\rho) \times (V_{\text{ev}})^2 \tag{2.14}$$

Table 2.1 gives detailed information about the Road and Chassis parameters. When we implement the model in Simulink, we will use the above relationships.

As part of the systematic exploration of the traction subsystem within the MATLAB Simulink framework, we start with an examination of the *Road element*. Illustrated in Figure 2.8, this element is modeled with an input variable V_{ev}, indicative of the vehicle speed, and an output

Table 2.1 Road and Chassis Parameters

Parameter	**Value**
`RDp.g`	9.81 m/s^2 (gravity)
`RDp.A`	6.027 m^2 (Frontal Area)
`RDp.Cx`	0.3333 (Drag Coefficient)
`RDp.ro`	1.200 kg/m^3 (Density of the Air)
`RDp.Kaero`	`RDp.ro` × `RDp.Cx` × `RDp.A`/2 (Constant for the resistance force to aero)
`RDp.f`	0.014 (Static Friction Force)
`CHAp.M_eq`	2×10^4 kg (Equivalent mass)

variable F_{env}, which corresponds to the environmental force acting on the vehicle. Adapting the road parameters to align with our specific case study, as presented in Equation 2.12, we establish the road block in Simulink. Figure 2.9 showcases the Simulink model that integrates these custom parameters, effectively simulating the longitudinal dynamics for our vehicle analysis.

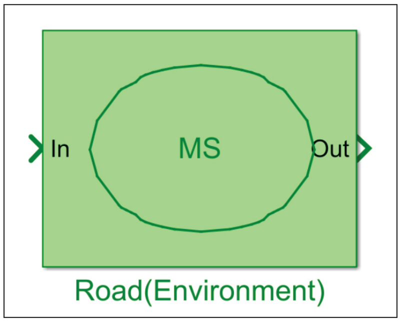

Figure 2.8 Schematic of the Road Element in Simulink

With the *Road element* rigorously established and serving as a foundational block in our Simulink model, we now transition our focus to the *Brake element*.

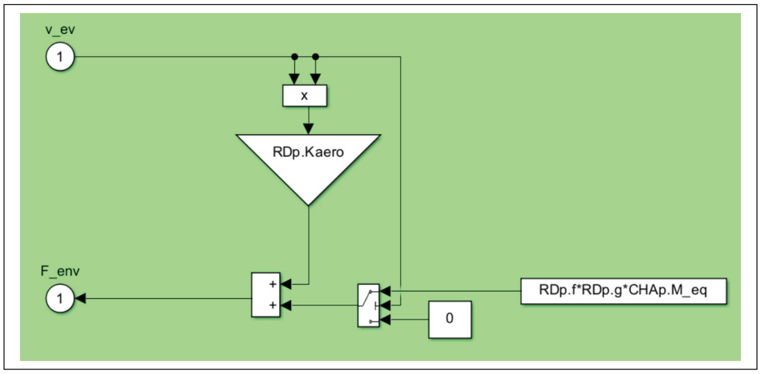

Figure 2.9 Simulink Model for the Road Block

2.4.1.2 Brake Element

Initiating our exploration of the *Brake element*, we explore its crucial role within the vehicle's traction subsystem, providing the necessary resistance to ensure controlled deceleration and safe handling.

In the pursuit of simplicity and clarity within our thesis framework, the design of the brake block is premised on the assumption that the actual braking force aligns with the reference value. Conceptually, the reference braking force is a proxy for the driver's input, corresponding to the pressure applied on the brake pedal, while the actual braking force is what engages with the vehicle's mass. Detailed insights into how this reference braking force is determined for enhanced simulation accuracy will be discussed in Chapter 3. For the current scope, the *Brake element* is mathematically represented by Equation 2.15.

$$F_{\mathrm{br}} = F_{br\_ref} \tag{2.15}$$

The corresponding Simulink block mirrors the structure employed for the Road element, with *reference braking force* F_{br_ref} serving as the input and *actual braking force* F_{br} as the output. The Simulink model expressing this relationship is depicted in Figure 2.10.

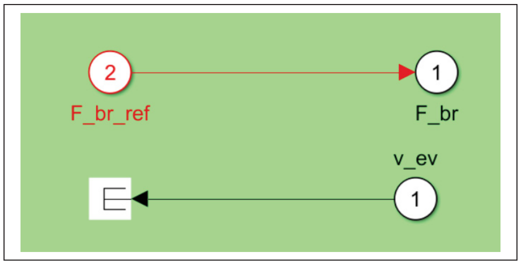

Figure 2.10 Simulink Model for the Brake Element

2.4.1.3 Battery Element

In this part, we start by looking at the battery cell's equivalent circuit model and define its key parameters. Next, we will show how we set up this model in Simulink, explaining each block and how they work together. After modeling, we'll focus on our specific system needs, particularly how many battery cells we need to connect in series and parallel to meet our energy requirements.

First a background knowledge of $LiFePO_4$ battery pack specifications for the propulsion system is required. The propulsion system of our setup is driven by a voltage source inverter, supplied by a $LiFePO_4$ battery pack with 752 V and 50.6 Ah. This high-voltage battery pack is essential to provide the power needed to feed the electric motor efficiently. The detailed specifications of this battery pack, including capacity, energy density and other key features, are summarized in Table 2.2.

Table 2.2 $LiFePO_4$ battery cell specification

Taken from Enix Energies (2014)

Technology	Lithium Iron Phosphate
Nominal Voltage	3.2 V
Standard Capacity	2.3 Ah
Weight	80 g
Max Continuous Discharge Current	46 A
Max / Min Cell Voltage	3.6 V / 2.6 V

Now our focus shifts to enhancing the circuit model by simulating over-voltage conditions. This is achieved by integrating a resistor parallel to a capacitor, illustrated in Figure 1.10. To further refine the model and mirror real-world scenarios more accurately, a capacitor c_{bat} is added in series, designed to stabilize voltage fluctuations. This advanced circuit model is thoroughly depicted in Figure 2.11.

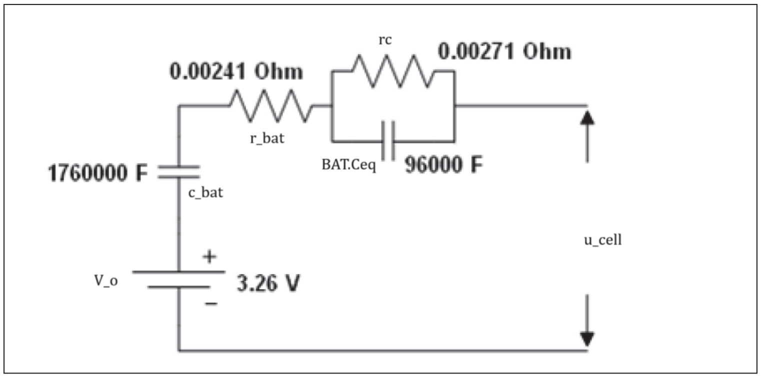

Figure 2.11 Equivalent Circuit for System Battery Cell

Taken from Mantravadi, Husain & Sozer (2011)

By examining the battery's voltage during charging and discharging cycles, it is observed that the open circuit voltage V_{oc} is best estimated by averaging the voltages at 10% SOC from both charging and discharging curves. This observation indicates that if the battery voltage linearly shifts from 0.95 V_{nom} to 1.05 V_{nom}, the SOC will correspondingly adjust from 20% to 90%. This relationship is mathematically represented in Equation 2.16.

$$\begin{cases} \Delta V_{\text{nom}} = \frac{1.05 \cdot V_{\text{nom}} - 0.95 \cdot V_{\text{nom}}}{V_{\text{nom}}} \quad \Delta V_{\text{nom}} = 10\% \\ \text{and} \quad V_{nom} = 3.2 \end{cases} \tag{2.16}$$

To compute the SOC, our model establishes an initial SOC at 70%. Additionally, a momentary SOC is derived as shown in Equation 2.17. The overall SOC is then determined according to the methodology outlined in Equation 2.18.

$$SOC_{Momentary} = (\int_0^t I_{cell}(t) d_t) \times (\frac{1}{3600}) \times (\frac{1}{BAT.Q_{bat}}) \tag{2.17}$$

In this Equation 2.17, $BAT.Q_{bat}$ represents the battery cell capacity in (Ah).

$$SOC_{total} = SOC_{Momentary} - SOC_0 \tag{2.18}$$

The cell's storage capacitance c_{bat} is estimated by determining the gradient of the average voltage curves during both charge and discharge from 20% to 100% SOC Mantravadi *et al.* (2011).

The battery cell's ohmic resistance, represented as r_{bat}, is calculable by observing the immediate voltage change upon opening *open circuit* or closing *close circuit* the test circuit. This instantaneous voltage shift, when divided by the constant current value used in the discharge test, provides the measure for the cell's internal resistance Mantravadi *et al.* (2011).

The cell's diffusivity resistance, denoted as rc, is established by examining the voltage increase from the moment just after the battery's voltage begins to rise until it stabilizes during a rest period. This voltage variation, once divided by the steady current employed during the discharge testing, yields the diffusivity resistance value Mantravadi *et al.* (2011).

Diffusivity capacitance, represented as $BAT.C_{\text{eq}}$, is calculated based on the time it takes for the battery voltage to stabilize after the closure of the test circuit. This time constant, when divided by the previously determined diffusivity resistance, provides the measurement for diffusivity capacitance Mantravadi *et al.* (2011).

All the parameters incorporated within the battery model, as exhibited in Figure 2.11, are comprehensively enumerated in Table 2.3.

Table 2.3 Battery Model Parameters

Parameters	**Values**
V_0	3.2 (V)
C_{bat}	1.76×10^6 (F)
r_{bat}	0.00241 (ohm)
rc	0.00271 (ohm)
BAT.C_{eq}	9.6×10^4 (F)

In the subsequent phase of our analysis, we proceed to compute the voltage of an individual battery cell, designated as u_{cell}. The computation is guided by Equation 2.19, which integrates the various parameters and variables of the cell to calculate its voltage.

$$u_{\text{cell}} = V_o - \left[i_{\text{cell}} \times Z_{\text{series}} + i_{\text{cell}} \times Z_{\text{parallel}}\right] \tag{2.19}$$

In this equation, u_{cell} represents the voltage across the battery cell, V_o is the open circuit voltage, i_{cell} is the battery cell current, Z_{series} is the series impedance, and Z_{parallel} is the parallel impedance. The series impedance consists of resistive and inductive elements in series with the battery cell, whereas the parallel impedance accounts for the shunt resistance and capacitance across the cell. In the context of the battery model, Equation 2.21 delineates the constituents of both Z_{series} and Z_{parallel}:

$$Z_{series} = r_{bat} + \frac{1}{c_{bat}.S} \Rightarrow Z_{series} = \frac{(r_{bat}.c_{bat}.S) + 1}{c_{bat}.S} \tag{2.20}$$

$$Z_{parallel} = \frac{rc \times \frac{1}{BAT.C_{eq} \times S}}{rc + \frac{1}{BAT.C_{eq} \times S}} \Rightarrow Z_{parallel} = \frac{rc}{(rc \times BAT.C_{eq} \times S) + 1} \tag{2.21}$$

To proceed with our analysis, we have identified all the variables required to calculate the battery cell voltage, u_{cell}. Next, we will integrate this computation into our Simulink model, which is shown in Figure 2.12.

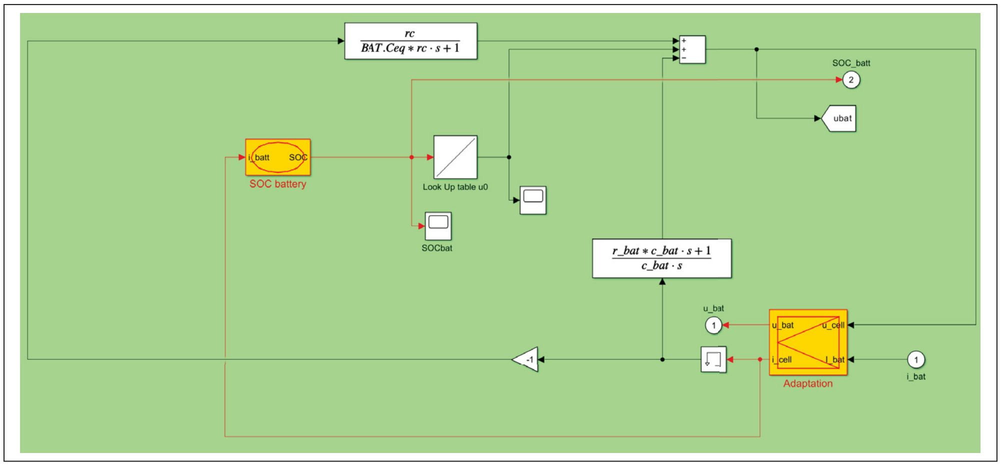

Figure 2.12 Simulink Model Illustrating Battery Cell Voltage Calculation

The Adaptation block in the figure is designed to ascertain the requisite number of cells arranged in series and parallel to meet the specifications of our ESS. simultaneously, the SOC block governs the SOC_{total}.

2.4.1.4 Electric Drive

Electric Motors serve as multi-physical energy converter elements in automotive applications and function as electromechanical energy transformers, converting electrical energy into mechanical energy. These typically include synchronous and induction machines. Figure 2.13 illustrates the multi-physical conversion element as per EMR framework.

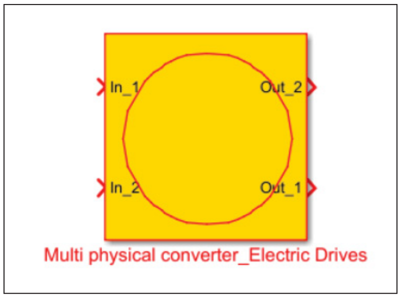

Figure 2.13 Schematic of the Electric Drives in Simulink

In HEVs, EMs respond quicker than ICEs due to their superior availability and performance. However, managing and controlling EMs' energy efficiently presents challenges. To address these, various modeling approaches like dynamic, static, and quasi-static are employed, each with its own set of pros and cons Syed (2012). In this context, we utilize static modeling to create an EM performance map. This method is chosen for its shorter simulation times and its simplicity in analyzing power and energy in steady-state conditions, which aids in overall optimization efforts.

In static modeling, time constants are not considered, allowing for a comprehensive representation of the EM, including its inverter and control systems. Additionally, the EMs are regulated directly through a specified reference torque, as demonstrated in Equation 2.22 Syed (2012).

$$T_{\mathrm{ed}} = T_{\mathrm{ed\_ref}} \tag{2.22}$$

In static modeling, we assume that control accuracy is flawless, resulting in the output torque T_{ed} precisely matching the reference torque $T_{\mathrm{ed\_ref}}$.

In our static model, the electric drives are described by a basic equation as seen in Equation 2.23. This equation also takes into account that there are always some energy losses in the system's components.

$$i_{ts} = \frac{T_{ed}\omega_{gb}\eta_{ed}^{K_{ed}}}{u_{bat}} \tag{2.23}$$

$$\text{where } K_{ed} = \begin{cases} -1 & \text{if } T_{ed}\omega_{ed} \geq 0 \\ 1 & \text{if } T_{ed}\omega_{ed} < 0 \end{cases}$$

In the given formula, T_{ed} represents the electric drive's torque measured in Newton-meters (Nm), and ω_{ed} signifies the angular velocity facilitated through the gearbox, measured in radians per second (rad/s). To discover the efficiency, we introduce K_{ed}, which adjusts based on the energy flow direction. Energy either flows from the energy sources to the environment during acceleration or from the environment back to the vehicle during regenerative braking. Thus, efficiency is applied according to the energy transfer direction: the first scenario applies to outward energy flow, while the second corresponds to inward energy recuperation.

Figure 2.14 illustrates the implementation of this model within Simulink.

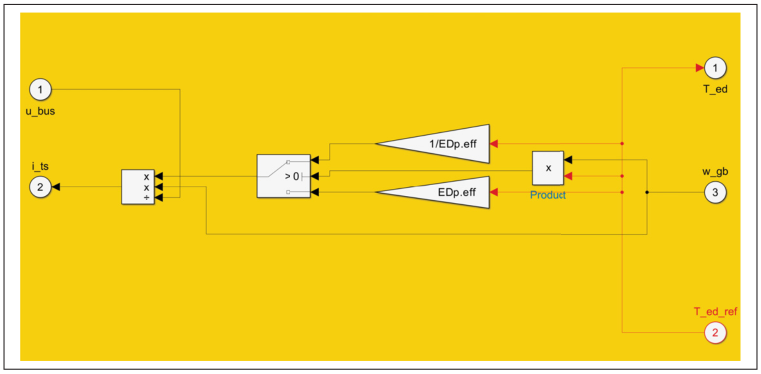

Figure 2.14 Implementation of the Electric Drive Model in Simulink

In our model $ED_p.eff$ represents the EM efficiency and it is assumed as high as 90%.

2.4.1.5 Gearbox

The *Gearbox* serves to align the engine's output torque with the demand at the wheels, referred to as the load torque. This demand is shaped by several factors, including the vehicle's mass, the desired acceleration rate, incline gradients, aerodynamic drag, and the rolling resistance encountered. Consequently, the gearbox must possess the capability to manage a torque output exceeding the usual requirement at the wheels Syed (2012). Within the EMR depiction, the gearbox is illustrated as a monophysical energy conversion element in Figure 2.15, signifying its role in modifying mechanical power into altered mechanical power outputs. This is characterized by a constant conversion ratio, denoted as K_g, and a transformation ratio, represented as K_{gb}. The mathematical representation of the gearbox is provided in Equation 2.24 and Equation 2.25.

$$T_{gb} = T_{ed} \times K_{gb} \times \eta_{gb}^{K_g} \tag{2.24}$$

$$\text{where} \quad K_g = \begin{cases} -1 & \text{if } T_{ed}\omega_{gb} < 0 \\ 1 & \text{if } T_{ed}\omega_{ed} \geq 0 \end{cases}$$

$$\omega_{gb} = \omega_{wh} \times K_{gb} \tag{2.25}$$

In Equation 2.25, ω_{wh} represents the input rotational velocity coming from wheels.

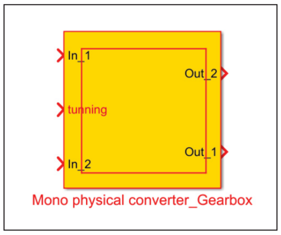

Figure 2.15 Schematic of the Gearbox in Simulink

Table 2.4 shows the values and specifications for our gearbox parameters, where MTp.Gear_eff is represented as η_{gb} and MTp.K_gear is represented as K_{gb}.

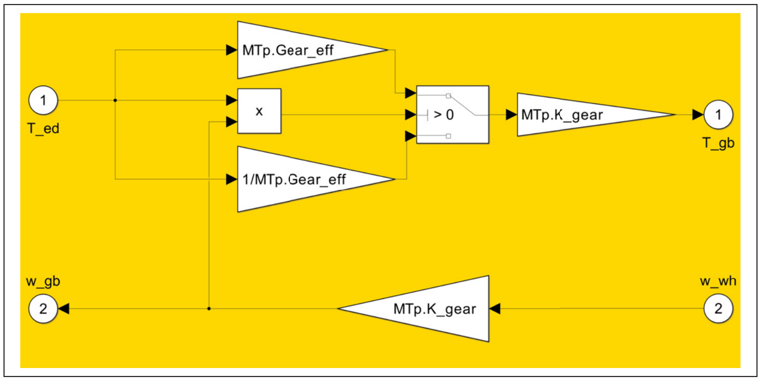

Figure 2.16 Implementation of the Gearbox Model in Simulink

Table 2.4 Gearbox Parameters

Parameter	Value
MTp.Gear_eff	0.95
MTp.K_gear	3.73

2.4.1.6 Wheels

The *Wheels* block in our system is characterized as a monophysical energy conversion element, the same as the gearbox element depicted in Figure 2.15. This block serves as an essential link between the road and the vehicle's chassis, transforming the gearbox's differential rotation into linear motion propelling the vehicle. Assuming a straight roadway without slippage, the model simplifies this interaction to a single equivalent wheel. The mathematical relationship, demonstrating how the gearbox torque is converted to wheel force by dividing it by the wheel radius, is represented in Equation 2.26 Syed (2012):

$$F_{wh} = \frac{T_{gb}}{R_{wh}} \tag{2.26}$$

This equation details the direct relationship between the gearbox torque T_{gb} and the force exerted by the wheels F_{wh}, with the wheel radius R_{wh} serving as the conversion factor.

Another output of the wheels block is the rotational speed of the wheel, which is calculated by dividing the vehicle's velocity by the wheel radius, as demonstrated in Equation 2.27:

$$\omega_{wh} = \frac{v_{ev}}{R_{wh}} \tag{2.27}$$

Having established the mathematical model for the equivalent wheel, we proceed to implement this model in Simulink. Figure 2.17 illustrates the representation of the equivalent wheels within the EMR framework.

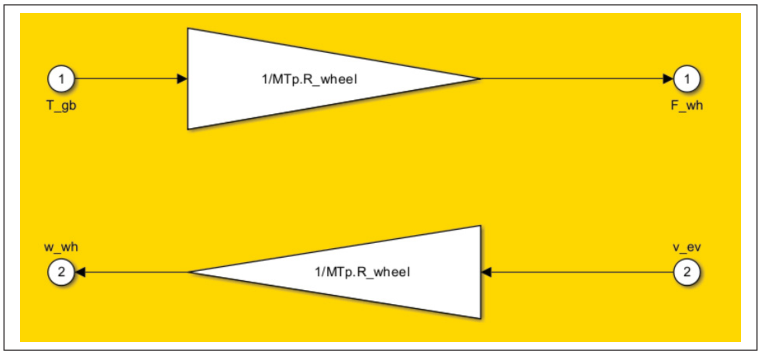

Figure 2.17 Implementation of the Wheels Model in Simulink

Table 2.5 shows the wheel parameters, where MTp.D_wheel represents the wheel diameter and MTp.R_wheel represents the wheel radius.

Table 2.5 Wheel Parameters

Parameter	Value
MTp.D_wheel	1.0922 m
MTp.R_wheel	0.5461 m

2.4.1.7 Chassis

Analyzing the chassis involves separating it into two segments, the initial segment being depicted through a monophysical coupling element as illustrated in Figure 2.18. This segment's purpose is to compute the total force applied to the vehicle's mass, incorporating the mechanical braking force alongside the powertrain's force, represented as F_{wh}. The incorporation of the mechanical braking force, denoted as F_{br}, with F_{wh} is facilitated by the coupling element, allowing for an augmented variable representing the total force from the powertrain. Equation 2.28 describes the coupling element's mathematical model.

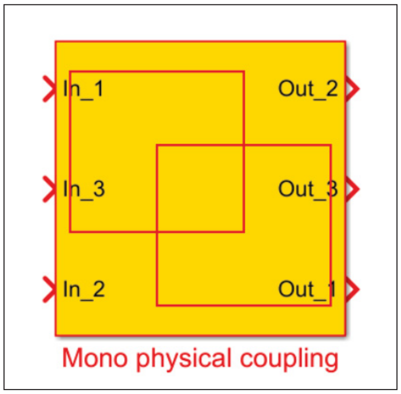

Figure 2.18 Schematic of the Monophysical Coupling in Simulink

$$F_{trac} = F_{wh} + F_{br} \tag{2.28}$$

Figure 2.19 depicts the model of the coupling element within the EMR framework.

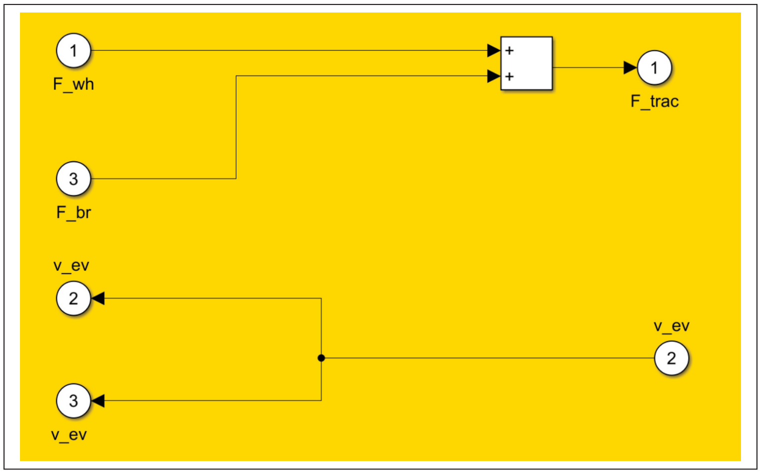

Figure 2.19 Implementation of the Monophysical Coupling Model in Simulink

The second segment of the chassis analysis is illustrated using an accumulation element, as demonstrated in Figure 2.20. Consistent with earlier discussions, the presence of a derivative in our mathematical modeling necessitates the involvement of an accumulation element within the EMR framework. Specifically, for the chassis, our mathematical formulation, depicted in Equation 2.29, includes a derivative to determine the force applied on the vehicle by external environmental factors Mantravadi *et al.* (2011).

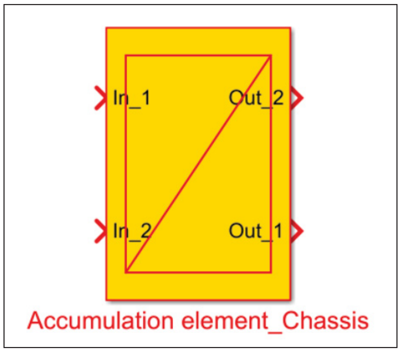

Figure 2.20 Schematic of the Accumulation Element in Simulink

$$V_{\text{ev}}(t) = \frac{1}{M_{\text{tot}}} \int (F_{\text{trac}}(t) - F_{\text{env}}(t))\, dt \tag{2.29}$$

Figure 2.21 illustrates the mathematical model within the EMR framework.

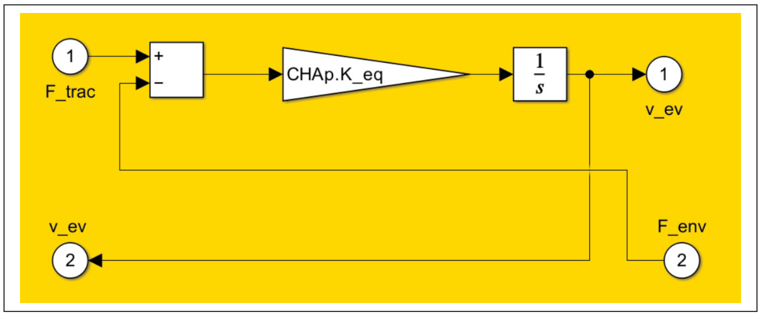

Figure 2.21 Implementation of the Chassis Accumulation Model in Simulink

Table 2.6 shows the chassis parameters, where CHAp.M_eq represents the equivalent mass (including the shaft and chassis) and CHAp.K_eq represents the velocity gain.

Table 2.6 Chassis Parameters

Parameter	Value
CHAp.M_eq	2×10^4 kg
CHAp.K_eq	5×10^{-5}

2.4.2 The IBC layer

In EMR, the initial step involves carefully examining the system's control paths. By pinpointing these pathways, we can build a control approach that effectively inverts the system's behavior, allowing for precise adjustments in response to changing conditions.

As seen earlier, the tuning path for our traction subsystem, depicted in Figure 2.3, aligns with our system's objectives. Following this, we establish the control paths by inversely mapping the tuning paths. Because by inverting the tuning paths, the corresponding control paths can be established. The primary goal is to adhere to a specified speed profile, specifically the normalized NEDC driving cycle in this study. Achievement of this goal is marked by the vehicle's actual speed closely mirroring the reference speed set by the driving cycle. Therefore, in our case, the target *objective* variable is v_{ev}, and the *control* variables are $T_{\mathrm{ed\_ref}}$ and $F_{\mathrm{br\_ref}}$. This setup indicates that the entire system is regulated through $T_{\text{ed\_ref}}$ and $F_{\text{br\_ref}}$. By navigating through the IBC blocks, our aim is to align the vehicle's speed with the reference speed, initiating the process of evaluating all parameters along our tuning path. This approach involves setting reference parameters for each block in the modeling layer of EMR and methodically incorporating them in reverse order through the IBC blocks to define our control path.

In the EMR framework, energy sources serve as the system's terminals and are not subject to inversion. The control path for our traction subsystem begins with the inversion of the chassis accumulation element within the IBC, followed by the chassis coupling element. Subsequently, we invert the models for the equivalent wheel, gearbox, and electric drive. This step-by-step inversion process, originating from the reference speed and concluding at the electric drive torque, enables us to regulate the vehicle's speed.

Additionally, direct inversion applies exclusively to mono or multi-physical converters, thanks to their non-temporal nature and typically linear, unchanging relationships. Accumulation elements, however, resist direct inversion due to their reliance on time-dependent relationships, which inherently resist physical inversion. Consequently, this necessitates the implementation of a closed-loop control strategy to address this limitation Syed (2012). In our case, this controller is a PI controller.

2.4.2.1 Inversion of Chassis Accumulation

The schematic representation of inverting an accumulation element through a PI controller is detailed in Figure 2.6, with its operational mechanics explained by Equation 2.2. Therefore, the mathematical model employed within our IBC accumulation element is as follows:

$$F_{\text{tot}_{\text{ref}}}(t) = F_{\text{meas}}(t) + C_{\text{corr}}[v_{\text{ev}_{\text{ref}}}(t) - v_{\text{ev}_{\text{meas}}}(t)] \tag{2.30}$$

As illustrated, the inverted accumulation block, utilizing measurements from the EMR, translates the reference speed (desired speed) into the required total force. This process essentially determines the total force needed to achieve a given desired speed. With both the measurements and reference at hand, we can complete the control loop. This controller puts measured values against our desired (reference) values to reduce error by adjusting control inputs. Once the error is minimized, the reference for the total force needed to secure the desired speed is established, continuing the inversion path until we reach our control variable, T_{ed-ref}. This variable directly influences the EMR, effectively closing the loop. The expectation is that the measured vehicle speed aligns with the reference speed. We now aim to delve deeper into the critical aspect of this process, the inversion of the accumulation element.

This implies that the accumulation inversion element acts as a controller within our system, specifically a PI controller in this context.

For the design of our control unit, a more thorough analysis of the PI controller's block diagram is necessary. Initially presented in Figure 1.15 and analyzed within the time domain, we shall now re-evaluate the diagram through a new lens, applying the Laplace transform to Equation 1.4 to deepen our understanding of its operational dynamics. The Laplace transform of Equation 1.4 yields the transfer function of a PI controller, which is represented as Equation 2.31.

$$u(t) = K_p e(t) + K_i \int e(t)\, dt \xrightarrow[Laplace]{} \rightarrow K_p + K_i/s \tag{2.31}$$

The *Plant* block, which was previously shown in Figure 1.15, will now represent the longitudinal dynamics of the FCEV in the revised control system architecture. As a result, the Plant block is redesigned in the Laplace domain using the transfer function, as seen in Equation 2.32.

$$V_{ev}(t) = \frac{1}{M_{tot}} \int F_{tot}(t) d_t \xrightarrow[Laplace]{} K_{ch}/s \tag{2.32}$$

The updated configuration of the PI controller within our system, reflecting the integration of the FCEV's longitudinal dynamics in the Laplace domain, is visualized in Figure 2.22.

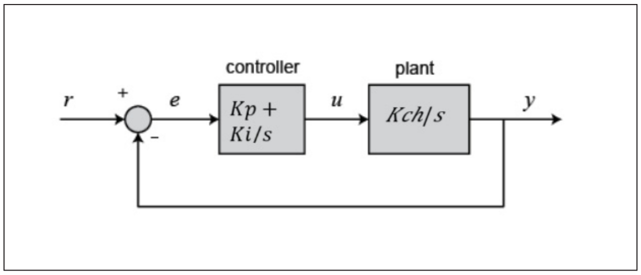

Figure 2.22 PI Controller in Laplace domain

Based on the PI controller's block diagram in the Laplace domain, the transfer function linking the input to the output is represented by Equation 2.33:

$$\begin{aligned} (y - r) \times (K_p + K_i/S) \times (K_{ch}/S) &= y \\ r \times (K_p + K_i/S) \times (K_{ch}/S) &= y \times (1 + (K_P + K_i/S) \times (K_{ch}/S)) \\ r \times \frac{(K_p \times S \times K_i) \times K_{ch}}{S^2} &= y \times \frac{S^2 + K_p S K_{ch} + K_i K_{ch}}{S^2} \\ \rightarrow \frac{y}{r} &= \frac{K_p K_{ch} S + K_i K_{ch}}{S^2 + K_p K_{ch} S + K_i K_{ch}} \end{aligned} \tag{2.33}$$

The formulation in Equation 2.33 indicates the presence of a second-order system.

We also examined the block diagram of the PI controller within the Laplace domain as shown in Figure 2.22. The relationship between the input and output is defined by the transfer function presented in the subsequent equation:

$$\frac{y}{r} = \frac{K_p K_{ch} S + K_i K_{ch}}{S^2 + K_p K_{ch} S + K_i} \tag{2.34}$$

we concluded that this represents a second-order system as illustrated in Equation 2.35 Ogata (1999):

$$H(S) = \frac{\omega_n^2}{S^2 + 2\zeta\omega_n S + \omega_n^2} \tag{2.35}$$

By incorporating the values from our PI controller into the second-order system equations, we obtain the following relationships:

$$\omega_n^2 = K_{chas} \times K_i \quad \text{leading to} \quad K_i = \frac{\omega_n^2}{K_{chas}},$$

and subsequently,

$$2\zeta\omega_n = K_{chas}K_p \quad \text{yielding} \quad K_p = \frac{2\zeta\omega_n}{K_{chas}}.$$

Having understood the PI controller used in the inversion of the accumulation element, we proceed to construct the Simulink model. This model is grounded on the mathematical framework of the PI controller, as showcased in Figure 2.23.

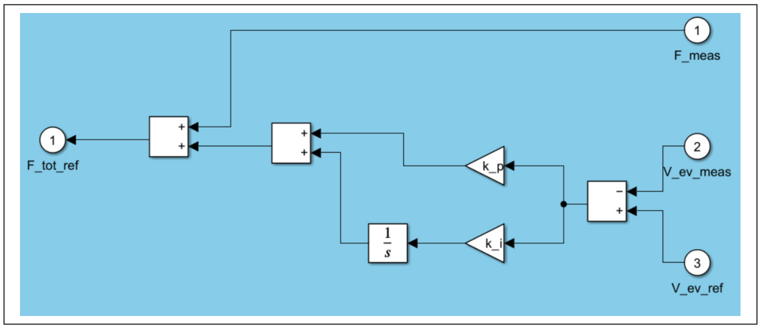

Figure 2.23 Implementation of the Chassis Accumulation Inversion Model in Simulink

For the PI speed controller, we assumed that the controller's natural frequency ω_n and the damping factor ζ are $\frac{3}{t_r}$ and 0.7, respectively, where t_r is the rise time. The constants K_i and K_p can be calculated as follows:

$$K_i = \frac{\omega_n^2}{CHAp.K_{eq}}$$

$$K_p = \frac{2 \cdot \xi \cdot \omega_n^2}{CHAp.K_{eq}}$$

Given the assumptions:

$$t_r = 1$$

$$\xi = 0.7$$

$$\omega_n = \frac{3}{t_r} = 3$$

$$CHAp.K_{eq} = \frac{1}{2 \times 10^4} = 5 \times 10^{-5}$$

Thus, we can calculate K_i and K_p as:

$$K_i = \frac{3^2}{5 \times 10^{-5}} = \frac{9}{5 \times 10^{-5}} = 1.8 \times 10^5$$

$$K_p = \frac{2 \cdot 0.7 \cdot 3^2}{5 \times 10^{-5}} = \frac{2 \cdot 0.7 \cdot 9}{5 \times 10^{-5}} = \frac{12.6}{5 \times 10^{-5}} = 2.52 \times 10^5$$

2.4.2.2 Inversion of Chassis Coupling

The inversion of the chassis coupling element is represented by what is termed as the distribution block inversion, as depicted in Figure 2.24.

To understand the operation of the coupling element's inversion block, let's revisit its mathematical foundation as outlined in our modeling layer. According to Equation 2.28, we initially had two

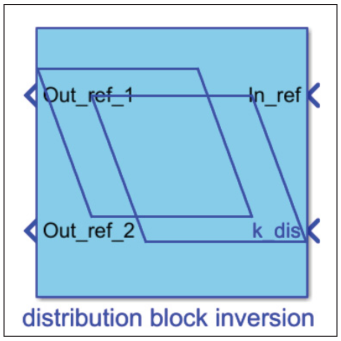

Figure 2.24 Schematic of the Distribution Block Inversion in Simulink

inputs: F_w and F_{br}. Upon inversion, these become two outputs: F_{br_ref} and F_{w_ref}, with a singular input, F_{tot_ref}, from the inversion of the accumulation block. This stage necessitates determining the allocation between the outputs. A distribution coefficient, K_{br}, is introduced to specify the portion of the total reference force allocated to regenerative braking (which, in turn, contributes to the electric drive) versus mechanical braking. The mathematical expressions below detail the inversion of the coupling element:

$$F_{w\_ref} = (1 - K_{br}) \cdot F_{tot\_ref} \tag{2.36}$$

$$F_{br\_ref} = K_{br} \cdot F_{tot\_ref} \tag{2.37}$$

Implementing this mathematical framework in Simulink results in the creation of the distribution inversion block for chassis coupling, as depicted in Figure 2.25. The methodology for determining K_{br} will be thoroughly elaborated in the subsequent sections of this chapter, specifically within the Strategy layer discussion.

2.4.2.3 Inversion of Equivalent Wheel & Gearbox

The inversion processes for both the Equivalent Wheel and the Gearbox blocks are facilitated using the Converter Inversion Block, as illustrated in Figure 2.26.

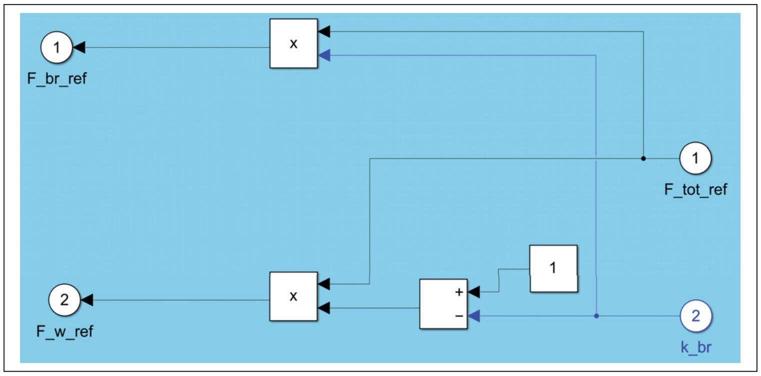

Figure 2.25 Implementation of the Chassis Coupling Inversion Model in Simulink

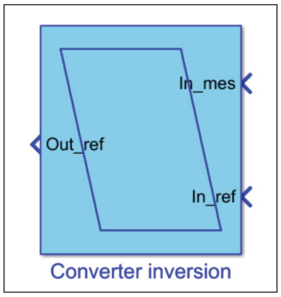

Figure 2.26 Schematic of the Converter Inversion in Simulink

The Equivalent Wheel and Gearbox are directly inverted, representing the most straightforward mathematical modeling within the IBC framework. The mathematical models for the inversion of these components are detailed in Equation 2.38 and Equation 2.39.

$$T_{gb\_ref} = R_{wh} \cdot F_{w\_ref} \tag{2.38}$$

$$T_{ed\_ref} = \frac{T_{gb\_ref}}{K_{gb}} \tag{2.39}$$

Figures 2.27 and 2.28 illustrate the implementation of these mathematical models in Simulink.

MTp.R_wheel and MTp.K_gear are listed in Table 2.5 and Table 2.4, respectively.

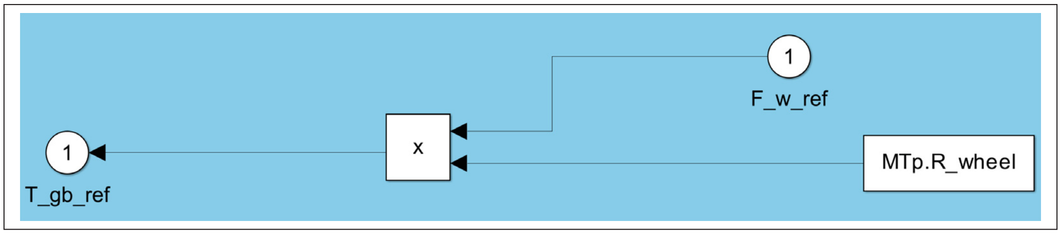

Figure 2.27 Implementation of the Equivalent Wheel Inversion Model in Simulink

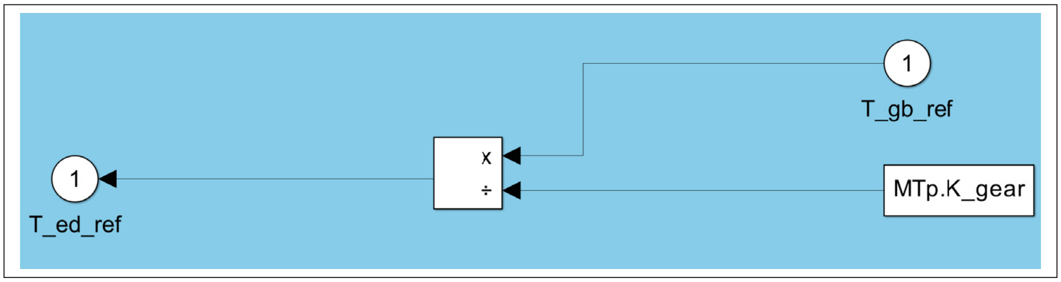

Figure 2.28 Implementation of the Gearbox Inversion Model in Simulink

2.4.3 The strategy layer

The EMR-based control framework establishes a local control level, while the strategy level serves as the global energy management system. To clarify, the in-depth control methodologies, including IBC, are part of the localized control structure, as outlined earlier. On the other hand, the strategy level includes global energy management, guiding the overall energy consumption across the system to formulate a control mechanism for complex systems Keyu (2010). The strategy block, shown in Figure 2.29, focuses on braking strategies within the traction subsystem. This is where we determine the distribution coefficient, K_{br}, to allocate energy between mechanical braking and regenerative braking.

To develop the braking strategy, we focus on the management of regenerative braking. Our system distinguishes between mechanical and electric *regenerative braking*. The strategy block determines the energy distribution between these two forms. The approach is outlined as follows:

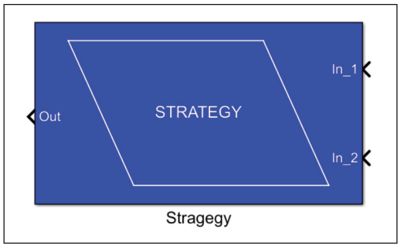

Figure 2.29 Schematic of the Strategy Block in Simulink

initially, we assess whether the reference total force indicates braking. If so, we examine the battery's permissible charge current to ensure it's not exceeded. Based on these conditions, rules are established to allocate energy between mechanical braking and regenerative braking. We assign the distribution coefficient, K_{br}, a value of 0.5, representing a scenario where energy loss is maximized. This simplification assumes that only half of the potential regenerative energy is recoverable, influenced by the efficiency of powertrain components. Figure 2.30 illustrates the sequence and conditions involved in managing regenerative braking within our system. It visualizes the process of determining whether braking is required, assessing the battery's charge limit, and then applying rules to distribute energy between mechanical and regenerative braking. Specifically, it depicts how the value of K_{br} is set to 0.5 to represent a balanced approach to energy recovery, taking into account the efficiency of powertrain components and the worst-case scenario for energy loss.

Considering the model's battery has a maximum charge current of 690 A, applying the decision process from Figure 2.30 into the strategy block in Simulink results in the setup shown in Figure 2.31.

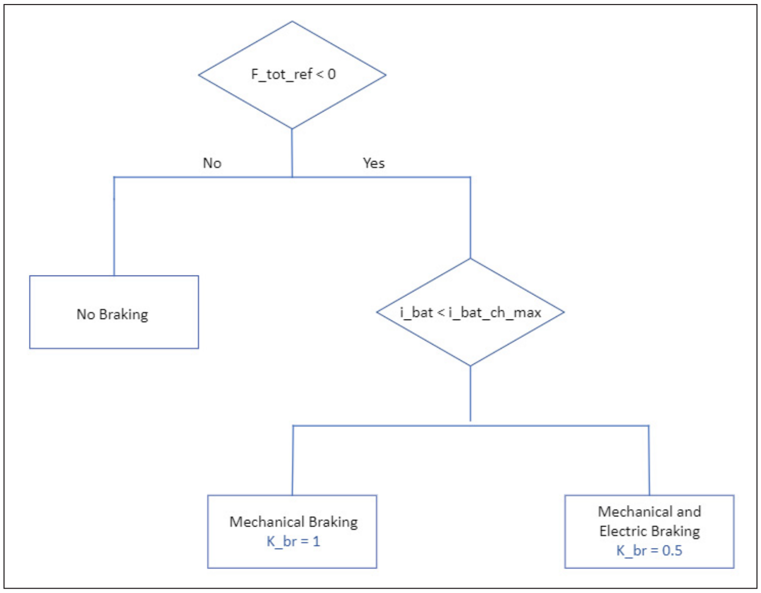

Figure 2.30 Decision process for distributing braking energy

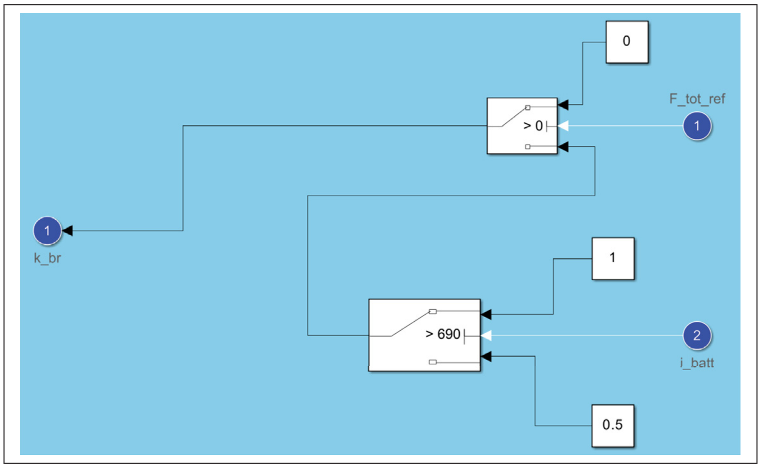

Figure 2.31 Implementation of the Braking Strategy Model in Simulink

2.5 Energy Storage Subsystem: Modeling Procedure and Analysis

This section delves into the ESS of our FCEV model. Adopting a similar approach as with the Traction Subsystem, the analysis and development of the ESS are structured into three methodical phases. Initially, we construct the modeling layer, detailing the ESS components and their interactions. Subsequently, the focus shifts to the local control aspect, where IBC blocks are applied. Lastly, we outline the strategy layer, which, for the ESS, incorporates a specialized EMS employing Fuzzy Logic. This novel EMS design, pivotal for the ESS's efficient operation, will be expounded upon in Chapter 3.

2.5.1 The modeling layer

In the context of the ESS, the modeling layer is investigated to comprehend the system's complexity and boundaries. Unlike the TS, the ESS's boundary is defined solely by the PEMFC. The modeling layer further includes the inductor and boost chopper, essential components for voltage regulation and power flow control. The PEMFC is orchestrated in parallel with the battery storage through a parallel connection coupling, ensuring an integrated operation. This setup forms the cornerstone of our ESS modeling layer, facilitating a detailed simulation of energy management within the FCEV.

2.5.1.1 The Fuel Cell Element

The PEMFC is a sophisticated electrochemical system, incorporating components crafted from composite, porous, and nano-materials to optimize electrochemical efficiency. Within the PEMFC, numerous complex interactions occur, including electrochemical reactions, electron and proton transfer, and the transport of reactants, water, vapor, and heat. These processes often span multiple boundaries and involve multiphase flows, with electrode reactions occurring at multiphase interfaces. Characterizing these interactions and materials poses challenges due to their simultaneous occurrence across varied spatial dimensions. Additionally, three-dimensional analysis becomes crucial for assessing the performance and durability of fuel cell stacks, which are highly sensitive to localized conditions. The extreme operational conditions of high potentials, temperatures, pressures, gas flows, and humidification levels further complicate measurements in situ. Electrode processes are key to the performance and durability of fuel cells, leading to the adoption of electrochemical techniques such as polarization curves, cyclic voltammetry (CV), linear sweep voltammetry (LSV), CO stripping voltammetry, and electrochemical impedance spectroscopy (EIS) for their characterization Valle (2014). In our research, we utilized the fuel cell polarization curve to develop a Simulink model of our fuel cell. In Chapter 1, we highlighted the polarization curve as a critical tool for evaluating fuel cells, detailing the correlation between cell voltage and current density. Figure 1.9 illustrates the polarization curve for a PEMFC, clearly describing the activation, ohmic, and mass transport regions. The PEMFC stack utilized in this research is derived from the IEEE VTS Motor Vehicle Challenge 2020. This particular stack was developed by HELION in Aix-en-Provence, France, as part of the SPACT-80 project. The project's goal was to create fuel cell systems (FCS) that are optimized for high-power transportation applications Solano *et al.* (2019). Table 2.7 summarizes the HELION PEMFC specification.

Table 2.7 Specifications of the HELION Fuel Cell Stack

Description	Value
Supplier	HELION (Areva)
Elements in series	2×110
Maximal gross power	80 [kW]
Maximal voltage	190 [V]
Power rate change	5 [A/s]

We modeled the fuel cell element in Simulink by employing the polarization curve, taking into account the values specified in Table 2.7. The Simulink representation of the fuel cell element is depicted in Figure 2.32.

To explain the Simulink model of the fuel cell, we begin by examining the polarization function, which characteristically follows a cubic polynomial of the form $ax^3 + bx^2 + cx + d$. This expression serves as a foundation to depict the voltage-current relationship for the fuel cell within our simulation environment. This mathematical model, by its cubic nature, could erroneously allow for negative values. However, negative current values have no physical meaning in the context of fuel cell operations. To rectify this within our Simulink model, a diode is implemented ahead of the i_{fc} input to the polarization curve block. This ensures that only positive current values, which are physically feasible, are permitted, thereby filtering out any unphysical negative

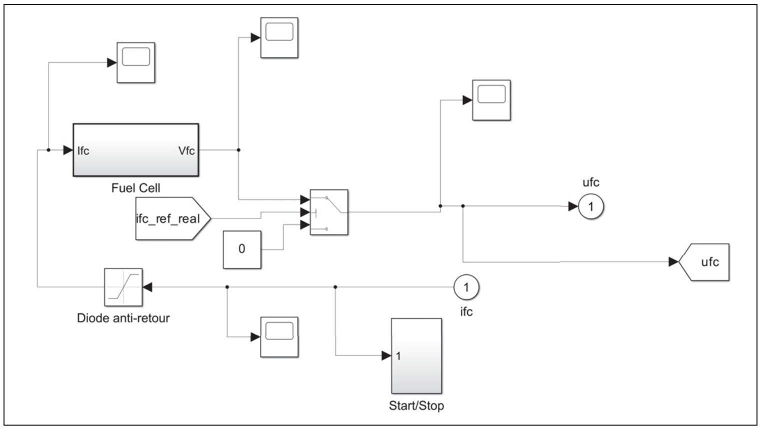

Figure 2.32 Implementation of the Fuel Cell Element in Simulink

currents. The implemented mathematical model in the fuel cell block within Simulink takes the current i_{fc} as its input and provides the fuel cell voltage v_{fc} as the output. The functional relationship for our specific fuel cell is defined by the polynomial:

$$v_{\mathrm{fc}} = -3.5259 \times 10^{-7} \cdot i_{\mathrm{fc}}^3 + 0.00034 \cdot i_{\mathrm{fc}}^2 - 0.3553 \cdot i_{\mathrm{fc}} + 178.7405 \tag{2.40}$$

where i_{fc} represents the current flowing through the fuel cell.

As described by Equation 2.40, the fuel cell model predicts a voltage output of approximately 178 V even when the input current, i_{fc}, is zero. This condition implies that the fuel cell would produce voltage without being actively engaged, which is not the desired behavior in a practical scenario. To address this, a switch is integrated into the Simulink model of the fuel cell block. This switch ensures that the fuel cell outputs zero voltage when it is supposed to be off, particularly when $i_{\mathrm{fc\_ref\_real}}$ is set to a value close to zero (0.001), indicating no current flow. This setup mimics the fuel cell's inactive state more accurately.

Essentially, the switch incorporated into the fuel cell model in Simulink acts as a gatekeeper, determining the operational state of the fuel cell based on the real reference current, $i_{\mathrm{fc\_ref\_real}}$. When $i_{\mathrm{fc\_ref\_real}}$ is greater than or equal to 0.001, the switch allows the voltage output from the fuel cell, v_{fc}, to be supplied to the system. If $i_{\text{fc\_ref\_real}}$ falls below this threshold, the switch ensures that the output voltage is held at a constant value of 0, effectively simulating the fuel cell's disengagement from the system. This mechanism provides precise control over the fuel cell's contribution to the system's energy supply.

The determination of $i_{\text{fc\_ref\_real}}$ and its implementation in controlling the fuel cell's operation will be elaborated upon in the IBC layer discussion of the ESS in subsequent sections.

2.5.1.2 The Smooth Inductor & Chopper Element

In the configuration of the FC system, the primary components are identified as the FC stack, a smoothing inductor, and a boost chopper to control its current. Auxiliary systems such as cooling and air supply are not included in this examination Depature *et al.* (2016).

Positioned at the forefront of the FC element, the smoothing inductor plays a crucial role. Despite sharing the same EMR pictogram as seen in Figure 2.20, its function within the system is distinct. In an FCEV, a smoothing inductor, also known as a filter inductor, is an electrical component used in the power electronics system to reduce voltage ripple and current fluctuations from the fuel cell stack before the power is delivered to the motor or stored in the ESS. This is crucial for maintaining the stability and efficiency of the fuel cell and prolonging the life of both the fuel cell and the electric drive components Dezhou Sanhe Electric Co. (Jul-09-2023).

Figure 2.33 displays the equivalent electrical circuit for both the inductor and the DC/DC converter present in our ESS. In our setup, the DC/DC converter functions as a boost chopper, which means its main role is to adjust the output voltage to meet the specific needs of the load. We can regulate the output voltage by altering the duty cycle of the boost DC-DC converter Samosir, Sutikno & Yatim (2011). This section will first explore the inductor's role and subsequently delve into the workings of the DC/DC converter.

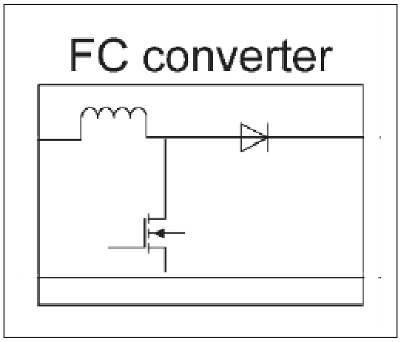

Figure 2.33 Fuell Cell Converter Equivalent Electrical Circuit Model

Taken from Chen & Guan (2021)

To enhance the inductor's model for greater accuracy and simplify the electrical circuit diagram, similar to the illustration in Figure 2.34, we can apply Faraday's law to the inductor. This application is detailed in Equation 2.41 AspenCore,Inc. (Accessed 2023).

The voltage across the inductor V_L is defined by the rate of change of the current through it, mathematically represented as:

$$V_L = L\frac{di}{dt} \tag{2.41}$$

where L represents the inductance of the coil, measured in henries (H), and $\frac{di}{dt}$ is the rate of change of current, expressed in amperes per second (A/s).

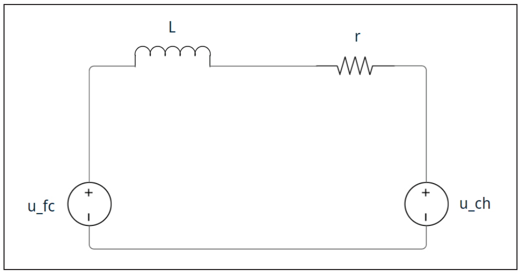

Figure 2.34 Simplified Smooth Inductor Electrical Circuit Model

Taking into account the simplified circuit model, by applying Kirchhoff's voltage law and translating the resulting equation into the Laplace domain, we obtain the relationship as presented in Equation 2.42.

$$u_{fc} = i_{fc}.(Z_L + Z_r) + u_{ch} \tag{2.42}$$

where Z_L=LS

and Z_r=r

That gives the transfer function presented in Equation 2.43

$$i_{fc} = \frac{u_{fc} - u_{ch}}{r + LS} \tag{2.43}$$

If we multiply numerator and denominator of this transfer function by $\frac{1}{r}$, then we have:

$$i_{fc} = \frac{u_{fc} - u_{ch}}{\frac{1}{r} + \frac{LS}{r}} \tag{2.44}$$

And that's the mathematical model that has been used in the Simulink model represented in Figure 2.35.

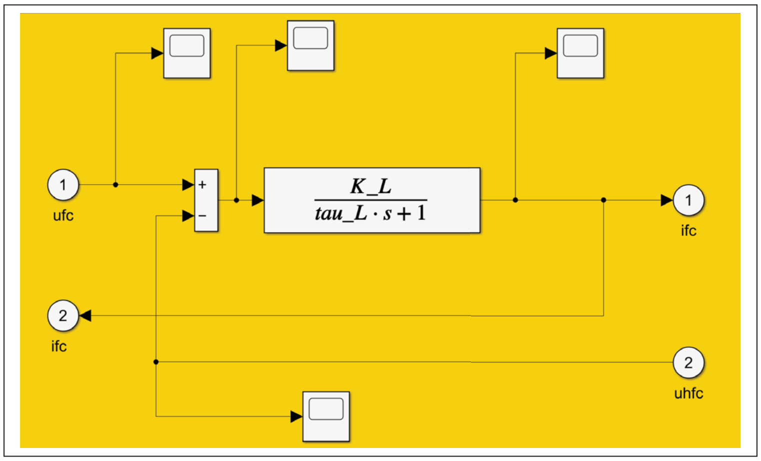

Figure 2.35 Implementation of the Smoothing Inductor Element in Simulink

In Figure 2.35, K_L=$\frac{1}{r}$ and the time constant or tau_L=$\frac{L}{r}$.

Table 2.8 presents the parameters of the smooth inductors, which are adopted from the IEEE VTS Motor Vehicle Challenge 2020 Solano *et al.* (2019).

Table 2.8 Smooth Inductor Parameters

Parameter	Value
V_e	65 V (Boost chopper average input voltage)
V_s	80 V (Boost chopper output voltage)
f_{PWM}	1×10^4 Hz (PWM frequency)
δ_{iL}	5 A (Current variation limit)
$\delta_{u_{\text{bus}}}$	1 V (DC bus variation limit)
R_{ch}	$\frac{80}{300}$ ohm (Equivalent maximal load resistor)
L	$\frac{V_e(1-\frac{V_e}{V_s})}{\delta_{iL} f_{\text{PWM}}}$ H (Inductance)
r_L	$\frac{L}{50\times10^{-3}}$ ohm (Winding resistance)
K_L	50 (Gain)
τ_L	0.5 s (Time constant response)

The boost chopper within the EMR framework is depicted as a mono-physical converter, similar to the illustration in Figure 2.15. This component's function is to adjust the output voltage to the specific demands of the vehicle by modulating the duty cycle of the boost DC-DC converter. Considering the boost chopper as a transformer, as demonstrated in Figure 2.36, with a transformation ratio denoted by m_{hfc}, we can articulate its mathematical expression as seen in Equation 2.45 Manish (2021).

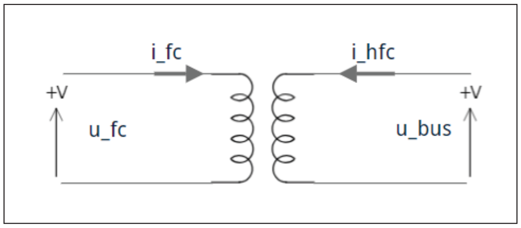

Figure 2.36 Simplified transformer Electrical Circuit Model

$$m_{hfc} = \frac{u_{hfc}}{u_{bus}} = \frac{i_{hfc}}{i_{fc}} \tag{2.45}$$

With the established mathematical model for the boost chopper, and taking into account its efficiency, the final design of the boost chopper block is completed. Figure 2.37 in the Simulink environment illustrates this final design.

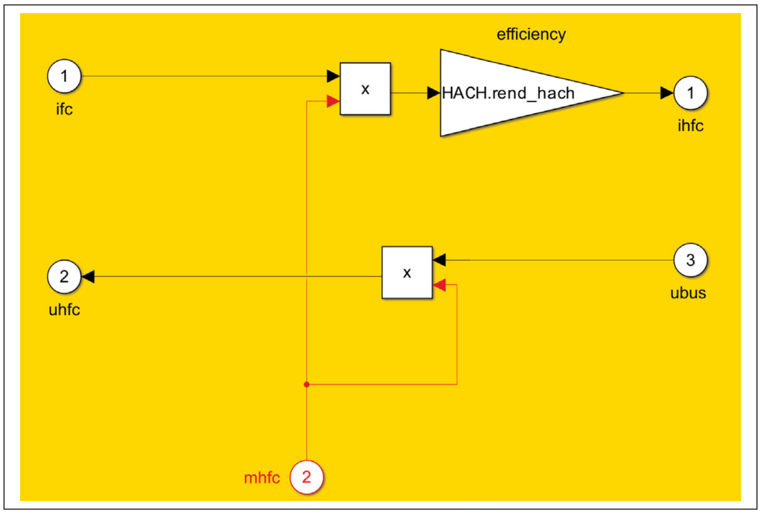

Figure 2.37 Implementation of the Boost Chopper Element in Simulink

The boost chopper model is also adopted from the IEEE VTS Motor Vehicle Challenge 2020 Solano *et al.* (2019). The efficiency depicted in the figure is assumed to be 0.95, therefore, HACH.rend_hach = 0.95.

2.5.1.3 The Parallel Connection Element

The variable m_{hfc} serves as a determining control parameter, it is known as the control variable and modulates the proportion of fuel cell current i_{fc} that contributes to the electric drive's demand. In our energy management strategy, it is sufficient to regulate a single current source—either from the fuel cell or the battery—to satisfy the traction system's requirements, particularly the electric drive. Given that the fuel cell is the primary energy provider in our system, we choose to control the fuel cell current, therefore we labeled the i_{fc} as the objective variable. Consequently, the corresponding demand from the battery is inherently managed. The coupling of these two energy sources adheres to the principles defined in Equation 2.46, which ensure the total current supplied to the traction system i_{ts} is the sum of the current from the battery i_{bat} and the fuel cell i_{fc}, where i_{bat} also equals the bus current i_{bus}:

$$i_{ts} = i_{bat} + i_{fc}, \quad i_{bat} = i_{bus} \tag{2.46}$$

In the designed system, the aforementioned mathematical model is explained within a mono-physical coupling element, termed the *Parallel Connection*. The corresponding EMR pictogram aligns with the one displayed in Figure 2.18. The implementation of this model within Simulink is detailed in Figure 2.38, which presents a visual representation of the parallel connection's functionality.

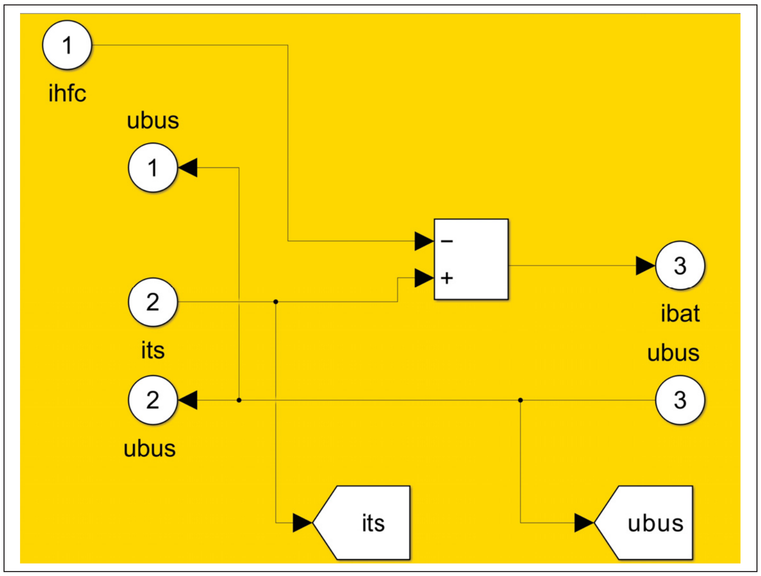

Figure 2.38 Implementation of the Parallel Connection Element in Simulink

2.5.2 The IBC layer-ESS

After fully developing the primary layer of the EMR, we proceed to establish the current control path within the IBC layer. As in the traction subsystem, a PI controller is utilized to minimize the error between the actual fuel cell current i_{fc_mes} and the reference current i_{fc_ref}. This reference current will be optimized within the EMS block, which is to be elaborately presented in Chapter 3. Within the IBC layer, the control *tuning variable*, denoted as m_{hfc}, must be finely tuned, given that the objective variable in our case is the fuel cell current i_{fc}. To fulfill this objective, it is essential to first construct a detailed and thorough circuit equivalent of the EMR layer. Subsequently, by inverting this circuit, we can formulate the control block and determine the appropriate tuning variable.

2.5.2.1 Inversion of Smooth Inductor & Boost Chopper

Integrating the equivalent circuits of the smoothing inductor and the boost chopper, as detailed in Figures 2.34 and 2.36, enables us to conceptualize the entire system's equivalent circuit. The detailed schematic of this comprehensive equivalent circuit is depicted in Figure 2.39.

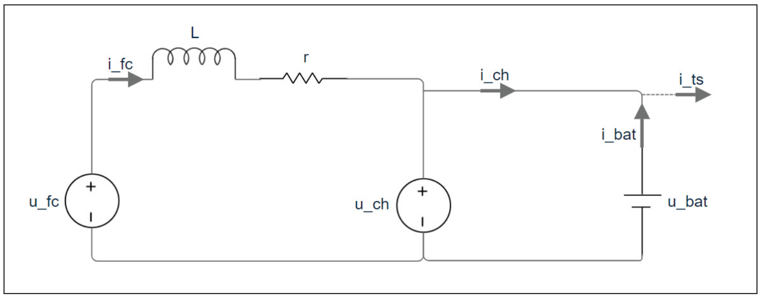

Figure 2.39 Integrated Equivalent Circuit of the ESS Combining Smoothing Inductor and Boost Chopper

The mathematical equation for this equivalent circuit is given as Equation 2.51.

$$u_{fc} = u_L + u_{ch} \tag{2.47}$$

And:

$$u_L = i_L r + L \frac{d_{i_L}}{d_t} \tag{2.48}$$

So:

$$u_{fc} = i_L r + L \frac{d_{i_L}}{d_t} + u_{ch} \tag{2.49}$$

Where:

$$\begin{cases} i_L = i_{fc} \\ u_{ch} = u_{hfc} \end{cases} \tag{2.50}$$

By applying an integral to both sides of the aforementioned equation:

$$i_{fc} = \int_0^t (u_{fc} - u_{ch}) d_t + i_{fc} r_L \tag{2.51}$$

To be able to translate this mathematical model into Simulink, we need to rewrite the equation in the Laplace domain which is given in Equation 2.52.

$$i_{fc} = \frac{\frac{1}{r_L}}{(\frac{L}{r_L})S + 1} \times (u_{fc} - u_{ch}) \tag{2.52}$$

In the Simulink model, we have:

$$\begin{cases} \frac{1}{r_L} = K_L \\ \frac{L}{r_L} = tau_L \end{cases} \tag{2.53}$$

To generate the PI controller block diagram for our ESS in the Laplace domain and outline its transfer function, we can utilize the established mathematical model. Figure 2.40 displays the schematic representation of the PI controller for the current loop.

The PI controller's transfer function is then detailed in Equation 2.54.

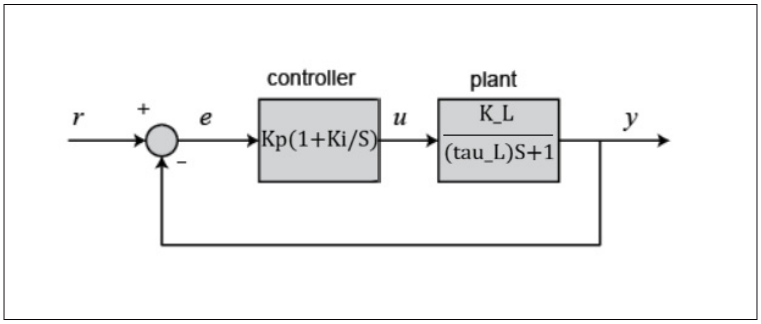

Figure 2.40 A Schematic Representation of the PI Controller for the Current Control Loop in the Laplace Domain

$$\frac{y}{r} = \frac{K_p K_L S + K_i K_L}{(tau_L)S^2 + (1 + K_p K_L)S + K_i K_L} \rightarrow \begin{cases} 2\zeta\omega_n = \frac{1+K_p K_L}{tau_L} \\ \omega_n^2 = \frac{K_i K_L}{tau_L} \end{cases} \tag{2.54}$$

The controller unit for the current control loop in the ESS is demonstrated through the inversion of an accumulation element, similar to what we observed in the traction subsystem. This process is visualized in Figure 2.24. By applying the transfer function to our controller block, the resulting Simulink implementation is displayed in Figure 2.41.

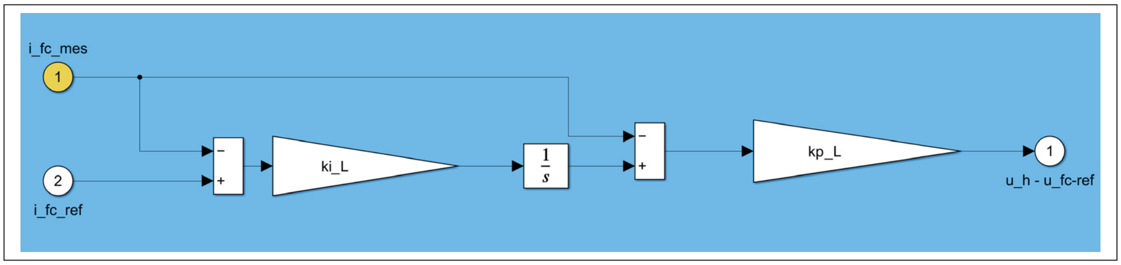

Figure 2.41 Simulink Representation of the PI Controller for Current Control in ESS

For this current control loop, we have assumed that $\zeta = 1$ and the time constant, τ_L, is $\frac{1}{3}$ of the boost chopper time constant based on the methodology used in Solano *et al.* (2019). According to this, the rest of the parameters can be calculated as shown in Equation 2.54.

Table 2.9 Current Control Loop Parameters

Parameter	Value
ζ	1 (Damping coefficient)
τ_{L_des}	0.1667 (Time response at ±5%)
ω_{n_L}	28.4640 (Pulsation)
k_{p_L}	0.5492 (Proportional coefficient)
k_{i_L}	14.7502 (Integral coefficient)

Alongside the PI controller, the system incorporates a low-frequency filter set at 15 mHz and adheres to a ramp rate limit ranging from 6 to 20 A/sec for generating the fuel cell current i_{fc_ref}, based on the fuel cell's power. This approach is aimed at minimizing the risk of stack faults and improving the FC's lifetime Depature *et al.* (2016). The entire setup is depicted in Figure 2.42.

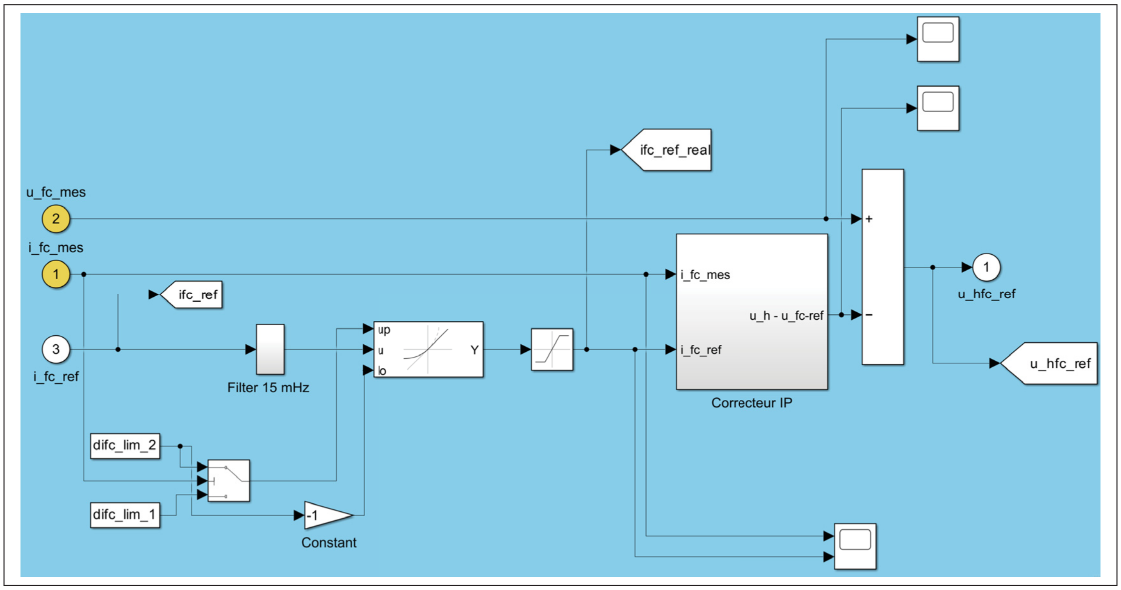

Figure 2.42 Implementation of ESS Controller in Simulink Framework

As previously discussed, the objective of the ESS IBC layer is to determine the modulation ratio in order to control i_{fc}. Through the inversion of the smoothing inductor's model, we obtain the reference voltage for the chopper u_{hfc_ref}. Similarly, inverting the model of the chopper yields the reference for the modulation ratio m_{hfc}. Given the simplicity of the boost chopper's design, identified as a monophysical converter, its inversion process is straightforward. It necessitates reversing the mathematical formula of the boost chopper, as detailed in Equation 2.45. This reversal leads to the IBC configuration for the boost chopper, as specified in Equation 2.55 and depicted in Figure 2.43.

$$m_{hfc_{ref}} = \frac{u_{hfc_{ref}}}{u_{bus}} \tag{2.55}$$

Where:

$$u_{bus} = u_{bat} \tag{2.56}$$

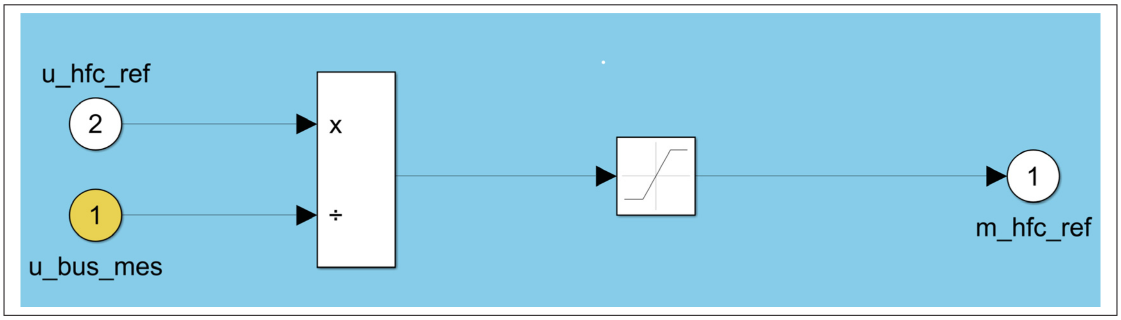

Figure 2.43 Implementation of Boost Chopper Inversion in Simulink Framework

The saturation block is employed to maintain the modulation ratio within the range of 0 to 1. This ratio determines the percentage of i_{fc} that needs to pass through to meet the system requirements. Consequently, it is essential that this value does not exceed one or fall below zero.

CHAPTER 3

ENERGY MANAGEMENT STRATEGY FOR OPTIMIZING FUEL CELL CURRENT CONTROL

As discussed before in Chapter 1, HEVs provide enhanced fuel efficiency and emissions reduction through integrated energy storage and electric drive systems, allowing for advanced features like engine-off idling and regenerative braking. The EMS's primary role is to optimize power distribution between the engine and energy storage to maximize fuel efficiency and minimize emissions, maintaining vehicle performance Serrao *et al.* (2011). This research focuses on the efficient allocation of power demand between the battery and the fuel cell, monitored through vehicle dynamics, with the aim of decreasing hydrogen fuel usage and extending battery longevity while inherently operating with zero emissions due to the vehicle's power sources. Adopting a rule-based methodology with an FLC, this study seeks to develop an EMS that optimally balances battery longevity and hydrogen consumption, leveraging FLC's capability to handle imprecise data and complex scenarios for sustainable and efficient vehicle operation.

3.1 Objectives of the Energy Management Strategy in Our FCEV System

An effective energy management strategy is crucial for ensuring the stability and fuel efficiency of the entire system. Positioned at the highest tier of the powertrain control order-global control level, known as the Strategy Layer within the EMR framework, the EMS plays an essential role in optimizing the distribution of power across available energy sources. It has been previously demonstrated that certain situations necessitate external control criteria, such as i_{fc}_ref in our context, especially when addressing the inversion of coupling elements. In such scenarios, the introduction of the third and critical domain of EMR becomes imperative, requiring EMS to furnish additional references for control. The literature reveals a variety of methods to tackle this complex optimization challenge, with rule-based and optimization-based methodologies emerging as the primary strategies as shown in Figure 1.5. These approaches provide the foundational strategies for the development of EMS techniques, showcasing the spectrum of solutions available Ouddah & Adouane (2019), Huangfu, Yu, Zhuo, Shi & Zhang (2021), Lenoir *et al.*.

Our study seeks to evaluate the efficacy of a fuzzy logic control methodology in enhancing battery lifespan, minimizing system weight, and reducing hydrogen consumption. We aim to compare its performance against scenarios lacking a comprehensive global control or employing a basic rule-based approach, highlighting the potential advantages of integrating advanced fuzzy logic techniques in energy management strategies.

3.2 Introduction to Fuzzy Logic

The EMS is crucial for allocating power between the fuel cell and battery to meet the vehicle's power needs, considering factors like keeping the battery's SOC within an optimal range. A promising technique for energy management in hybrid electric systems is fuzzy logic control, which can handle difficult-to-predict variables like traffic flow and road inclines with ease. Its application in numerous studies confirms its simplicity and real-time control efficacy. FLC strategies in FCHEVs often rely on a set of IF-THEN rules based on input parameters, a technique known for its ability to mimic human decision-making processes in scenarios marked by ambiguity or uncertainty. This adaptability makes fuzzy logic particularly valuable in managing the complex and variable dynamics of hybrid electric vehicle operation Sulaiman *et al.* (2018)Saib, Hamouda & Marouani (2017).

From the standpoint of electrical engineering, fuzzy logic uses human knowledge and linguistic labels in a unique way to model physical processes and develop control systems, building on its usefulness in HEV energy management. Because of its adaptability, it may be used in a variety of settings. Bicycling is a common activity where fuzzy control is demonstrated since riders don't need to rely on exact acceleration or speed readings to stay in control. Rather than using quantitative judgments like "fast," "slow," "near," or "far," the human brain determines when to brake or accelerate. This linguistic label-based intuitive control method reflects the core of fuzzy logic control systems, merging human-like reasoning with the previously discussed technological optimization of energy management in FCHEVs Solano (2012).

3.2.1 Introduction to Designing a Fuzzy Inference System

Contrary to the binary true or false norm of classical logic, fuzzy logic is a method for representing logical thinking. Alternatively, a range of truth values is introduced, where 0 represents total falsehood and 1 represents the absolute truth. Given the complexity and uncertainty that are sometimes present in real-world circumstances, this technique enables a deeper comprehension of statements.

Fuzzy logic enables the creation of a fuzzy inference system (FIS), a mechanism that transforms a collection of inputs into outputs through human-interpretable rules, bypassing the need for abstract mathematical formulations. This function finds widespread use in control applications, where it processes references and measurements to generate an actuating signal based on a set of fuzzy logic-based rules. This approach allows for more intuitive and adaptable control strategies in various applications Douglas (2021). Figure 3.1 illustrates the FIS schematic within a control system.

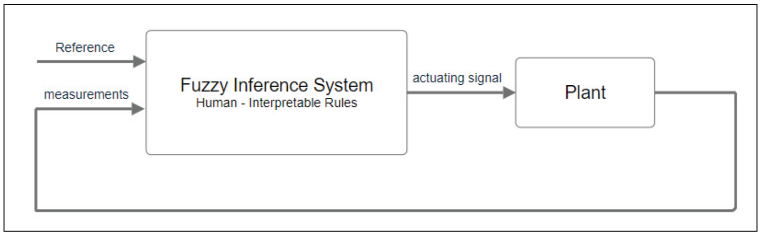

Figure 3.1 Schematic Representation of a Fuzzy Inference System (FIS), illustrating the process of transforming inputs into outputs through human-interpretable rules within control applications

Fuzzy logic is useful in a wide range of decision-making processes, demonstrating its versatility beyond its use as a conventional control method. The creation of a FIS does not require an already-existing model, which makes it especially useful for elaborately unknown complicated systems. It is possible to create and implement customized rules if one has enough intuition and familiarity with the system in issue. An FIS represents a branch of artificial intelligence by enabling computers to simulate human cognitive approaches to problem-solving. Through fuzzy logic and the implementation of an FIS, it is possible to translate experience-based knowledge into a format comprehensible to computers, utilizing logical rules.

To exemplify, consider the application within a banking context, where the FIS assesses the risk associated with granting loans based on comprehensive personal and financial data.

In the banking industry, for instance, a banker may utilize fundamental rules based on credit ratings to assess loan risk: excellent credit denotes low risk, neutral credit implies medium risk, and bad credit indicates high risk. These guidelines serve as a predictive framework for assessing the possibility of loan repayment because they are based on gathered information and data. Therefore, using the rule-based information that already exists is a useful substitute for developing intricate mathematical models to evaluate financial actions. Because language is inherently imprecise, it can be difficult to use experiential information to inform decisions. It adds a binary logic that facilitates analysis but misses linguistic nuances when words like "good credit" are defined in absolute terms, such as a score of 750 or higher. Accepting the imprecision of linguistic terminology is crucial in order to accurately reflect the collective understanding of the banking industry as well as the nuance of language. Fuzzy logic is a better option because binary logic is inadequate in this regard. Because fuzzy logic takes into account the gradation and diversity of human language, it offers a sophisticated and adaptable way to integrate industry knowledge into decision-making procedures. Fuzzy logic transforms specific, precise inputs, such as exact credit ratings, into fuzzy variables through a process known as fuzzification. This allows fuzzy logic rules to be applied to these variables, generating new fuzzy numbers. Subsequently, these fuzzy numbers undergo defuzzification, converting them back into precise, specific outputs. The process, from fuzzification through to defuzzification, is illustrated in Figure 3.2, detailing each step involved in translating crisp inputs into fuzzy variables and back into crisp outputs.

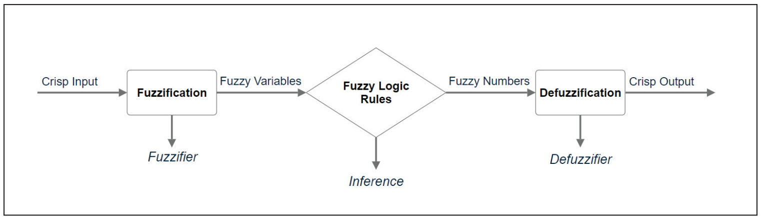

Figure 3.2 Illustration of the Fuzzification and Defuzzification Processes in Fuzzy Logic, showcasing the transformation of precise inputs into fuzzy variables and their subsequent conversion back into specific outputs

In applying fuzzy logic to our banking example, envision conducting a survey among 100 bankers to determine their perception of the boundary between bad to neutral credit, and neutral to good credit. Given the subjective nature of these categories, it's expected that their responses vary. Suppose the consensus is that a score of 750 or higher is consistently viewed as good credit, but only half consider a score of 700 as good, and a score of 650 is unanimously not seen as good. This exercise effectively maps out the membership function for what constitutes good credit. Similarly, one could establish membership functions for neutral and bad credit, resulting in three intersecting curves. This illustrates that credit scores can simultaneously hold varying degrees of membership across different categories, such as a score of 800 being fully classified as good credit, whereas a score of 700 might be equally split between good and neutral credit categories.

In the context of our banking example, consider the fuzzification process applied to a credit score of 660. This score, intuitively understood as predominantly neutral, is quantitatively represented through membership functions as 90% neutral and 10% good, translating into a fuzzy representation of (0, 0.9, 0.1) as it is shown in Figure 3.3. This transformation from a precise input to a fuzzy value exemplifies the process of fuzzification, the initial step in our fuzzy logic framework.

Following fuzzification, the inference stage is approached by evaluating the input's implications based on predefined logical rules. For a credit score of 660, the inference might deduce that since the credit is 10% good, there is a corresponding 10% likelihood of the risk being low.

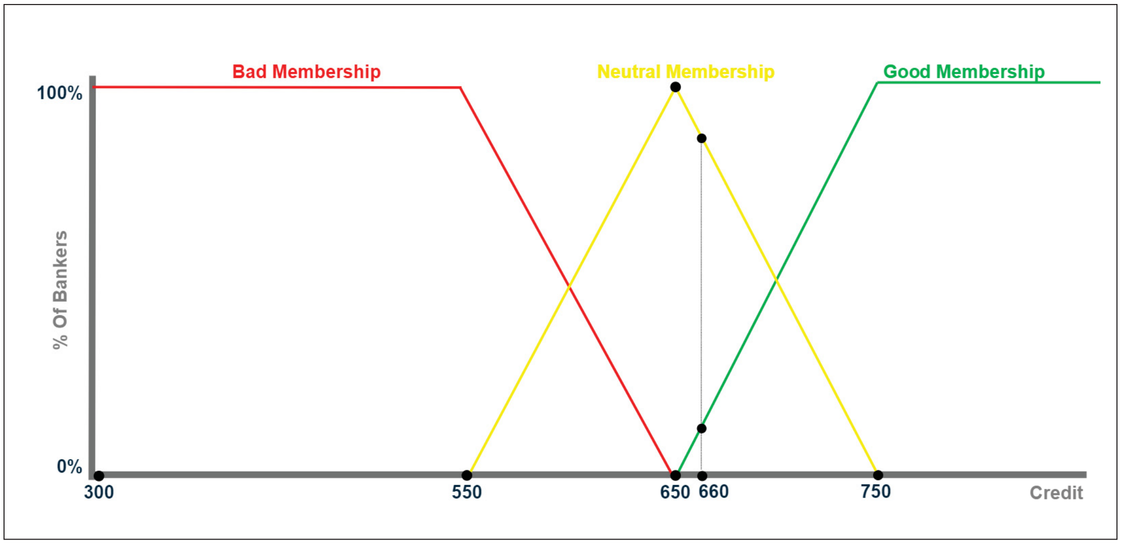

Figure 3.3 Definition illustration of membership functions within the banking sector example, showcasing the transition of credit scores into categories of bad, neutral, and good credit. Each line represents the degree of membership, varying from 0 to 100%, for credit scores in the respective categories, highlighting the fuzzy logic approach to quantifying creditworthiness

Similarly, the 90% neutrality of the credit score suggests a 90% probability of medium risk, with no portion of the credit score falling into the bad category, hence a 0% likelihood of high risk. This analysis results in a fuzzy variable that, due to the simplicity of our example's rules, mirrors the initial fuzzy numbers but could potentially differ significantly with more complex rule sets. This procedure is again represented in Figure 3.4.

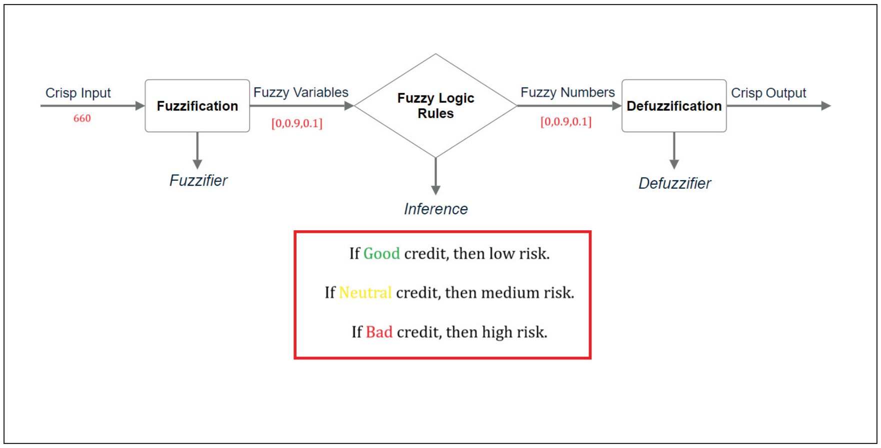

Figure 3.4 Illustration of Fuzzification Process showcasing investigation for a credit score of 660

The process concludes in defuzzification, where the calculated fuzzy number is converted back into a precise, actionable output. The role of the membership function within this process is pivotal. It quantifies and categorizes the degree to which a given input (like a credit score) aligns with certain criteria (e.g., good, neutral, or bad credit). This categorization is not binary but rather expressed in terms of a percentage, indicating the extent of membership within each category. This nuanced approach allows for a more sophisticated and realistic representation of variables that are inherently vague or subjective, such as creditworthiness.

In conclusion, the membership function serves as the cornerstone of the fuzzification process, enabling the conversion of crisp inputs into fuzzy values. These fuzzy values, through the application of logical rules during the inference phase, facilitate a comprehensive and nuanced assessment of risk, which can then be translated back into precise outputs during the defuzzification stage Douglas (2021).

After the process of inference is finished and a new fuzzy number is obtained, the next step is called defuzzification. In this step, the fuzzy value is transformed back into an exact, measurable output. To give an example, consider surveying one hundred bankers to create membership functions that convert the qualitative risk ratings (low, medium, and high) into precise numerical values. For simplicity, we assume that these functions are defined as follows: low risk is associated with 25% and below, declining linearly up to 50%; medium risk is associated with 25% to 75%; and high risk is associated with 50% to 75%, increasing linearly.

Defuzzification employs various methodologies, with one common approach involving the truncation of membership functions at the percentage level indicated by the output—90% medium and 10% low risk, in this instance. This truncation produces two trapezoidal shapes, which are then combined into a single geometric figure. The defuzzified value corresponds to the x-coordinate of this figure's centroid, which, in our example, approximates to 46%. This percentage suggests that a credit score of 660 poses a 46% risk level, aligning closely with the anticipated perception that such a score marginally exceeds the neutral credit threshold, thereby constituting a somewhat lower risk.

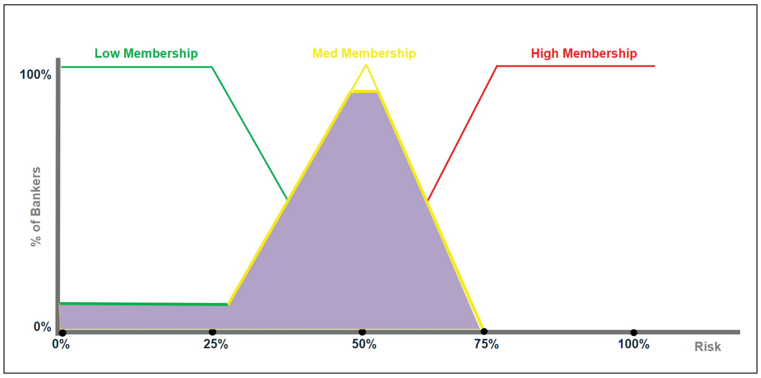

Figure 3.5 Illustration of transforming fuzzy risk levels into a precise risk percentage through defuzzification

The defuzzification procedure, illustrated in Figure 3.5, demonstrates how fuzzy logic enables the conversion of imprecise linguistic expressions into tangible, useful information, so serving as a bridge between qualitative assessments and quantitative analysis.

Another significant advantage of fuzzy logic is its flexibility in problem-solving, particularly in the ability to develop a fuzzy inference system from a bottom-up perspective. This approach allows for the initial establishment of a foundational framework without a detailed understanding of the specific membership functions or rules. Subsequently, data can be employed to systematically refine and determine the parameters of the inference system. This process bears resemblance to the method used in tuning neural networks within the domain of machine learning, enabling the fine-tuning of the fuzzy inference system based on empirical data.

A key benefit of this methodology is the resultant model's interpretability. Unlike many machine learning models, the rules within a fuzzy inference system remain transparent and understandable, facilitating easier verification and certification of the system. This attribute is especially valuable in applications requiring rigorous validation processes. This thesis adopts this data-driven approach to design our system, leveraging the interpretability and adaptability of fuzzy logic to meet our specific system requirements Douglas (2021).

3.2.2 Implementation of Fuzzy Logic in Studied System

In this section, the focus shifts to the practical application of FLC within the particular system that is being studied. Initially, the discussion will cover the inputs and outputs designated for the FLC, providing a foundational understanding of how the system interprets data and what it aims to achieve through its processing.

Following this, attention will be directed towards the membership functions, the core components that translate crisp inputs into fuzzy values. This part will detail the methodological approach to defining these functions, explaining the rationale behind their shapes, ranges, and the degrees of membership they represent. This explanation will include insights into how these functions were designed to capture the subtle behaviors and characteristics of the system's variables.

Lastly, the rules outlined in the FIS will be introduced in this part. These rules are crucial in directing the FLC's decision-making process by specifying how inputs should be processed and integrated to generate the intended outputs. The discussion will provide insight into these rules' rational structure and how they combine intuitive methods with expert knowledge to provide efficient and understandable system control.

3.2.2.1 Defining FLC Input and Output

The input to our customized FLC is the SOC of the battery, while the output is a coefficient that subsequently determines the i_{fc_ref}. This selection of input and output is strategic, aimed at achieving the system's goals. By managing the SOC, we can command the system to maintain it within a range that ensures the battery pack's longevity. Adjusting the i_{fc_ref} coefficient allows us to specify the optimal current required from the fuel cell to recharge the battery, thus optimizing hydrogen usage and extending the fuel cell's lifespan by preventing it from operating at its maximum output merely to recharge the battery.

3.2.2.2 Development of Membership Functions

The initial step in developing the membership functions for the battery's SOC involves establishing its range. This determination is based on analyzing the system under worst-case scenarios for both the minimum and maximum SOC levels: the maximum being when the FC operates continuously, and the minimum when the FC remains off all the time. Such scenarios suggest that the SOC fluctuates between 0.27 and 0.71. To ensure a margin of safety, we expanded this range to span from 0.2 to 0.8. Figure 3.6 illustrates the membership function plot for the battery SOC, with the range set from 0.2 to 0.8. The allocation of values to different membership functions was achieved through manual tuning and observation of the system's response to various settings. In this framework, LS denotes Low SOC, MS indicates Medium SOC, and HS represents High SOC.

Now that we have the membership functions for our input, we must follow the same procedure for i_{fc_coef}, which is the FLC's output. This variable's range is methodically set between 0 and 1, since it is a coefficient. This choice simplifies the system, makes it easier to tune, and makes it more straightforward to understand in the future if changes or additions are made, like adding more inputs. The output produced by the FLC is then adjusted and justified by adding a gain factor. The foundation of this system's configuration is to allow the FC to provide more power when the SOC is low, satisfying the system's power requirements and making it

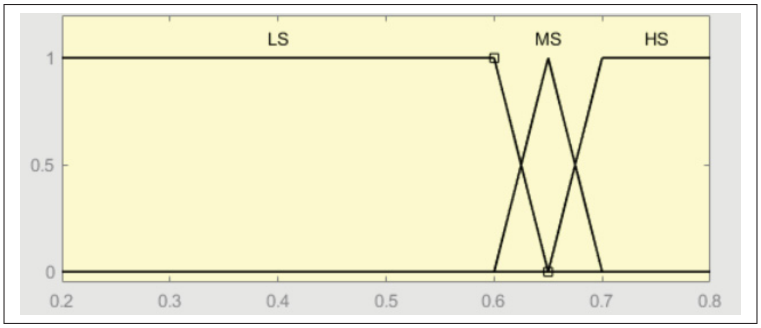

Figure 3.6 Membership Function Plot for Battery SOC, illustrating the defined range from 0.2 to 0.8 with categories LS (Low SOC), MS (Medium SOC), and HS (High SOC) determined through manual tuning and system behavior observation

easier for batteries to be recharged in order to raise the SOC. In contrast, the FC's contribution decreases as the SOC rises in order to keep the SOC within the intended ranges and to enable a higher battery power demand, particularly during high dynamic phases. As a result, in low SOC situations, the i_{fc_coef} is maximized, whereas in high SOC situations, it is minimized. Analyzing system behavior and manual adjusting were used to determine the values assigned to the various membership functions, much like in earlier steps.

Figure 3.7 displays the membership function plot for i_{fc_coef}, with a range from 0 to 1. Within this model, HT denotes the minimal i_{fc_coef} share, MT signifies a moderate i_{fc_coef} share, and LT indicates the maximum share of i_{fc_coef}.

3.2.2.3 Establishing Fuzzy Inference System Rules

Following the establishment of membership functions for both the input and output, it is essential to articulate the rules. These rules have been meticulously crafted and simplified in terms of their range to facilitate ease of development and comprehension. Considering that the FC must increase the power supply when the SOC is low in order to meet system power demands and facilitate battery recharging to raise the SOC; conversely, when the SOC rises, the FC's input decreases in order to keep the SOC within desired bounds and to accommodate the increased

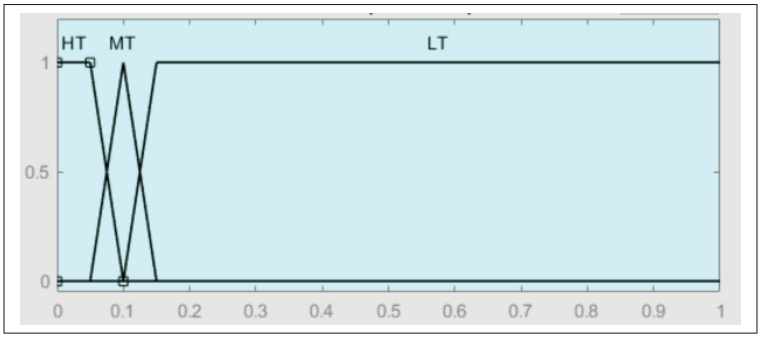

Figure 3.7 Membership Function Plot for i_{fc_coef}, showing the range from 0 to 1 with categories HT (minimal share), MT (moderate share), and LT (maximum share) based on manual tuning and system analysis

power demand from the battery, particularly in high dynamic conditions. Using this justification and three membership functions for every condition, we arrive to the following three fundamental principles:

- If the SOC is low (as determined by the LS input membership function), then the i_{fc_coef} should be at its maximum (corresponding to the LT output membership function).
- If the SOC is medium, then a medium share of i_{fc_coef} is necessary.
- Lastly, at high SOC, the minimum share of i_{fc_coef} should be utilized.

Figure 3.8 illustrates the application of these rules within Simulink, showcasing the operational logic of the FLC in this context.

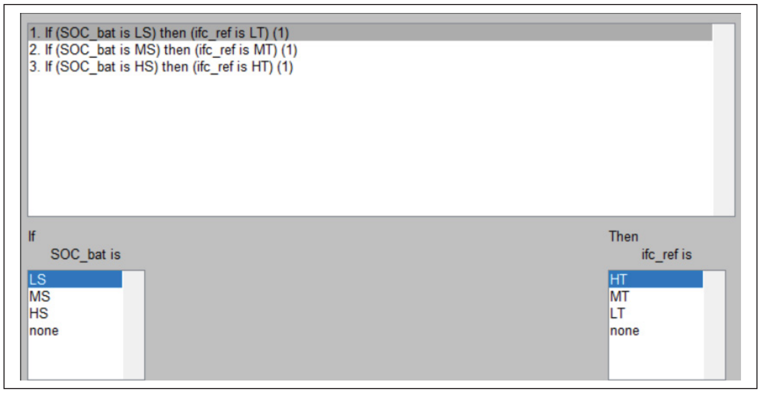

1. If (SOC_bat is LS) then (ifc_ref is LT) (1)
2. If (SOC_bat is MS) then (ifc_ref is MT) (1)
3. If (SOC_bat is HS) then (ifc_ref is HT) (1)

Figure 3.8 Visualization of the Fuzzy Logic Controller (FLC) rules applied in Simulink, demonstrating the correlation between SOC levels and i_{fc_coef} shares for low, medium, and high SOC conditions

3.2.2.4 Defining the Recharge Current: Determining Fuel Cell Contribution for Battery Charging

As was previously mentioned, the FC current allocated for battery recharging is determined by a coefficient that the FLC produces. Optimizing this current is important for two main reasons: first, it will extend the fuel cell's lifespan by preventing demands for its maximum current capacity; second, it will reduce the amount of hydrogen used, since higher current demands on the fuel cell equate to higher hydrogen consumption. Therefore, it is crucial to adjust the maximum recharge current, represented as i_{rech}, in order to guarantee the fuel cell's durability and minimize hydrogen consumption.

To achieve this optimization, it is necessary to formulate the mathematical equation representing the current that charges the battery, derived from the FC. This relationship is shown in Equation 3.1.

$$I_{rech\_bat} = m_{hfc} \times I_{fc} \tag{3.1}$$

Where I_{rech_bat} needs to be optimized.

Equation 3.2 is the result of rephrasing the entire equation in terms of the fuel cell current in order to optimize the recharge current, i_{rech_bat}.

$$m_{hfc} = \frac{u_{fc\_mes} - PI_{output}}{u_{bus\_mes}} \tag{3.2}$$

In this equation, u_{fc_mes} denotes the voltage-current function of the FC, and PI_{out} represents the output of the PI controller dedicated to fuel cell current regulation, as detailed in the preceding chapter. The parameter m_{hfc} acts as a critical control variable, while u_{bus_mes} is considered equivalent to the voltage at the DC bus. As Figure 3.9 illustrates, the bus voltage variation is considered small, roughly 5%, and is therefore handled as a constant value of 740 V.

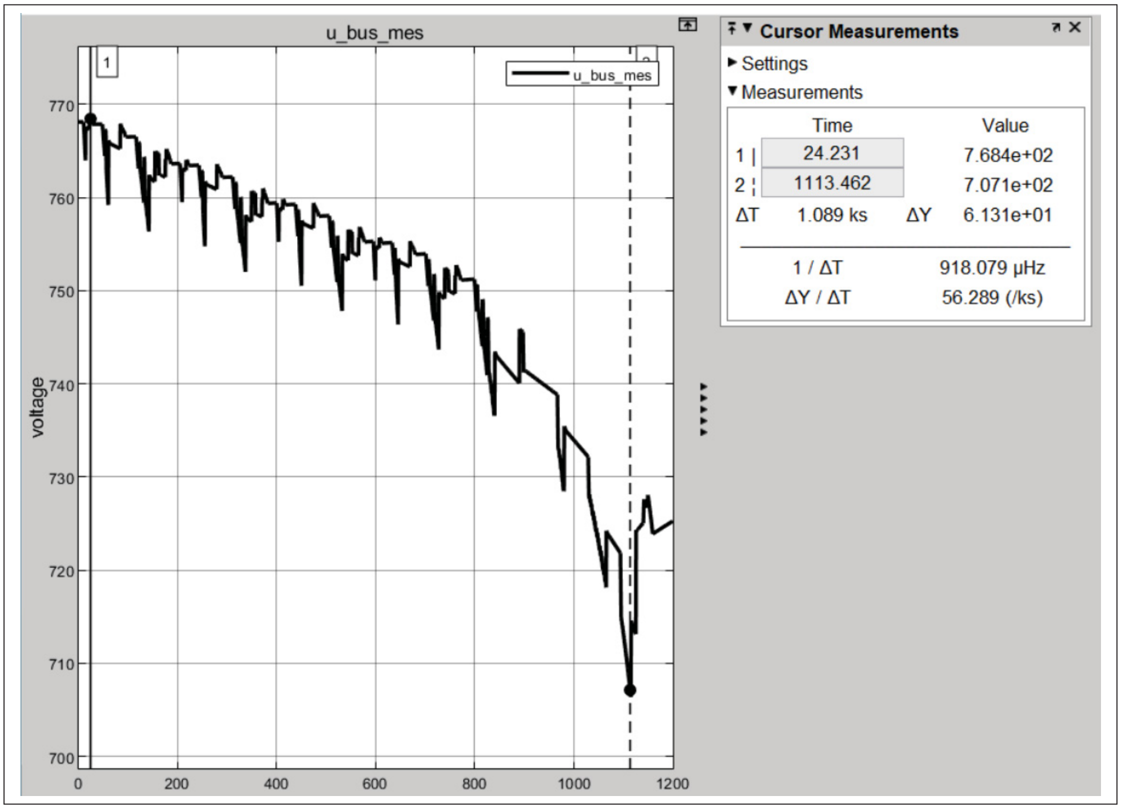

	Time		Value
1	24.231		7.684e+02
2	1113.462		7.071e+02
ΔT	1.089 ks	ΔY	6.131e+01

1 / ΔT 918.079 µHz
ΔY / ΔT 56.289 (/ks)

Figure 3.9 Depiction of the DC bus voltage, treated as a constant at 740 V due to minimal variation

Based on the correlation between the controller's input and output, a straightforward numerical comparison leads to the formulation of Equation 3.3.

$$PI_{out} = \frac{1}{50} \times I_{fc} \tag{3.3}$$

Therefore, with reference to Equation 3.3 and considering the voltage-current function of the fuel cell as illustrated in Figure 3.10, it can be affirmed that Equation 3.2 has been comprehensively reformulated in terms of i_{fc} enabling us to optimize i_{rech_bat} in terms of i_{fc}.

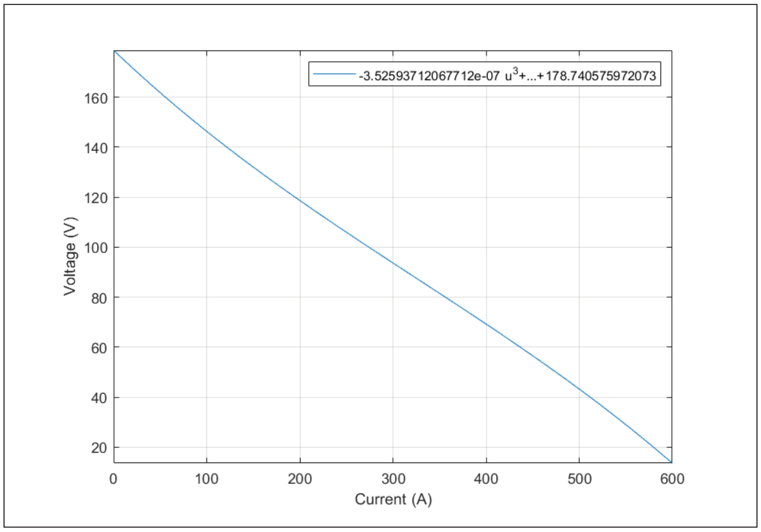

Figure 3.10 Fuel Cell Voltage-Current Relationship

Equation 3.4 presents I_{rech_bat} defined as a function dependent on i_{fc}.

$$f_{i_{rechmax}}(u) = \left(\frac{v_{fc}(u)}{U\_bus}\right) u \tag{3.4}$$

Where v_{fc} is expressed in Equation 2.40 and u represents i_{fc}.

Plotting this function yields a curve, for which the boundaries have been defined in accordance with the FC specifications, delineating a range from 0 to 600 Amps. As demonstrated by the curve in Figure 3.11, the optimal value for i_{rech_bat} occurs when $i_{fc} = 320A$. Therefore, to meet the system's stated objectives, i_{rech_bat} should not exceed $320A$.

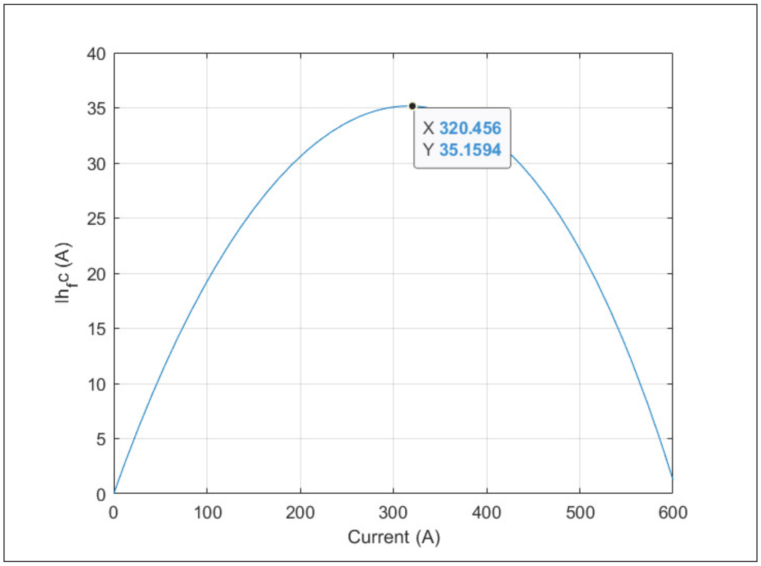

Figure 3.11 Curve depicting the relationship between i_{fc} and i_{rech_bat}, highlighting the optimal recharge current at $i_{fc} = 320A$

CHAPTER 4

DATA ACQUISITION AND SIMULATION

Starting with an overview of the prototype and its features, we conduct a thorough analysis of the prototype chosen for our case study in this last chapter. This lays the groundwork for specifying the modified vehicle's specifications. The next section of the chapter covers component sizing, in which we carefully calculate the dimensions of the fuel cell, hydrogen tank, electric motor, and battery pack to make sure they all match the needs of the system. We then introduce the driving cycle used for the model—namely, the NEDC—which serves as the benchmark for our simulations. Following this, the chapter unfolds with a step-by-step development of the system, beginning with the validation of the Traction subsystem and concluding with the Energy Storage subsystem. The investigation into the system's performance underlines the extent to which the project's objectives have been met. These objectives include minimizing hydrogen consumption, maximizing the durability of the battery's lifetime, and reducing the overall weight of the vehicle. Every part of this chapter advances a comprehensive comprehension of the effectiveness of the system and the accomplishment of these objectives.

4.1 Introduction and Overview of the Prototype

The selected prototype for this study is the Kenworth 2002, a heavy-duty long-haul truck equipped with a C10 Caterpillar engine. The general and engine specifications of the truck are detailed in Table 4.1, which provides a clear overview of its daily mileage capacity, engine power, Gross Vehicle Mass (GVM), and engine type.

Table 4.1 General and Engine Specifications of Kenworth 2002

Specification	**Value**
Mileage per day	300km
Engine	365-430 HP
GVM	52000 LB
Engine type	C10 Caterpillar

It is assumed that the reduced weight of the FCEV counterpart's powertrain offsets the mass contributed by the battery pack in the system Pardhi *et al.* (2022). Consequently, for the purposes of component sizing, the total vehicle mass is maintained at the original GVM of 52000 lbs, as applied to the examined vehicle.

4.1.1 Comprehensive Calculation of Required Power and Energy

Given that the vehicle's weight post-conversion remains consistent with the original GVM, it is logical to presume that the same power output is required for the electrified powertrain to propel the vehicle. The calculations commence with the maximum power advertised, factoring in the most demanding scenarios to accommodate potential increases in load, dynamic requirements, or auxiliary components that may impact performance.

$$\text{The maximum advertised power: } P = 430\text{hp} = 320\text{KW} \tag{4.1}$$

$$\text{Assuming daily mileage and average speed: } x = v \times t \text{ and } v = 90\frac{km}{h} \tag{4.2}$$

$$\text{So, travel time: } t \approx 3.5\text{h} \tag{4.3}$$

$$\text{For required energy: } E = P \times t \tag{4.4}$$

$$\text{So } E = 320\text{Kw} \times 3.5\text{h} = 1120\text{KWh} \tag{4.5}$$

$$\text{Assuming electric motor efficiency at 95\%: } ESS_p = \frac{320}{0.95} \approx 337\text{KW} \tag{4.6}$$

In this context, ESS_p signifies the total power demand on the Energy Storage Subsystem. It is important to note that within the scope of this study, the sizing of the battery pack is determined based on the peak power requirement. This approach ensures that the battery is capable of supplying power during high dynamic periods, which contributes to mitigating the rate of FC degradation. Subsequently, the hydrogen tank is dimensioned based on the maximum energy demand, as the fuel cell serves as the primary generator of energy, necessitating its ability to consistently fulfill the system's energy needs.

Consequently, this analysis concludes with the definition of the system's power and energy requisites as outlined in Equations 4.7 and 4.8, concluding the specifications for the Energy Storage Subsystem's capacity.

$$ESS_P = 337\text{kW} \tag{4.7}$$

$$ESS_E = 1120\text{KWh} \tag{4.8}$$

4.1.2 Specifications of the Electric Motor

With the maximum power required to propel the vehicle established, the next phase involves selecting an appropriate EM. The selection criteria for this process mandates that the peak power capacity of the EM surpasses the power output of the ESS:

$$EM_{Peak\_Power} > ESS_P \tag{4.9}$$

In this project, the choice has been made to employ an electric motor from the GVM series produced by Parker Corporation. The specifications of the selected EM are detailed in Figure 4.1.

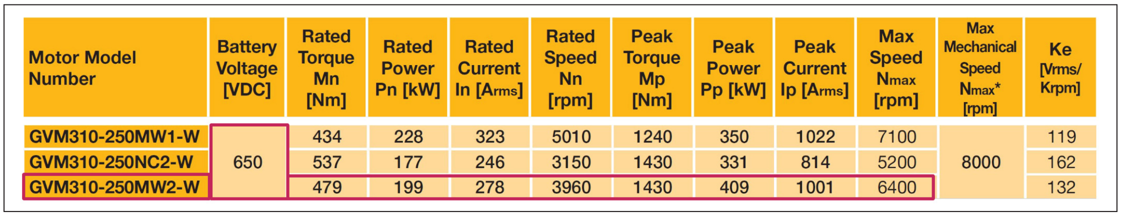

Motor Model Number	Battery Voltage [VDC]	Rated Torque Mn [Nm]	Rated Power Pn [kW]	Rated Current In [Arms]	Rated Speed Nn [rpm]	Peak Torque Mp [Nm]	Peak Power Pp [kW]	Peak Current Ip [Arms]	Max Speed Nmax [rpm]	Max Mechanical Speed Nmax* [rpm]	Ke [Vrms/ Krpm]
GVM310-250MW1-W	650	434	228	323	5010	1240	350	1022	7100	8000	119
GVM310-250NC2-W		537	177	246	3150	1430	331	814	5200		162
GVM310-250MW2-W		479	199	278	3960	1430	409	1001	6400		132

Figure 4.1 Specifications of the selected Electric Motor from Parker Corporation's GVM series

Taken from Parker Hannifin Corporation (2022)

Upon reviewing the data sheet for the EM series, the model GVM310-250MW2-W stands out as the optimal choice for fulfilling the power requirements, boasting a peak power capacity of 409 kW, thereby satisfying the specified condition. With this EM model selected, we can establish the battery voltage, which should be equivalent to the voltage across the system's DC bus, recorded at 650 V. This correspondence leads to the specification of the DC bus as presented in Equation 4.10:

$$V_{DC} = V_{bat} = 650\ V, \quad P_{peak} = 409\ KW, \quad I_{peak} = 1001\ A \tag{4.10}$$

4.1.3 Specifications of the Battery Pack

Having established the voltage of the DC bus and consequently the battery pack voltage, we now proceed on the battery pack sizing process. Initially, it is critical to determine the minimum current requirement from the battery pack. This calculation is expressed in Equation 4.1.3:

$$P = V \times I \tag{4.11}$$

where P represents ESS_P at 337 KW, V stands for the DC bus voltage V_{DC_BUS} at 650 V, and thus I, the battery current I_bat, is calculated to be 520 A as a minimum value.

Continuing with the sizing of the battery pack, we adopt two methodologies: the first approach is grounded in defining the minimum battery capacity, ensuring stable recharging throughout the vehicle's operation period. The second approach focuses on determining the minimum required current, which guarantees that the battery pack can reliably support the system during periods of high dynamic demand.

The investigation will commence by examining the battery cell specifications as outlined in Figure 4.2. From this foundation, we will proceed to evaluate the system operation when sized on the basis of the minimum required capacity.

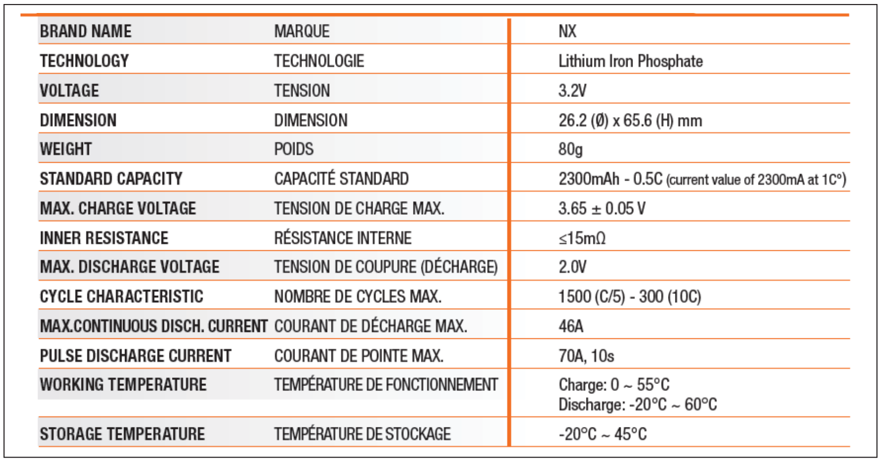

BRAND NAME	MARQUE	NX
TECHNOLOGY	TECHNOLOGIE	Lithium Iron Phosphate
VOLTAGE	TENSION	3.2V
DIMENSION	DIMENSION	26.2 (Ø) x 65.6 (H) mm
WEIGHT	POIDS	80g
STANDARD CAPACITY	CAPACITÉ STANDARD	2300mAh - 0.5C (current value of 2300mA at 1C°)
MAX. CHARGE VOLTAGE	TENSION DE CHARGE MAX.	3.65 ± 0.05 V
INNER RESISTANCE	RÉSISTANCE INTERNE	≤15mΩ
MAX. DISCHARGE VOLTAGE	TENSION DE COUPURE (DÉCHARGE)	2.0V
CYCLE CHARACTERISTIC	NOMBRE DE CYCLES MAX.	1500 (C/5) - 300 (10C)
MAX.CONTINUOUS DISCH. CURRENT	COURANT DE DÉCHARGE MAX.	46A
PULSE DISCHARGE CURRENT	COURANT DE POINTE MAX.	70A, 10s
WORKING TEMPERATURE	TEMPÉRATURE DE FONCTIONNEMENT	Charge: 0 ~ 55°C Discharge: -20°C ~ 60°C
STORAGE TEMPERATURE	TEMPÉRATURE DE STOCKAGE	-20°C ~ 45°C

Figure 4.2 Specifications of the battery cell, providing essential data for system sizing based on minimum capacity and current requirements

Taken from Enix Energies (2014)

The necessary battery capacity for our system is derived using Equation 4.12:

$$\text{Requested Capacity} = \text{Running Time (h)} \times \text{EM rated current} \tag{4.12}$$

Given the adoption of the NEDC speed profile for our simulations, which entails a duration of 1.2×10^3 seconds, and referencing the EM rated current of 278 A as indicated in Figure 4.1, the requisite battery capacity is calculated as follows:

$$\text{Required Ah (Capacity)} = \frac{1.2 \times 10^3 \times 278}{3600} = 92.66 \text{ Ah} \tag{4.13}$$

For ease of calculation and system design considerations, we round up the Required Capacity to 100 Ah.

Referencing the battery cell specifications detailed in Figure 4.2, each cell is noted to have a capacity of 2.3 Ah. To meet the system's capacity requirements, the calculation below determines the necessity for 44 cells to be configured in parallel:

$$\frac{100}{2.3} = 43.48 \approx 44 \tag{4.14}$$

With 44 cells in parallel, and given each cell's current capacity is 46 A, the module's total current capability is calculated as:

$$I_{module} = 46A \times 44 = 2024\ A \tag{4.15}$$

This calculation reveals that the battery pack's current capability significantly exceeds the EM's peak current tolerance of 1001 A, as shown in Figure 4.1.

The surplus in the EM's capacity to handle the maximum current not only deems it unnecessary for the battery to support such high currents but also indicates the system's capability to operate solely on batteries at an SOC higher than 0.4—considered unneeded given the FC serves as the primary energy source, recharging the battery as needed. With an FLC based EMS, maintaining the SOC within a range of 0.4 to 0.7 is achievable. Thus, sizing the battery to accommodate to the EM's peak current demand of 1001 A is considered sufficient.

Reducing the number of cells in parallel by half results in a configuration of 22 cells, providing a current output of $1012A$. This adjustment shifts the focus to sizing the system based on voltage requirements. According to Equation 4.10, the battery voltage V_{bat} must be at least 650 V. Therefore, the battery pack configuration must be restructured to fulfill both current and voltage demands:

$$\text{Cell voltage} = 3.2\ V \tag{4.16}$$

When 47 cells are arranged in series, the module voltage is calculated as:

$$\text{Module voltage} = 47 \times 3.2 = 150.4\ V \tag{4.17}$$

Subsequently, aligning 5 such modules in series achieves:

$$5 \times 150.4\,V = 752\,V \tag{4.18}$$

This arrangement shows that in order to maximize the physical dimensions of the module, 47 cells were first connected in series. This was followed by the series connection of 5 modules in order to exceed the voltage requirement of the system. A modest degree of oversizing ensures a margin of safety.

A battery pack with this arrangement weighs 413.6 kg. On the other hand, if the original configuration—which was designed to meet capacity requirements—had been followed, the weight of the battery pack would have doubled to 827.2 kg. This method dramatically cuts the weight of the battery pack in half by applying an EMS based on FLC, proving the effectiveness of strategic EMS application.

4.1.4 Specifications of the Fuel Cell & Hydrogen Consumption Calculation

With the battery sizing complete, attention now shifts to finalizing the ESS dimensions by determining the FC size and, crucially, the hydrogen tank capacity. For this project, the FC selection is inspired by the IEEE VTS Motor Vehicles Challenge 2020 Solano (2012), wherein the FC chosen for their prototype is suited to heavy-duty applications and is modeled based on a polarization curve—mirroring the approach taken in this study. Figure 4.3 details the specifications of the FC model incorporated into this project.

Consequently, the final aspect of component sizing concerns the capacity of the hydrogen tank. The type of FC under study operates on gaseous hydrogen, for which the storage requirements are dictated by the ideal gas law, presented as follows in Equation 4.19:

$$V(m^3) = \frac{n(mol) \times R(J/molK) \times T(K)}{P(Pa)} \tag{4.19}$$

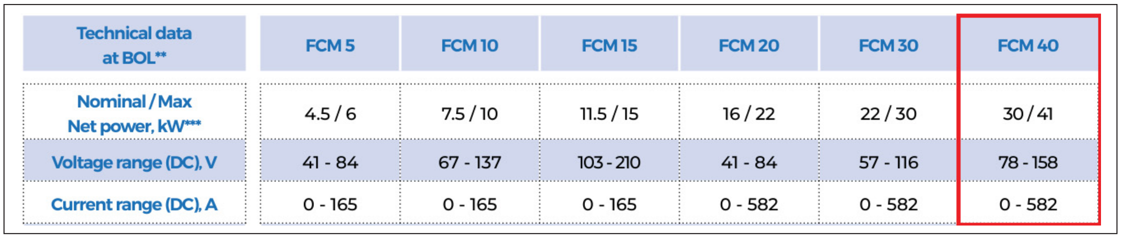

Technical data at BOL**	FCM 5	FCM 10	FCM 15	FCM 20	FCM 30	FCM 40
Nominal / Max Net power, kW***	4.5 / 6	7.5 / 10	11.5 / 15	16 / 22	22 / 30	30 / 41
Voltage range (DC), V	41 - 84	67 - 137	103 - 210	41 - 84	57 - 116	78 - 158
Current range (DC), A	0 - 165	0 - 165	0 - 165	0 - 582	0 - 582	0 - 582

Figure 4.3 Specifications of the fuel cell model used in this project, reflecting the standards of heavy-duty applications

Taken from Helion Hydrogen Power (2023)

In this equation, V denotes the volume of hydrogen gas required in cubic meters, n is the amount of substance in moles, R is the ideal gas constant with a value of 8.314 $J/mol \cdot K$, T represents the absolute temperature in Kelvin, and P stands for the pressure in Pascals. Utilizing this law, we can determine the necessary volume of hydrogen to be stored in the tank.

With the system's required energy calculated at 1120 KWh as shown in Equation 4.5, and considering the fuel cell's FC efficiency of 0.57, the needed hydrogen in the tank can be estimated as Equation 4.20:

$$\text{Required } H_2 \text{ in the Tank} = \frac{E_{req}}{FC_{eff}} = \frac{1120\ KWh}{0.57} \approx 1965\ KWh \tag{4.20}$$

From this energy requirement and knowing the energy density of hydrogen, we can deduce the mass of hydrogen necessary for the tank:

$$H_{2\_M_{Tank}} = \frac{H_{2\_E_{Tank}}}{H_{2\_Density}} = \frac{1965\ KWh}{33.333\ KWh/Kg} \approx 59\ Kg \tag{4.21}$$

This calculation informs us that approximately 59 Kg of hydrogen is needed to satisfy the system's energy demands.

Given the mass of hydrogen required for the tank is 59 Kg and the molar mass of hydrogen (H_{2_Molar}) is 2.016×10^{-3} $Kg/Mole$, the number of moles (n) can be calculated as:

$$n = \frac{H_{2\_M_{Tank}}}{H_{2\_M_{Molar}}} = \frac{59}{2.016 \times 10^{-3}} \approx 29265.87302 \text{ moles} \tag{4.22}$$

With the molar gas constant (R) being 8.314472 $\frac{J}{moleK}$, and the temperature (T) of the stored gas at $25°C$ or $298.15\ K$, and considering the high pressure of hydrogen storage tanks typically at $700\ Bar$ or $70,000,000\ Pa$, the volume of hydrogen (V) can be deduced using the ideal gas law:

$$V = \frac{n \times R \times T}{P} = \frac{29265.87302 \times 8.314472 \times 298.15}{70000000} \times 10^3 \approx 1036.4131\ L \approx V \approx 1035\ L \tag{4.23}$$

Equation 4.23 concludes that approximately 1035 L of hydrogen is required to be stored in the tank under the specified conditions.

4.2 Traction Subsystem Validation

The validation of the Traction Subsystem focuses on the correlation between the vehicle's actual speed and its reference value within the MATLAB/Simulink environment. Following the framework outlined in Chapter 1, the EMR features three distinct layers. The initial layer, depicted in orange and green, consists of the EMR model of the system's components, including the EM, Gearbox, Wheels, and Chassis, and outlines the system's constraints, namely the Battery, Brakes, and the Environment.

Progressing to the intermediary layer, shown in light blue, we encounter the IBC, which manages the local control employing a PI controller for speed regulation. The bottom layer, depicted in dark blue, is the Strategy level. This level is responsible for the allocation of energy distribution between mechanical braking and regenerative braking, optimizing the energy flow within the system.

Figure 4.4 presents the schematics of the Traction Subsystem utilizing the EMR, illustrating the subsystem's dynamics and control strategy integration. To continue our analysis in this section, we will examine the plot through designated scopes, each marked by distinct colors for clarity. The scope outlined in red highlights the battery current, the orange-marked scope focuses on battery power, the green scope illustrates battery energy, and the blue one represents the braking distribution coefficient.

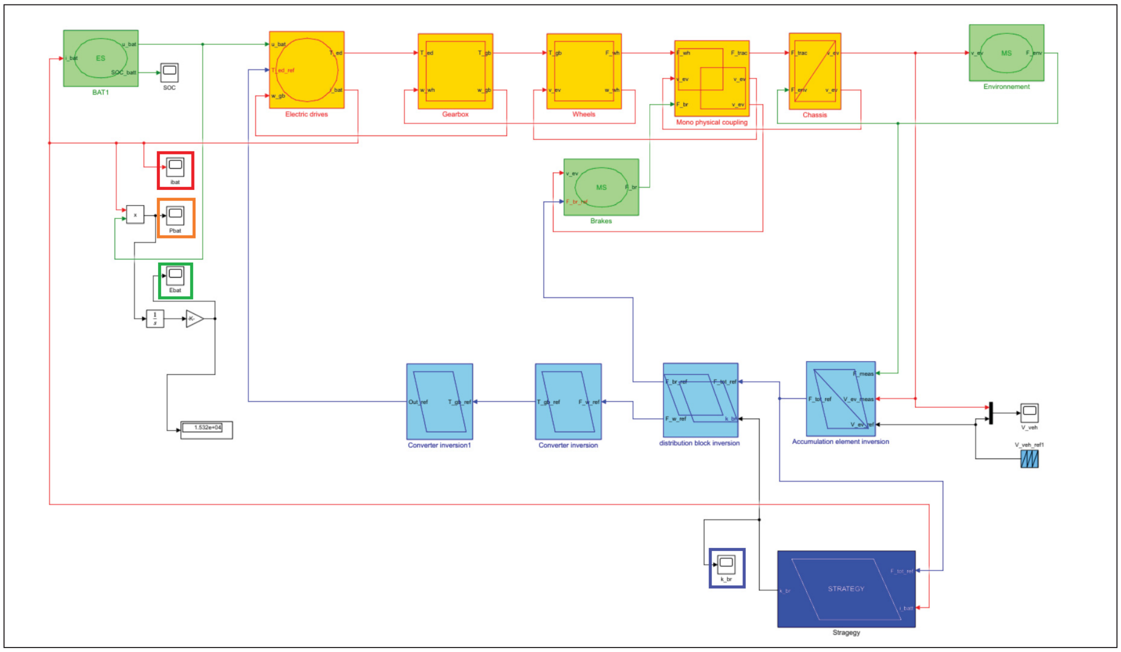

Figure 4.4 Schematic representation of the traction subsystem using Energetic Macroscopic Representation in MATLAB/Simulink, displaying system components and control layers for validating vehicle speed performance against reference values

The initial phase in the validation of the traction subsystem involves verifying the proper functionality of the PI controller. To accomplish this, the TS is isolated immediately post-controller as shown in yellow rectangle in Figure 4.5 where illustrates the methodology for this assessment. A detailed examination of Figure 4.6 reveals that the measured traction force $F_{trac\_measured}$ is in accordance with the reference traction force $F_{trac\_reference}$, confirming the effective operation of the PI controller. However, a minute lag can be observed when closely inspecting the force values, indicating a slight delay in the measured force's response to the reference. This small difference is considered acceptable and is not anticipated to significantly obstruct the system's main objective of reaching the desired speed.

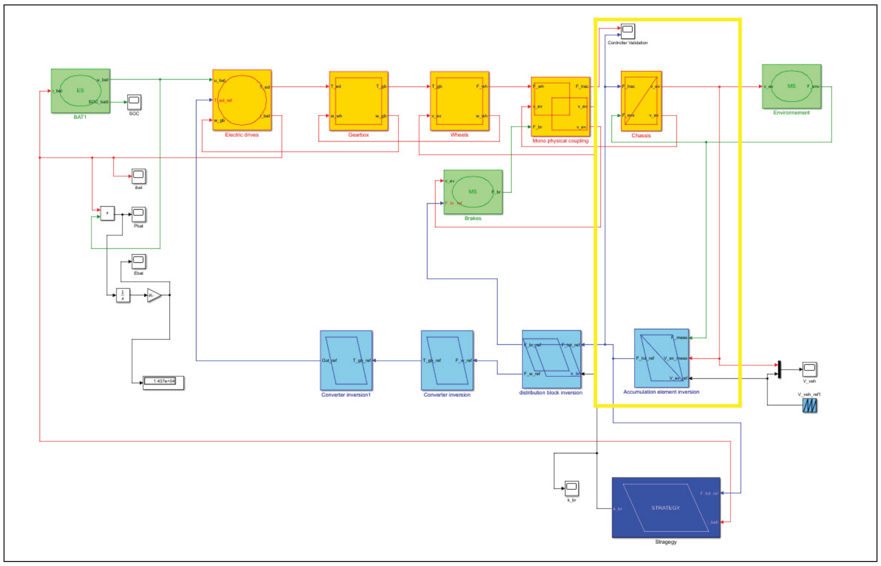

Figure 4.5 Diagram showcasing the method of isolating the traction subsystem post-PI controller to evaluate its performance in MATLAB/Simulink

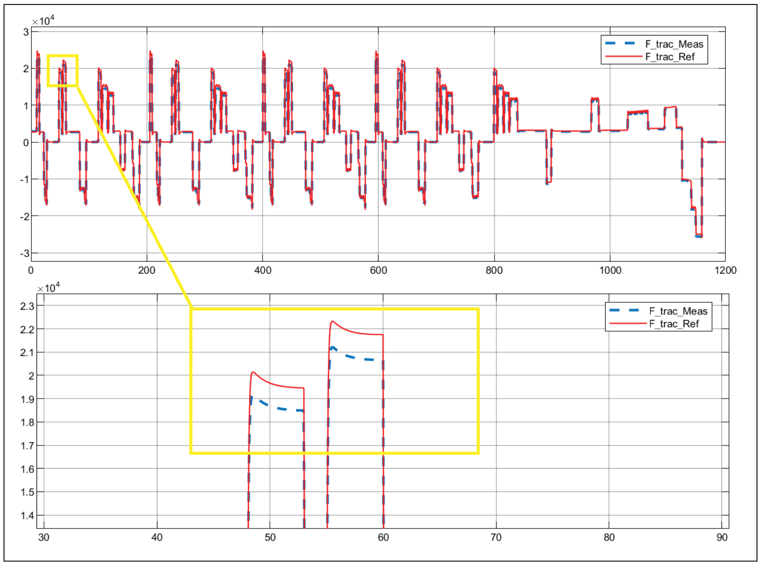

Figure 4.6 Comparison of the measured traction force versus the reference traction force, indicating the PI controller's response and slight temporal delay

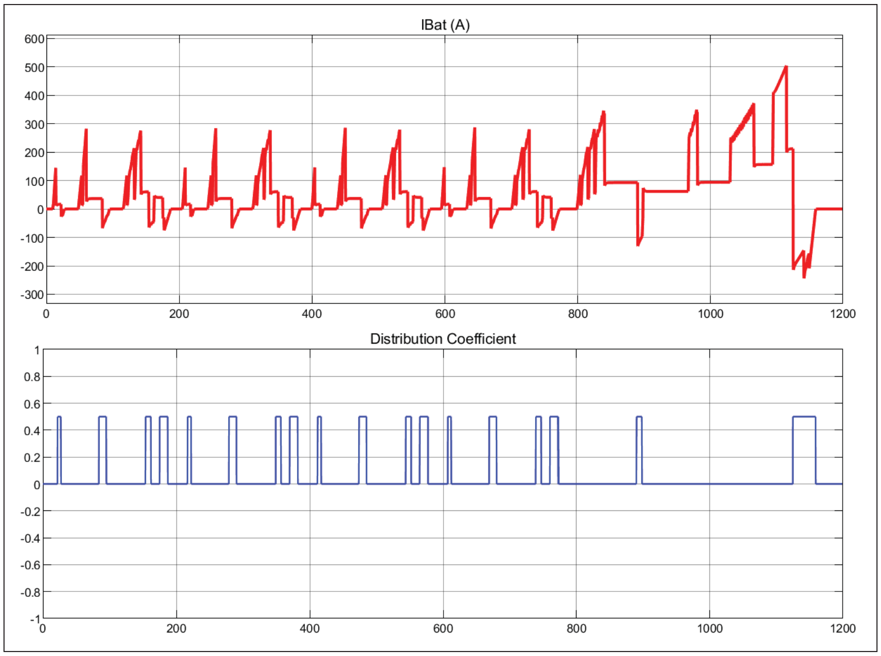

Figure 4.7 The correlation between braking distribution coefficient and battery current demonstrates the successful operation of the regenerative braking strategy

To determine the effectiveness of the implemented braking strategy, we refer to the diagnostic scopes indicated in Figure 4.4. The red-marked scope tracks the battery current, while the blue-marked scope monitors the variations in the braking distribution coefficient, providing insight into the system's dynamic braking response. Examining the braking distribution coefficient plot alongside the battery current plot in Figure 4.7 clearly demonstrates the effectiveness of our braking strategy. When we see that the battery current dips below zero, this indicates that regenerative braking is taking place and the battery is being charged. The battery current plot consistently aligns with the changes in the braking distribution coefficient, confirming that the system switches to regenerative braking as intended. Therefore, it is clear that the braking strategy is functioning correctly, as evidenced by the battery charging whenever the braking distribution coefficient signals regenerative braking.

To validate the system's operation, it is essential to verify that the battery power mirrors the trend of the battery current. Subsequently, the battery energy must be observed to ensure its precise

Figure 4.8 Correlation between battery power and current, validating the battery's consistent or ascending energy levels in accordance with the non-plug-in hybrid vehicle design

functionality. In line with the design criteria, since the vehicle is intended to be non-plug-in hybrid, the battery energy should consistently exhibit a steady or increasing trend without any decrement. Figure 4.8 confirms that the battery's power indeed closely aligns with the current's behavior, satisfying one of the validation objectives. Furthermore, the illustration shows the battery's energy remains constant or increases, aligning with the project's goals and confirming the absence of energy depletion, which is crucial for a non-plug-in system.

The final phase of validation includes examining whether the vehicle's measured speed adheres to its reference speed. This validation confirms that the PI controller designed for speed control

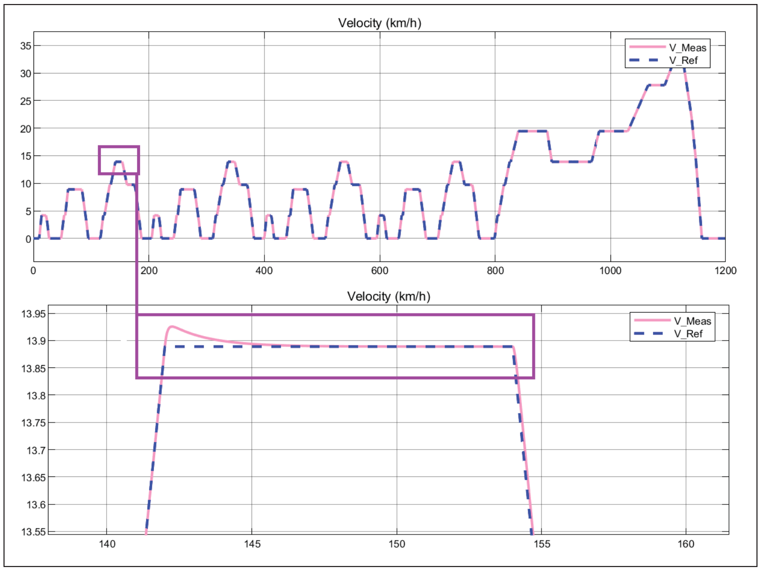

Figure 4.9 Comparative analysis of the vehicle's measured speed against the reference speed, highlighting the negligible difference between the two

functions correctly, as discussed in Chapter 2. The operational mechanics of the PI controller are explained by Equation 2.2. The expectation is that the measured vehicle speed aligns with the reference speed. Figure 4.9 depicts both variables on a single plot, where it becomes evident that the measured and reference speeds are closely aligned. Upon closer inspection, a minor discrepancy may be discernible, yet it remains negligible.

4.3 Energy Storage Subsystem Validation

In the validation of the ESS, the primary goals include verifying the proper functioning of the PI controller dedicated to FC current regulation and confirming that the FC activates and operates as expected. The implications of the Strategy layer on system performance are addressed in a subsequent section of this chapter.

Figure 4.10 depicts the system's final schematic and configuration, showcasing the integration of both energy sources—the FC and the battery pack—prior to the application of the Strategy layer. Within this setup, i_{fc_ref} is presumed to be a constant value of 260 A. This assumption simplifies the preliminary validation process, allowing for a focused evaluation of the PI controller's effectiveness and the FC's operational integrity. The determination of i_{fc_ref} will be refined by the EMS within the Strategy layer in later stages.

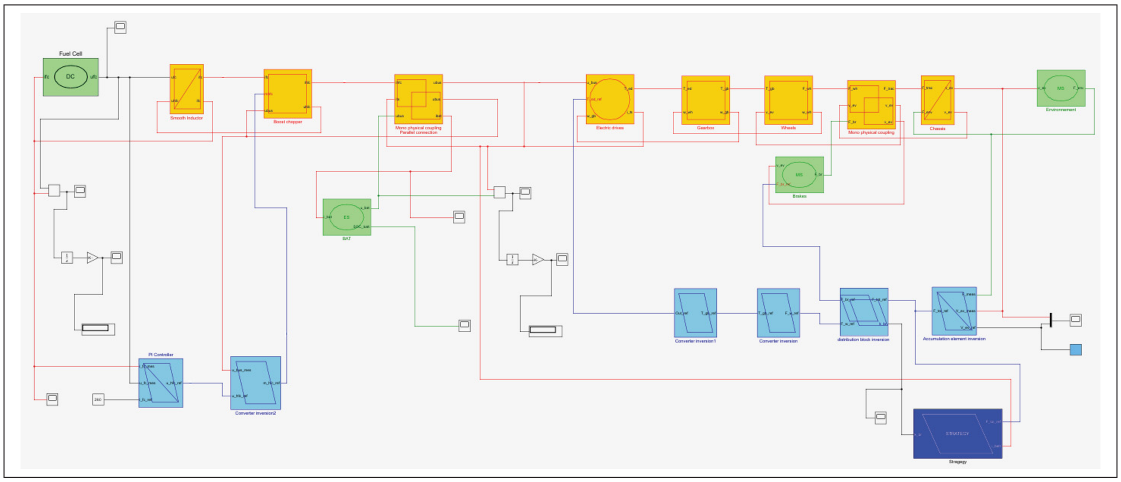

Figure 4.10 Schematic representation of the ESS featuring the FC and battery pack without the Strategy layer, employing a constant i_{fc_ref} for initial validation of the PI controller and FC functionality

To evaluate the PI controller's performance, it is essential to observe the plot within the controller scope, showcasing both i_{fc_meas} and i_{fc_ref} for comparative analysis. Figure 4.11 illustrates the behavior of these variables during the simulation. A notable feature in the FC configuration is the inclusion of a switch mechanism. This switch ensures that the fuel cell outputs essentially zero voltage, particularly when $i_{\text{fcref\_real}}$ approaches a negligible value 0.001 A, effectively simulating the FC's inactive state. Such a configuration aids in replicating periods where the fuel cell should not be active.

Furthermore, it is observed that i_{fc_ref} takes approximately 40 seconds to stabilize at its target of 260 A. This delay is not indicative of any deficiency in the controller's functionality but rather a consequence of a rate limiter placed before the PI controller in the system's configuration. This design decision, coupled with the implementation of a low-frequency filter at 15 mHz and a ramp rate limit varying between 6 to 20 A/sec for i_{fc_ref}, is strategically aimed at safeguarding

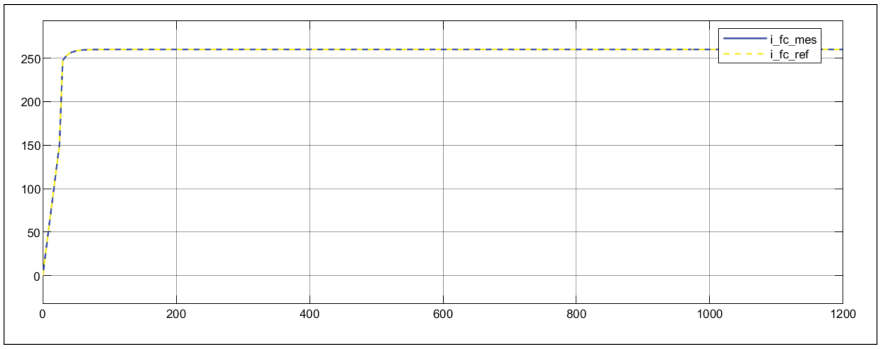

Figure 4.11 Simulation behavior of i_{fc_meas} and i_{fc_ref} within the PI controller scope, highlighting the FC's operational dynamics and the implemented control strategies for lifespan enhancement

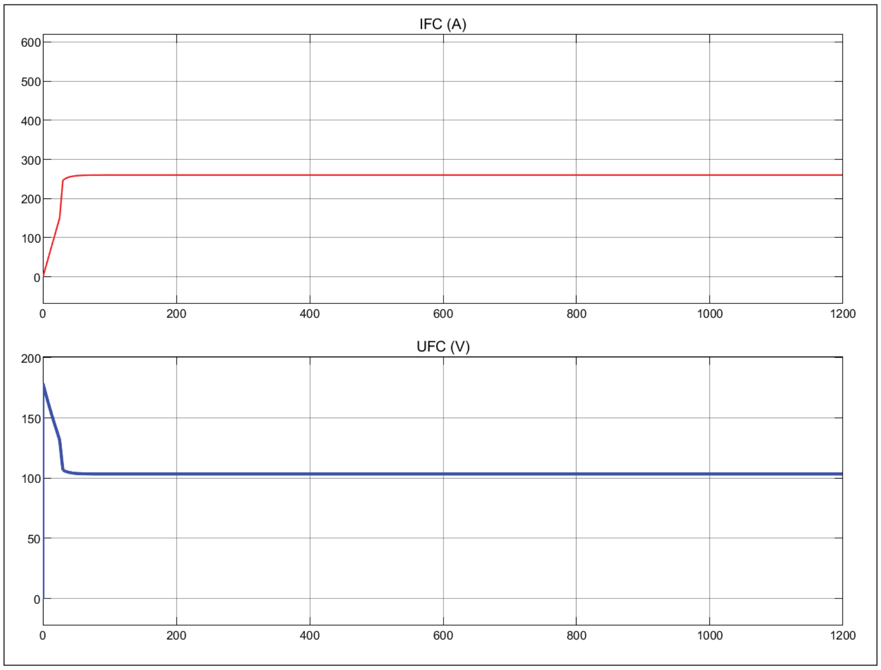

Figure 4.12 Comparative analysis of the FC's output voltage and current, demonstrating activation thresholds and the impact of rate limiting on reaching operational current levels

against stack faults and extending the fuel cell's operational lifespan, as elaborated in prior discussions and reinforced by literature Depature *et al.* (2016).

To assess the functionality of the FC, it is crucial to analyze and compare the FC's output voltage against its current. Figure 4.12 presents these metrics in separate plots. The integration of a switch within the FC configuration results in a zero output voltage whenever the FC current is at zero. As the FC current surpasses the switch threshold of 0.001, the FC becomes operational. The fluctuations observed in the FC's output voltage correspond to the FC's polarization curve, illustrating the dynamic response of the FC to varying current levels. The delay observed in the FC current reaching its designated final value is attributed to the rate limiter, a control mechanism designed to modulate the current's rate of change to ensure stable FC operation.

4.4 Analysis of System Performance Across Different Scenarios

The aim of this study is to evaluate the system's operation across three distinct scenarios, each differing in efficiency levels.

- The first scenario explores the system functioning solely on the battery pack, essentially operating as a BEV without integrating an FC.
- In the second scenario, the incorporation of the FC is examined, highlighting its importance in heavy-duty applications and this project in particular. Here, the EMS employs a basic rule-based strategy.
- The third scenario involves a simulation of the system converted into an FCEV, utilizing an FLC-based EMS. This setup demonstrates superior efficiency, ensuring the longevity of the battery pack while minimizing hydrogen consumption.

These scenarios play a crucial role in demonstrating the adaptability of the system and the need of an efficient EMS in maximizing efficiency and resource use.

The evaluation of these three scenarios is anchored on the SOC of the battery, aligning with the primary aim to enhance battery pack longevity by maintaining its SOC within the range of 0.4 to 0.7.

In the first scenario, where the system operates exclusively on battery power, the battery's SOC dips to 0.26, as depicted in Figure 4.13. This outcome not only underscores the infeasibility of relying solely on the battery for energy but also indicates that a battery pack weighing 413.6 Kg is insufficient for sustaining vehicle operation without degrading its own condition.

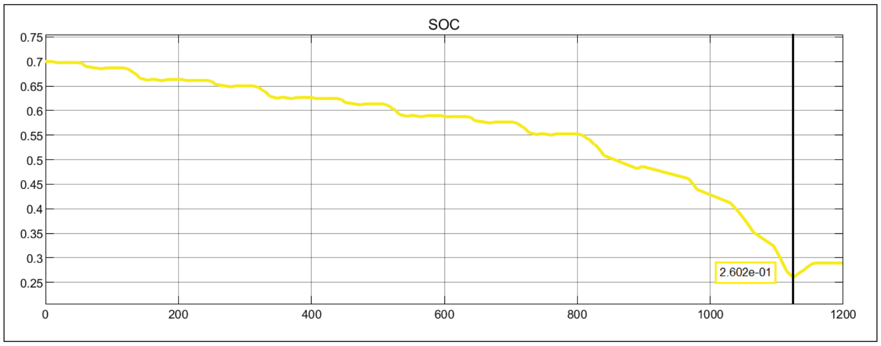

Figure 4.13 Battery SOC trajectory when the vehicle operates solely on the battery pack, highlighting the decline to a SOC of 0.26

Should the FC be asked to continually operate in support of the SOC, instances occur where the SOC surpasses the upper threshold of 0.7. Under this scenario, the SOC will periodically surpass its assigned limit; Figure 4.14 describes this event.

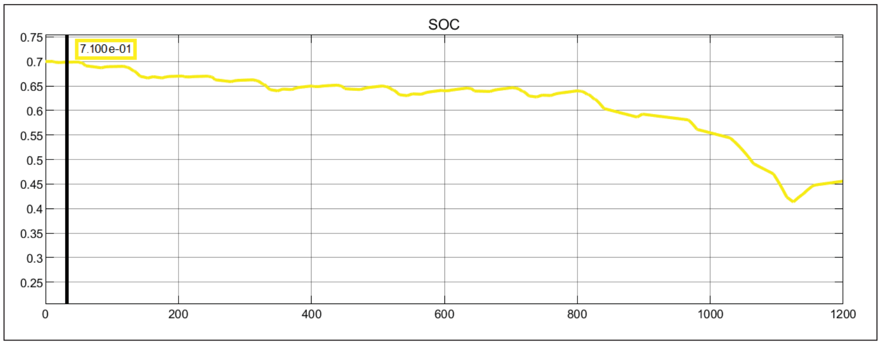

Figure 4.14 Illustration of SOC exceeding the upper limit of 0.7 when the fuel cell operates continuously, highlighting instances where SOC surpasses the desired range

To explore the second scenario, it's imperative to integrate the foundational layer of the ESS configuration, known as the strategy level. Within this scenario, the strategy block features the EMS, which is configured to function according to a basic rule-based EMS approach. Figure 4.15 presents the complete EMR of the analyzed FCEV, including the strategy layer.

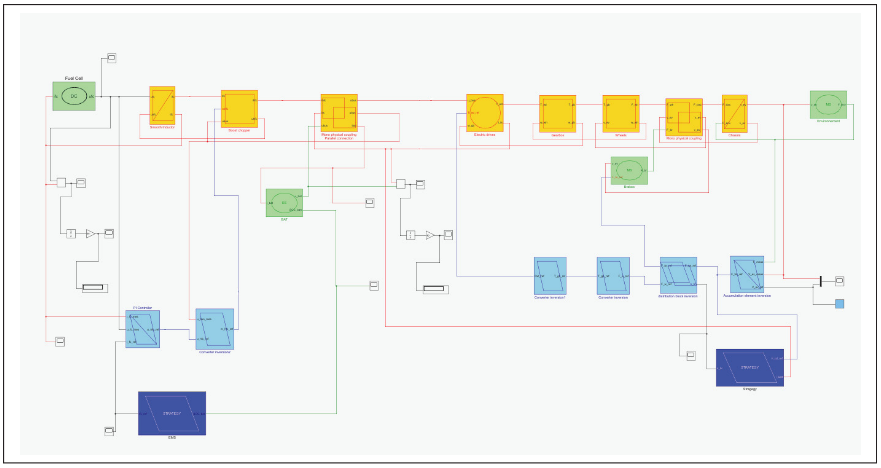

Figure 4.15 Comprehensive EMR of the FCEV under study

Operating with a basic rule-based EMS allows the system to function, yet the SOC remains unsatisfactory, approximately at 0.27, marking an improvement over the first scenario, but only marginally. Figure 4.16 illustrates the battery SOC under conditions where the system employs a simple rule-based strategy for energy management.

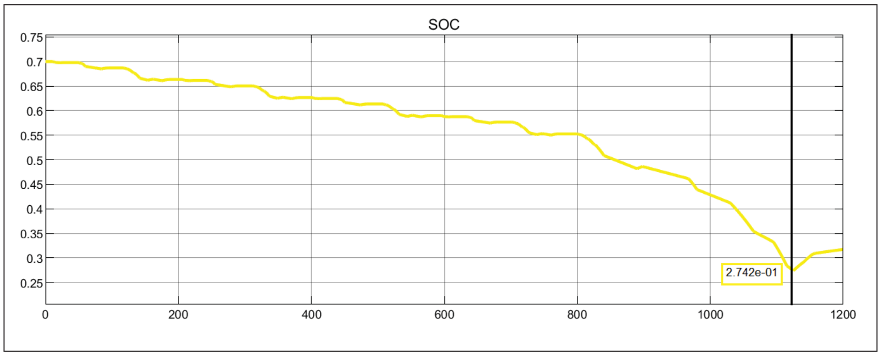

Figure 4.16 Battery SOC during operation with a simple rule-based EMS, indicating a slight improvement in SOC to approximately 0.27

Transitioning to the final scenario, the system operates under an EMS governed by FLC rules. Figure 4.17 demonstrates that employing the FLC approach for the EMS effectively maintains the battery's SOC within the desired range of 0.4 to 0.7. This strategic management ensures the longevity of the battery pack.

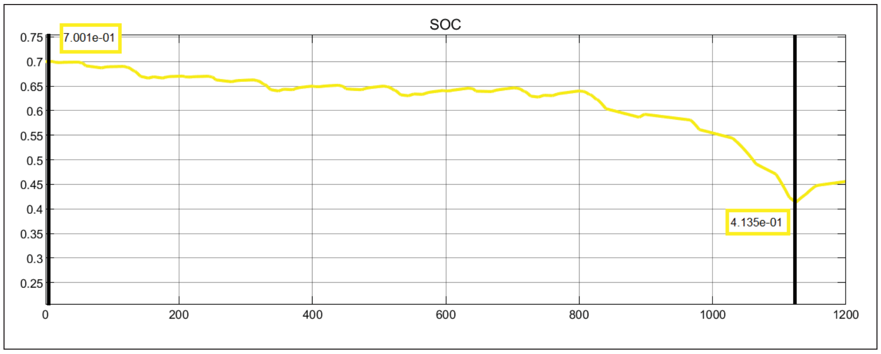

Figure 4.17 The battery SOC under an FLC rule-based EMS, illustrating successful maintenance within the optimal range for battery longevity

4.5 Conclusion on Data Acquisition

The system's top-down objectives are reviewed in this section. Maintaining the SOC in the ideal range of 0.4 to 0.7 is of the utmost importance for the battery pack's lifetime. The second goal is to reduce the amount of hydrogen used, which is essential to improving the sustainability and efficiency of the system. Last but not least, reducing the weight of the vehicle—especially by reducing the mass of the battery pack—is an important factor in the design and functionality of the system.

In Figure 4.17, we demonstrate that employing an FLC-based EMS enables the maintenance of the battery's SOC within the desired range of 0.4 to 0.7. This achievement fulfills the system's primary objective, underscoring the effectiveness of the FLC-based EMS.

Furthermore, as detailed in the preceding section 4.1.3, the decision to prioritize current requirements over capacity in battery pack sizing was strategic. Such an approach is validated by the observation that the battery pack's current provision far surpasses the EM peak current capacity of 1001 A. This excess capacity suggests that relying solely on the battery for high currents is inefficient, especially considering the FC as the main energy source capable of recharging the battery as necessary. Hence, the system's design to operate efficiently on a battery sized for the EM's peak current demand is justified. By halving the number of cells in parallel to 22, we achieve a current output of 1012 A, aligning closely with the system's operational requirements. This configuration not only meets the necessary power demands but also optimizes the system's weight and efficiency, reinforcing the utility of an FLC-based EMS in achieving optimal system performance.

This leaves us with the final objective of minimizing hydrogen consumption. As elaborated on in section 4.1.4, the hydrogen tank sizing was predicated on a worst-case scenario—operating the motor at peak power for 3.5 hours. This led to the calculation of the required hydrogen in the tank, presented as Equation 4.20, amounting to 1965 KWh. Implementing an FLC-based EMS presents an opportunity to diminish the energy demands on the tank. To facilitate this comparison, it is essential to analyze the energy contributions from both the Battery and the FC within the system, as simulated in Simulink. According to Figure 4.18, the observed energy values are as follows:

- $E_{bat} = 15.32\ KWh$
- $E_{FC} = 6.814\ KWh$

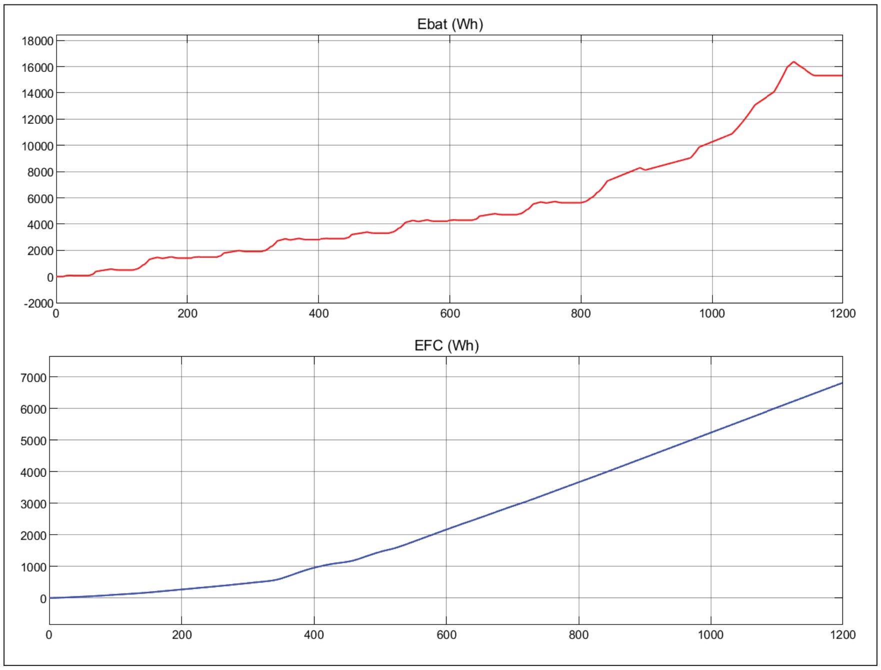

Figure 4.18 Energy contributions from the Battery and Fuel Cell within the system, showcasing $E_{bat} = 15.32\ KWh$ and $E_{FC} = 6.814\ KWh$

However, the values for E_{bat} and E_{FC} correspond to the NEDC speed profile, which does not consistently demand maximum power from the vehicle and operates over a limited duration of 1200 seconds. To align these observed values with those derived from the worst-case scenario calculations, a process of adaptation is required, ensuring that the comparison accurately reflects the system's performance under maximal stress conditions.

To correlate the observed values with those from the worst-case scenario, we begin by recalculating E_{bat} and E_{FC} over the desired operation time of 3.5 hours:

$$E_{bat\_total} = 15.32 \times 3 \times 3.5 = 160.86 \text{ KWh} \tag{4.24}$$

$$E_{FC\_total} = 6.814 \times 3 \times 3.5 = 71.54 \text{ KWh} \tag{4.25}$$

Therefore, the total energy request from the ESS becomes:

$$E_{ESS\_total} = 160.86 + 71.54 = 232.407 \text{ KWh} \tag{4.26}$$

Comparing this total observed energy request E_{ESS_total} to the calculated value for the worst-case scenario of 1120 KWh, as specified in Equation 4.8, indicates that the energy demand under observed conditions is 4.82 times lower than that of the worst-case scenario. This factor of 4.82 serves as a coefficient to adjust observed energy consumption to align with the most demanding operational expectations.

To establish a comparison between the observed E_{FC_total} and the worst-case scenario estimates, the observed total fuel cell energy needs adjustment by a factor of 4.82:

$$E_{FC\_total\_wc} = 71.547 \times 4.82 = 344.85 \text{ KWh} \tag{4.27}$$

Recall from Equation 4.20 that the required hydrogen in the tank for the worst-case scenario was calculated to be 1965 KWh. Comparing this requirement to the adjusted $E_{FC\_total\_wc}$, we find that the energy demand from the FC under a worst-case scenario, facilitated by an FLC-based EMS, is approximately 5.7 times less than initially anticipated. This indicates that adopting an FLC-based EMS configuration can reduce hydrogen consumption by a factor of 5.7, necessitating only 181.58 L of hydrogen compared to the 1035 L projected in Equation 4.23. This analysis satisfactorily addresses all three system objectives, illustrating the system's adeptness at meeting its goals through the implementation of an FLC-based EMS.

CONCLUSION AND RECOMMENDATIONS

This study started a critical path toward resolving the urgent problem of CO_2 emissions worldwide, particularly emphasizing the transportation sector's contribution, which stands at approximately 20% of the total emissions. With road transport being identified by the International Energy Agency as the major contributor within this sector, accounting for 75% of transportation emissions, the need for sustainable alternatives has never been more critical. This thesis presented a transformative approach by converting a conventional Class 8 C10 Caterpillar Kenworth 2002 truck into an FCEV, thus aligning with the Massachusetts Institute of Technology's insights into the potential of FCEVs in significantly reducing greenhouse gas emissions and mitigating petroleum dependency.

Employing MATLAB/Simulink alongside an EMR, the study intricately designed and simulated a comprehensive EMS tested across multiple scenarios. The deployment of an FLC based EMS was pivotal in achieving the system's objectives, which include maintaining the battery's SOC within an optimal range of 0.4 to 0.7, minimizing hydrogen consumption, and reducing the vehicle's overall weight.

Key findings from the study reveal that an FLC-based EMS effectively keeps the battery's SOC within the desired range, thereby ensuring the battery pack's longevity. Additionally, the strategic prioritization of current requirements over capacity in battery pack sizing, demonstrated by the observation that the battery pack's current supply significantly exceeds the EM peak current capacity of 1001 A, underlines the efficiency of relying on the FC as the primary energy source. This approach not only meets the system's power demands but also optimizes weight and operational efficiency, showcasing an FLC-based EMS's role in achieving optimal system performance.

The hydrogen consumption analysis further underscores the EMS's efficacy. By adopting an FLC-based EMS, the study demonstrates a potential reduction in hydrogen consumption by approximately 5.7 times without adding to the battery pack weight, highlighting the system's sustainability and environmental benefits. This adjustment meant that the hydrogen consumption could be dramatically decreased only through specific designed FLC-based EMS, requiring only 181.58 *L* of hydrogen compared to the 1035 *L* initially projected. Such an achievement significantly contributes to the overarching goal of reducing the environmental footprint of heavy-duty transportation.

Building on the insights gained, the following recommendations to enhance the system's functionality are proposed:

1. **Integration of Artificial Intelligence (AI) in EMS Tuning:** Expanding the system's adaptability through AI can facilitate the tuning process of the FLC and FIS, enabling efficient operation across a broader range of driving cycles without the need for manual adjustments.

2. **Optimization of Fuel Cell Operation Cycles:** A focused analysis on minimizing the fuel cell's activation and deactivation cycles can enhance its lifespan, creating a more sustainable and cost-effective energy solution for FCEVs.

This thesis established a foundational stone in the field of sustainable transportation, advocating for the accelerated adoption of FCEV technology in heavy-duty vehicles. Addressing the recommendations highlighted herein can propel further advancements in FCEV technology, paving the way for a greener, more sustainable future in transportation.

BIBLIOGRAPHY

(1965). *Gemini fuel cell system final report*.

Abdelkareem, M. A., Elsaid, K., Wilberforce, T., Kamil, M., Sayed, E. T. & Olabi, A. (2021). Environmental aspects of fuel cells: A review. *Science of The Total Environment*, 752, 141803.

Ajanovic, A. & Haas, R. (2019). Economic and environmental prospects for battery electric-and fuel cell vehicles: a review. *Fuel cells*, 19(5), 515–529.

Ajanovic, A. (2015). The future of electric vehicles: prospects and impediments. *Wiley Interdisciplinary Reviews: Energy and Environment*, 4(6), 521–536.

AspenCore,Inc., A. I. (Accessed 2023). The Inductor [Online]. Retrieved from: https://www.electronics-tutorials.ws/inductor/inductor.html.

Bawa, I., Omeiza, A. U. & Amlabu, C. A. (2019). Improving Performance and Prolongation of Electric Motors by Advanced Control Scheme in Nigeria Manufacturing Industry: An Issue to Sustain Production and Marketing of Industrial Products. *International Journal of Current Innovations in Advanced Research*, 51–59.

Blal, M., Benatiallah, A., NeÇaibia, A., Lachtar, S., Sahouane, N. & Belasri, A. (2019). Contribution and investigation to compare models parameters of (PEMFC), comprehensives review of fuel cell models and their degradation. *Energy*, 168, 182–199.

Bunzemeier, A. & Litz, L. FUNDAMENTALS OF CONTROL THEORY.

Camacho, M. d. l. N. (2022). Hydrogen fuel cell heavy-duty trucks: Review of main research topics. *International Journal of Hydrogen Energy*, 47, 29505–29525.

Cell, F. & Association, H. E. [Accessed on: September 23, 2024]. (2023). Fuel Cell and Hydrogen Energy Association. Retrieved from: https://www.fchea.org/fuelcells.

Chen, K., Bouscayrol, A. & Lhomme, W. (2008). Energetic Macroscopic Representation and Inversion-based Control Application to an Electric Vehicle with an Electrical Differential. *Journal of Asian Electric Vehicles*, 6(1), 1097–1102.

Chen, L. & Guan, W. (2021). Safety design and engineering solution of fuel cell powered ship in inland waterway of China. *World Electric Vehicle Journal*, 12(4), 202.

Chrenko, D. (2008). *Energetic macroscopic representation modeling and control of a low temperature fuel cell system fed by hydrocarbons*. (Ph.D. thesis, Université de Franche-Comté).

CTMS, C. (2023). Introduction: PID Controller Design [Online]. Retrieved from: https://ctms.engin.umich.edu/CTMS/index.php?example=Introduction&section=ControlPID#19.

Cullen, D. A., Neyerlin, K., Ahluwalia, R. K., Mukundan, R., More, K. L., Borup, R. L., Weber, A. Z., Myers, D. J. & Kusoglu, A. (2021). New roads and challenges for fuel cells in heavy-duty transportation. *Nature energy*, 6(5), 462–474.

Depature, C., Jemei, S., Boulon, L., Bouscayrol, A., Marx, N., Morando, S. & Castaings, A. (2016). Ieee vts motor vehicles challenge 2017-energy management of a fuel cell/battery vehicle. *2016 IEEE Vehicle Power and Propulsion Conference (VPPC)*, pp. 1–6.

Dezhou Sanhe Electric Co., D. S. E. C. (Jul-09-2023). THE ROLE OF INDUCTORS IN NEW ENERGY VEHICLES [Online]. Retrieved from: https://www.sanhetrans.com/news/introduction-to-the-role-of-new-energy-inductor-solutions-in-automobiles/.

Dincer, I., Hamut, H. S. & Javani, N. (2016). *Thermal management of electric vehicle battery systems*. John Wiley & Sons.

Douglas, B. [Fuzzy Logic]. (2021, August, 25). What Is Fuzzy Logic? [Youtube Video]. Retrieved from: https://www.youtube.com/watch?v=__0nZuG4sTw&ab_channel=MATLAB.

Eapen, D., Suseendiran, S. & Rengaswamy, R. (2016). Phosphoric acid fuel cells. In *Compendium of Hydrogen Energy* (pp. 57–70). Elsevier.

Electronics Coach, E. C. (2023). Control System [Online]. Retrieved from: https://electronicscoach.com/control-system.html.

Enix Energies, E. E. [26650 LIFEPO4 BATTERY 2300mAh 3.2V]. (2014) [Battery specification Data sheet].

European Commission Green propulsion in transport. Green propulsion in transport [Online]. Retrieved from: https://transport.ec.europa.eu/transport-themes/clean-transport/clean-and-energy-efficient-vehicles/green-propulsion-transport_en.

Fuel Cell & Hydrogen Energy Association, F. C. . H. E. A. (2021). History of Fuel Cells. Retrieved from: https://www.fchea.org/history.

Granovskii, M., Dincer, I. & Rosen, M. A. (2006). Economic and environmental comparison of conventional, hybrid, electric and hydrogen fuel cell vehicles. *Journal of Power Sources*, 159(2), 1186–1193.

Grove, W. R. (1839). On Voltaic Series and the Combination of Gases by Platinum. *Philosophical Magazine and Journal of Science*.

Haidekker, M. A. (2013). Solving differential equations in the Laplace domain, linear feedback controls. *Linear Feedback Controls: The Essentials, Elsevier, Burlington*, 27–56.

Hannah Ritchie, H. R. (2020). Cars, planes, trains: where do CO2 emissions from transport come from? [Online]. Retrieved from: https://ourworldindata.org/co2-emissions-from-transport.

Hart, D. & Hörmandinger, G. (1998). Environmental benefits of transport and stationary fuel cells. *Journal of Power Sources*, 71(1-2), 348–353.

Helion Hydrogen Power, H. H. P. (2023). HEAVY DUTY FUEL CELL PRODUCTS [Online dataset]. Retrieved from: https://www.helion-hydrogen-power.alstom.com/upload/documents/BR-helion-FICHE%20HEAVY%20DUTY%20FUEL%20CELL%20PRODUCTS-A4%20paysage[1].pdf.

Huangfu, Y., Yu, T., Zhuo, S., Shi, W. & Zhang, Z. (2021). An Optimization Energy Management Strategy Based on Dynamic Programming for Fuel Cell UAV. *IECON 2021–47th Annual Conference of the IEEE Industrial Electronics Society*, pp. 1–6.

Ijaodola, O., Ogungbemi, E., Khatib, F. N., Wilberforce, T., Ramadan, M., El Hassan, Z., Thompson, J. & Olabi, A. G. (2018). Evaluating the effect of metal bipolar plate coating on the performance of proton exchange membrane fuel cells. *Energies*, 11(11), 3203.

International Renewable Energy Laboratory, N. (2011). Hydrogen Fuel Cell Electric Vehicles [Online]. Retrieved from: https://www.nrel.gov/hydrogen/fuel-cell-vehicle-evaluation.html.

Ito, H. (2017). Economic and environmental assessment of phosphoric acid fuel cell-based combined heat and power system for an apartment complex. *International Journal of Hydrogen Energy*, 42(23), 15449–15463.

James, B. D. & Kalinoski, J. A. (2002). *Mass production cost estimation of direct hydrogen PEM fuel cell systems for transportation applications: 2002 update*.

John D, H. (2022). Proportional Integral (PI) Control [Online]. Retrieved from: https://apmonitor.com/pdc/index.php/Main/ProportionalIntegralControl.

Kamal, E. & Adouane, L. (2018). Hierarchical energy optimization strategy and its integrated reliable battery fault management for hybrid hydraulic-electric vehicle. *IEEE Transactions on Vehicular Technology*, 67(5), 3740–3754.

Keyu, C. (2010). *COMMON ENERGETIC MACROSCOPIC REPRESENTATION*. (Ph.D. thesis, Université Paris).

Koita, A., Payman, A., Dakyo, B. & Hissel, D. (2018). Control of a Wind Energy Conversion System using the Energetic Macroscopic Representation. *2018 7th International Conference on Renewable Energy Research and Applications (ICRERA)*, pp. 1460–1465.

Kromer, M. A. & Heywood, J. B. (2007). An assessment of fuel cells for zero-emission vehicles and their impact on oil use and CO2 emissions. *Energy Policy*, 35(9), 4693–4708.

Lathi, B. P. (2006). Linear systems and signals. *ISBN13: 9780195158335*.

Lenoir, T., Trovao, J. P. F., Ta, M. C. & Messier, P. Electric Powertrain Modeling and Control in Vehicular Applications using Energetic Macroscopic Representation.

Lhomme, W., Bouscayrol, A. & Barrade, P. (2004). Simulation of a series hybrid electric vehicle based on energetic macroscopic representation. *2004 IEEE International Symposium on Industrial Electronics*, 2, 1525–1530.

Liu, Y., Liu, J. & Qin, D. (2020). Online energy management strategy of fuel cell hybrid electric vehicles based on rule learning. *Journal of Cleaner Production*, 260, 121017-to.

Manish, K. S. (2021). Equivalent Circuit of a Transformer Explained with Examples [Online]. Retrieved from: https://www.tutorialspoint.com/equivalent-circuit-of-a-transformer-explained-with-examples.

Manoharan, Y., Hosseini, S. E., Butler, B., Alzhahrani, H., Senior, B. T. F., Ashuri, T. & Krohn, J. (2019). Hydrogen fuel cell vehicles; current status and future prospect. *Applied Sciences*, 9(11), 2296.

Mantravadi, P., Husain, I. & Sozer, Y. (2011). Modeling, implementation and analysis of a Li-ion battery powered electric truck. *2011 IEEE Energy Conversion Congress and Exposition*, pp. 1428–1435.

Mitra, U., Arya, A. & Gupta, S. (2023a). A comprehensive and comparative review on parameter estimation methods for modelling proton exchange membrane fuel cell. *Fuel*, 335, 127080.

Mitra, U., Arya, A., Khan, A., Javara, N., Gawre, S. K. & Arya, M. (2023b). Simulation and Performance Analysis of a Fuel Cell Hybrid Electric Vehicle. *2023 IEEE International Students' Conference on Electrical, Electronics and Computer Science (SCEECS)*, pp. 1–6.

Nikola Corporation, N. C. (2023). TRE FCEV ALL SCIENCE.NO FICTION. [Online]. Retrieved from: https://www.nikolamotor.com/tre-fcev/.

Noura, N. (2022a). *Une stratégie de gestion énergétique adaptative pour un véhicule hybride à hydrogène basée sur l'identification en ligne de paramètres*. (Ph.D. thesis, Université du Québec à Trois-Rivières).

Noura, N. (2022b). *Une stratégie de gestion énergétique adaptative pour un véhicule hybride à hydrogène basée sur l'identification en ligne de paramètres*. (Ph.D. thesis, UNIVERSITÉ DU QUÉBEC À TROIS-RIVIÈRES, https://depot-e.uqtr.ca/id/eprint/10380).

Nunez, C. (2019). Carbon dioxide levels are at a record high. Here's what you need to know. [Online]. Retrieved from: https://www.nationalgeographic.com/environment/article/greenhouse-gases.

Ogata, K. (1999). Modern control engineering. *Book Reviews*, 35(1181), 1184.

O'hayre, R., Cha, S.-W., Colella, W. & Prinz, F. B. (2016). *Fuel cell fundamentals*. John Wiley & Sons.

Ouddah, N. & Adouane, L. (2019). Hybrid energy management strategy based on fuzzy logic and optimal control for tri-actuated powertrain system. *IEEE Transactions on Vehicular Technology*, 68(6), 5343–5355.

Pardhi, S., Chakraborty, S. & Tran, D.-D. (2022). A Review of Fuel Cell Powertrains for Long-Haul Heavy-Duty Vehicles: Technology, Hydrogen, Energy and Thermal Management Solutions. *Energies*, 15(24), 9557-to.

Parikh, A., Shah, M. & Prajapati, M. (2023). Fuelling the sustainable future: a comparative analysis between battery electrical vehicles (BEV) and fuel cell electrical vehicles (FCEV). *Environmental Science and Pollution Research*, 30(20), 57236–57252.

Parker Hannifin Corporation, P. H. C. (2022). GVM310 Global Vehicle Motor [Online dataset]. Retrieved from: https://www.parker.com/content/dam/Parker-com/Literature/Electromechanical-Europe/Literature/192_300115_GVM310_catalog.pdf.

Pesaran, A. A., Kim, G. H. & Keyser, M. (2009). Thermal Performance of EV and HEV Battery Modules and Packs. *SAE Technical Paper*.

Plug Power Inc., P. P. I. Fuel Cell Benefits: 5 Facts You Should Know [Online]. Retrieved from: https://www.plugpower.com/fuel-cell-power/fuel-cell-benefits/.

Saib, S., Hamouda, Z. & Marouani, K. (2017). Energy management in a fuel cell hybrid electric vehicle using a fuzzy logic approach. *2017 5th International Conference on Electrical Engineering-Boumerdes (ICEE-B)*, pp. 1–4.

Samosir, A. S., Sutikno, T. & Yatim, A. H. M. (2011). Dynamic evolution control for fuel cell DC-DC converter. *TELKOMNIKA (Telecommunication Computing Electronics and Control)*, 9(1), 183–190.

Sandeep, V. (2021). When and why to use P, PI, PD and PID Controller? [Online]. Retrieved from: https://medium.com/@svm161265/when-and-why-to-use-p-pi-pd-and-pid-controller-73729a708bb5.

Saur, G. & Ramsden, T. (2014). Hydrogen production from wind: Two case studies of the application of high wind to electrolysis for hydrogen production. *International Journal of Hydrogen Energy*, 39(1), 301–306.

Serrao, L., Onori, S. & Rizzoni, G. (2011). A comparative analysis of energy management strategies for hybrid electric vehicles.

Solano, J., Jemei, S., Boulon, L., Silva, L., Hissel, D. & Pera, M.-C. (2019). IEEE VTS motor vehicles challenge 2020-Energy management of a fuel cell/ultracapacitor/lead-acid battery hybrid electric vehicle. *2019 IEEE Vehicle Power and Propulsion Conference (VPPC)*, pp. 1–6.

Solano, J. (2012). *Energy management of a hybrid electric vehicle: an approach based on type-2 fuzzy logic*. (Ph.D. thesis, Université de Franche-Comté).

Sorlei, I.-S., Bizon, N., Thounthong, P., Varlam, M., Carcadea, E., Culcer, M., Iliescu, M. & Raceanu, M. (2021). Fuel cell electric vehicles—A brief review of current topologies and energy management strategies. *Energies*, 14(1), 252.

Spiegel, C. (2011). *PEM fuel cell modeling and simulation using MATLAB*. Elsevier.

Sulaiman, N., Hannan, M., Mohamed, A., Ker, P. J., Majlan, E. & Daud, W. W. (2018). Optimization of energy management system for fuel-cell hybrid electric vehicles: Issues and recommendations. *Applied energy*, 228, 2061–2079.

Syed, S. A. (2012). *Energetic macroscopic representation and multi-level energy management for heavy-duty hybrid vehicles using double planetary geartrain*. (Ph.D. thesis, Lille 1).

The Global EV Outlook, T. G. E. O. (2021). *Global EV Outlook 2021*. https://www.iea.org/reports/global-ev-outlook-2021: INTERNATIONAL ENERGY AGENCY.

Tie, S. F. & Tan, C. W. (2013). A Review of Energy Sources and Energy Management System in Electric Vehicles. *Renewable and Sustainable Energy Reviews*, 20, 82-102.

Tseng, Y.-M., Huang, H.-S., Chen, L.-S. & Tsai, J.-T. (2018). Characteristic research on lithium iron phosphate battery of power type. *MATEC Web of Conferences*, 185, 00004.

U.S. Department of Energy. (2023). How Do Fuel Cell Electric Vehicles Work Using Hydrogen? Retrieved from: https://afdc.energy.gov/vehicles/how-do-fuel-cell-electric-cars-work.

Valle, F. (2014). Electrocatalyst degradation in high temperature PEM fuel cells.

Wang, Y., Chen, K. S., Mishler, J., Cho, S. C. & Adroher, X. C. (2011). A review of polymer electrolyte membrane fuel cells: Technology, applications, and needs on fundamental research. *Applied energy*, 88(4), 981–1007.

Wang, Y., Seo, B., Wang, B., Zamel, N., Jiao, K. & Adroher, X. C. (2020). Fundamentals, materials, and machine learning of polymer electrolyte membrane fuel cell technology. *Energy and AI*, 1, 100014.

Waseem, M., Amir, M., Lakshmi, G. S., Harivardhagini, S. & Ahmad, M. (2023). Fuel Cell-based Hybrid Electric Vehicles: An Integrated Review of Current Status, Key Challenges, Recommended Policies, and Future Prospects. *Green Energy and Intelligent Transportation*, 100121.

Whittingham, M. S. (2012). History, Evolution, and Future Status of Energy Storage. *Proceedings of the IEEE*, 100(Special Centennial Issue), 1518-1534.

Wilberforce, T., Khatib, F., Ijaodola, O., Ogungbemi, E., El-Hassan, Z., Durrant, A., Thompson, J. & Olabi, A. (2019). Numerical modelling and CFD simulation of a polymer electrolyte membrane (PEM) fuel cell flow channel using an open pore cellular foam material. *Science of The Total Environment*, 678, 728–740.

WMO, W. (2019). State of the Climate in 2018 shows accelerating climate change impacts [Online]. Retrieved from: https://public.wmo.int/en/media/press-release/state-of-climate-2018-shows-accelerating-climate-change-impacts.

Wu, S., Zhang, H. & Ni, M. (2016). Performance assessment of a hybrid system integrating a molten carbonate fuel cell and a thermoelectric generator. *Energy*, 112, 520–527.

Yao, G., Du, C., Ge, Q., Jiang, H., Wang, Y., Ait-Ahmed, M. & Moreau, L. (2019). Traffic-Condition-Prediction-Based HMA-FIS Energy-Management Strategy for Fuel-Cell Electric Vehicles. *Energies*, 12(23), 4426.

Zhang, R. & Yao, E. (2015). Electric vehicles' energy consumption estimation with real driving condition data. *Transportation Research Part D: Transport and Environment*, 41, 177–187.